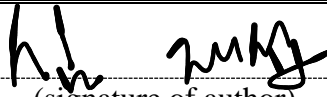




FACULTY OF SCIENCE AND TECHNOLOGY

## MASTER'S THESIS

Study programme/specialisation:  Marine and Offshore Technology	Spring semester; 2020  Open
Author:  Jaesub Sim	 ..... (signature of author)
Programme coordinator:  Professor Muk Chen Ong	
Supervisor(s):  Associate Prof. Lin Li / Prof. Muk Chen Ong / Hui Cheng	
Title of master's thesis:  Numerical study on structural responses of gravity-based fish cages	
Credits: 30 ECTS	
Keywords:  Gravity-based fish cages, wake effect, numerical analysis, marine aquaculture, current load, net structure	Number of pages: 74  + supplemental material/other: 30  Stavanger, June 30. 2020

# NUMERICAL STUDY ON STRUCTURAL RESPONSES OF GRAVITY-BASED FISH CAGES

---

Author : Jaesub Sim  
Supervisor : Associate Prof. Lin Li  
Co-Supervisor : Prof. Muk Chen Ong  
: Hui Cheng

**University of Stavanger**

Faculty of Science and Technology

Department of Mechanical and Structural Engineering and Material Science

Master of Science Thesis, Spring 2020

# Abstract

---

The location of a fish farm is moving towards more exposed locations due to spatial and environmental concerns. As the fish farm moves to open seas, the structure of the fish farm would undergo increased environmental loads induced by a larger wave and faster current compared to the sheltered areas. The increased loads may cause several problems, such as a reduction in cultivation volume and increased tension in mooring lines. The cultivation volume of a fish cage is essential for fish welfare since the reduced volume of a cage stresses the fish leading to high mortality. Moreover, the increased tension in mooring lines may cause accidental failure. Therefore, the accurate estimation of the loads and the structural behavior of the fish farm should be obtained to verify the performance and to secure the integrity of the fish farm structure.

In this thesis, the focuses are made on mainly two issues to estimate loads and structural behavior of the fish farm structure. Firstly, the structural responses such as drag force of a cage, cultivation volume, and mooring line tension are investigated considering the wake effect of a permeable net structure. The wake effect is essential to accurately estimate the hydrodynamic forces of the system since it greatly alters the flow field after a net structure. Moreover, most of the environmental loads come from the net structure due to its largest volume among all components of the fish cage. 4x2 multi-cage fish farm model under current load is investigated, using a well-validated numerical tool called FhSim. The wake effect of a net structure is divided into three regions to realize the flow field inside and outside of a net structure, *i.e.*, (i) twine-to-twine wake effect, (ii) net-to-net wake effect and (iii) cage-to-cage wake effect. A comparative study is used to determine and quantify the influence of the wake effect on dynamic responses of the fish farm structure. The results from the numerical simulations suggest that the drag force of a fish cage can be overestimated up to 76% without the wake effect.

Secondly, the accidental failure of a cable in the mooring grid is considered. As a cable in the mooring grid fails, the load is transferred to neighboring cables leading to a possible rupture of another cable. Thus, it is imperative to discern the loads in cables of the mooring grid under a failure condition to secure the integrity of the structure. Two numerical models are investigated under pure current condition. One is the single-cage model, and the other is the 4x1 multi-cage model. A built-in function of FhSim is utilized to control the occurrence of failure. The cables which trigger the largest tension in a cable are identified. Furthermore, the most significant increases of tension in different types of cable, *i.e.*, mooring line, frame cable, and bridle, are found by comparison between intact and failure mode models. The results indicate that the maximum tension in a mooring line can be increased by up to 31% and 53% for the single and multi-cage systems, respectively.

# Acknowledgements

---

I would first like to thank my main supervisor Associate Prof. Lin Li, for her consistent guidance and consultation throughout the entire thesis work. She continuously steered me in the right direction and inspired me to pursue an advanced performance whenever she thought I need it.

I would also like to express my gratitude to my co-supervisor, Prof. Muk Chen Ong, for his motivation and mentoring that he willingly provided. I extend my sincere appreciation to Ph.D. candidate Hui Cheng. He always swiftly responded me and answered my questions. I am greatly indebted for every effort and time that he bent to answer my queries and feedback. Also, his attitude towards the academic work has greatly inspired me.

Finally, I would like to thank my parents and my wife for their unconditional support throughout the study.

# Contents

---

Abstract.....	i
Acknowledgments .....	ii
Contents.....	iii
List of Figures.....	vi
List of Tables .....	viii
1 Introduction.....	1
1.1 Background and motivation .....	1
1.2 Overview of marine fish cage .....	3
1.2.1 New concepts of fish cage.....	5
1.2.2 Flexible gravity-based fish cage.....	6
1.3 Literature review .....	8
1.4 Scope and objective.....	10
2 Theory.....	12
2.1 Hydrodynamic forces on net structure .....	13
2.1.1 Morison type force model .....	13
2.1.2 Screen type force model .....	16
2.2 Hydrodynamic forces on floating collar.....	18
2.3 Wake behind a circular cylinder.....	18
2.3.1 Flow around a circular cylinder.....	18
2.3.2 Velocity deficit within the wake region.....	21
2.3.3 Near-field modification of the velocity deficit in the wake region.....	22
2.4 Wake behind a screen.....	23

---

3	Numerical method.....	24
3.1	FhSim Framework.....	24
3.2	Structural model.....	27
3.2.1	Net structure .....	27
3.2.2	Floating collar.....	28
3.2.3	Cables .....	28
3.2.4	Buoy .....	29
3.2.5	Sinker tube.....	29
3.3	Implementation of wake effects .....	30
3.3.1	Twine-to-twine wake effect.....	31
3.3.2	Net-to-net wake effect .....	31
3.3.3	Cage-to-cage wake effect .....	32
3.4	Structural failure .....	33
4	Numerical investigation on the cage-to-cage wake effect: A case study of a 4x2 cage array.....	34
4.1	Model set-up .....	35
4.2	Environmental loading .....	37
4.3	Wake effects on drag forces and cultivation volumes of fish cages under different flow directions .....	38
4.3.1	Case 1 (without wake effect) .....	38
4.3.2	Case 2 (with only cage-to-cage wake effect).....	39
4.3.3	Case 3 (with all the three wake effects).....	43
4.3.4	Comparison between the three cases .....	44
4.4	Wake effects on the total drag force and cultivation volume under different flow directions .....	46
4.5	The wake effects on tensions in anchor lines under different flow directions .....	47
4.6	Summary .....	49
5	Numerical study on the structural responses of fish farms under accidental failure condition.....	50
5.1	Environmental loading .....	51
5.2	Single-cage model.....	52
5.2.1	Model set-up.....	52
5.2.2	Tensions in mooring lines and frame cables.....	53

---

5.2.3	Drag force and cultivation volume .....	59
5.3	4x1 multi-cage model.....	60
5.3.1	Model set-up.....	60
5.3.2	Tensions in mooring lines and frame cables.....	63
5.3.3	Drag force and cultivation volume .....	68
5.4	Summary .....	69
6	Conclusions and future work .....	70
	References .....	72
	Appendix A .....	75
A.1	Drag force of all cages with different flow directions and wake effects (Case 1, 2, and 3) .....	76
A.2	Volume of all cages with different flow directions and wake effects (Case 1, 2, and 3).....	78
A.3	Mooring line tensions with different flow directions and wake effects (Case 1, 2, and 3).....	80
	Appendix B.....	82
B.1	Results from the intact model .....	84
B.2	Results from failure mode model.....	85
	Appendix C.....	89
C.1	Results from intact model.....	90
C.2	Results from failure mode model.....	94

# List of Figures

---

Fig. 1-1: World capture fisheries and aquaculture production.....	2
Fig. 1-2: Types of cage system according to its hydrostatic position .....	3
Fig. 1-3: Types of fish cages based on the means of maintaining cultivation volume .....	4
Fig. 1-4: An overview of new concepts of fish cages .....	5
Fig. 1-5: Overview of a single gravity-based fish cage .....	6
Fig. 1-6: Structure of the thesis.....	11
Fig. 2-1: The pressure and viscous forces acting on a circular cylinder .....	13
Fig. 2-2: Current loads acting on an inclined twine.....	15
Fig. 2-3: Illustration of square-woven net .....	16
Fig. 2-4: Force and geometry of a net panel associated with the flow direction.....	17
Fig. 2-5: Regions of disturbed flow .....	19
Fig. 3-1: Overview of the FhSim architecture .....	25
Fig. 3-2: Flow chart for the transfer of variables across interconnected sub-models .....	25
Fig. 3-3: Tetrahedron volume integration method.....	26
Fig. 3-4: Triangular element used for the net structure.....	27
Fig. 3-5: Illustration of triangular elements for net structure.....	28
Fig. 3-6: Illustration of different wake effects .....	30
Fig. 3-7: Illustration of the method to identify the nets which experience the net-to-net wake effect.....	31
Fig. 3-8: Velocity profile 1.5D downstream behind a fish cage .....	32
Fig. 4-1: Configuration of 4x2 multi-cage fish farm layout .....	35
Fig. 4-2: Time history for the estimated cage volume of Cage 1.....	37
Fig. 4-3: Drag force and cultivation volume of cages (Case 1) .....	38
Fig. 4-4: Drag force and cultivation volume of cages (Case 2) .....	39
Fig. 4-5: Deformed state of cages for Case 1 and Case 2 .....	40
Fig. 4-6: Flow interference of upstream cage to downstream cage .....	41
Fig. 4-7: Illustration of the velocity defect zone when the flow direction is 60° .....	42
Fig. 4-8: Drag force and cultivation volume of cages (Case 3) .....	43
Fig. 4-9: Drag force and cultivation volume of Cage 8 .....	44



---

Fig. 4-10: Deformed states of Cage 5 and 8 .....	45
Fig. 4-11: Illustration of the velocity defect zone when the flow direction is 20° .....	45
Fig. 4-12: Total drag force and cultivation volume of all cages .....	46
Fig. 4-13: Comparison of ETAL based on the three cases when the ambient flow velocity is 0.5 m/s.....	48
Fig. 5-1: Time history of estimated cage volume .....	51
Fig. 5-2: Plan view of the single-cage model .....	52
Fig. 5-3: Distribution of tensions in cables of the intact single-cage model (flow direction = 0°) .....	53
Fig. 5-4: Upstream mooring line tension for the intact single-cage model.....	55
Fig. 5-5: Critical cable tension in case of failure .....	56
Fig. 5-6: Tension distribution and the location of the structure when U1 fails.....	57
Fig. 5-7: Maximum tensions of the mooring line, bridle, and frame cable.....	58
Fig. 5-8: Deformed state of the net structure of the single-cage model.....	59
Fig. 5-9: Planview of 4x1 multi-cage fish farm model.....	60
Fig. 5-10: Extreme loads for intact 4x1 multi-cage model .....	61
Fig. 5-11: Velocity contour when the flow direction is 0° .....	62
Fig. 5-12: Velocity contour when the flow direction is 30°.....	62
Fig. 5-13: Velocity contour when the flow direction is 50°.....	62
Fig. 5-14: Distribution of tension among mooring lines and frame cables when the flow direction is 20° .....	63
Fig. 5-15: The shifted position of the 4x1 multi-cage model (flow direction = 20°) .....	64
Fig. 5-16: Dislocation of the 1x4 multi-cage model when V4 fails.....	65
Fig. 5-17: The largest tension of each upstream mooring line among all failure modes .....	66
Fig. 5-18: Tension distribution among mooring lines and frame cables (U2 fails, flow direction = 20°) .....	67
Fig. 5-19: Cultivation volume and drag force of all cages for the intact model .....	68

# List of Tables

---

Table 2-1: Regimes of flow around a smooth, circular cylinder in steady current .....	20
Table 4-1: Dimensions and properties of the fish cage used in this thesis.....	36
Table 4-2: Simulation matrix.....	37
Table 4-3: Drag force of cages for Case 1 and Case 2.....	40
Table 5-1: Simulation matrix.....	51
Table 5-2: Change of length and strains of mooring lines and frame cables .....	54
Table 5-3: The largest tension in upstream mooring line and failure mode .....	67
Table A-1: Simulation matrix for 4x1 multi-cage model .....	76
Table A-2: Total drag force for all cages for different flow directions (Case 1) .....	76
Table A-3: Total drag force for all cages for different flow directions (Case 2) .....	77
Table A-4: Total drag force for all cages for different flow directions (Case 3) .....	77
Table A-5: Cultivation volume of all cages for different flow directions (Case 1) .....	78
Table A-6: Cultivation volume of all cages for different flow directions (Case 2) .....	78
Table A-7: Cultivation volume of all cages for different flow directions (Case 3) .....	79
Table A-8: Mooring line tension for different flow directions (Case 1).....	80
Table A-9: Mooring line tension for different flow directions (Case 2).....	80
Table A-10: Mooring line tension for different flow directions (Case 3).....	81
Table B-1: Pre-tensions of mooring lines .....	83
Table B-2: Pre-tensions of frame cables.....	83
Table B-3: Pre-tensions of bridles .....	83
Table B-4: Tensions in mooring lines of the intact single-cage model for different flow directions .....	84
Table B-5: Tensions in frame cables of the intact single-cage model for different flow directions .....	84
Table B-6: Tensions in bridles for different flow directions .....	85
Table B-7: Tensions in mooring lines for different failure modes when the flow direction is 0° .....	85

---

Table B-8: Tensions in frame cables for different failure modes when the flow direction is $0^\circ$ .....	86
Table B-9: Tensions in bridles for different failure modes when the flow direction is $0^\circ$ .....	86
Table B-10: Tensions in mooring lines for different failure modes when the flow direction is $90^\circ$ .....	87
Table B-11: Tensions in frame cables for different failure modes when the flow direction is $90^\circ$ .....	87
Table B-12: Tensions in bridles for different failure modes when the flow direction is $90^\circ$ .....	88
Table C-1: Tensions in mooring lines for different flow directions .....	90
Table C-2: Tensions in frame cables for different flow directions .....	91
Table C-3: Tensions in bridles of Cage 1 for different flow directions .....	91
Table C-4: Tensions in bridles of Cage 2 for different flow directions .....	92
Table C-5: Tensions in bridles of Cage 3 for different flow directions .....	92
Table C-6: Tensions in bridles of Cage 4 for different flow directions .....	93
Table C-7: Tensions in mooring lines for different failure modes (flow direction = $20^\circ$ ) .....	94
Table C-8: Tensions in frame cables for different failure modes (flow direction = $20^\circ$ ) .....	95
Table C-9: Tensions in frame cables for different failure modes (flow direction = $50^\circ$ ) .....	96
Table C-10: Tensions in bridles of Cage 1 for different failure modes (flow direction = $50^\circ$ ) .....	97
Table C-11: Tensions in bridles of Cage 2 for different failure modes (flow direction = $50^\circ$ ) .....	98
Table C-12: Tensions in bridles of Cage 3 for different failure modes (flow direction = $50^\circ$ ) .....	99
Table C-13: Tensions in bridles of Cage 4 for different failure modes (flow direction = $50^\circ$ ) .....	100
Table C-14: Tensions in bridles of Cage 1 for different failure modes (flow direction = $70^\circ$ ) .....	101
Table C-15: Tensions in bridles of Cage 2 for different failure modes (flow direction = $70^\circ$ ) .....	102
Table C-16: Tensions in bridles of Cage 3 for different failure modes (flow direction = $70^\circ$ ) .....	103
Table C-17: Tensions in bridles of Cage 4 for different failure modes (flow direction = $70^\circ$ ) .....	104

# Chapter 1

## Introduction

---

### 1.1 Background and motivation

As proclaimed in the universal declaration of human rights ratified by member states of the UN (United Nations), “everyone has the right to a standard living adequate for the health and well-being of himself and of his family, including food.” In this regard, one of the SDGs (Sustainable Development Goals) is agreed by all UN member states to end poverty. According to FAO (Food and Agriculture Organization of the United Nations), the global population is expected to reach 9 billion by the middle of the twenty-first century. As the population grows, so does the need for food. The aquaculture industry is highlighted in the critical importance of meeting the food demand since the growth in the supply of fish for human consumption has been twice as high as population growth over the decades. The production of aquaculture has been shown rapid growth since the late 1980s, while the captured fish production is static [1]. In 2018, the share of aquaculture reached 46.0 % of total fishery production (Fig. 1-1), and it appears to surpass the share of captured fish production in a short period [2]. Thus, the growth of aquaculture is the most promising to meet the food demand and to alleviate hunger worldwide.

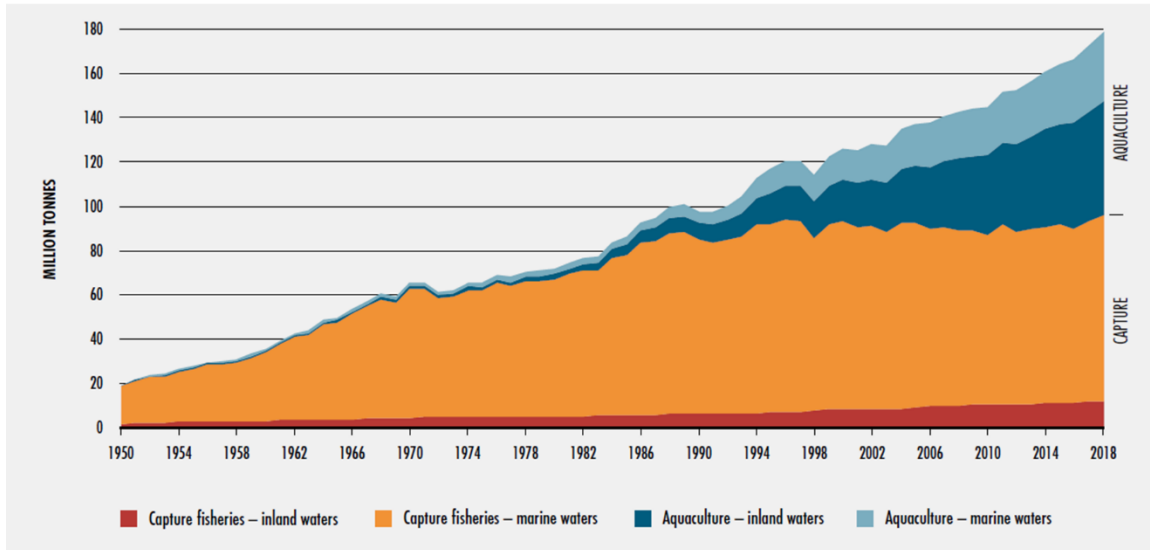


Fig. 1-1: World capture fisheries and aquaculture production [2].

In Norway, the aquaculture industry is predominant in finfish farming, such as Atlantic salmon (*Salmo Salar*), which is cultured in the sea-based fish cages from the smolt stage until it reaches to harvesting weight (4-5 kilogram). The Atlantic salmon is currently the most widely cage-reared fish species, accounting for 51% of worldwide cage aquaculture production, and Norway contributes more than half of the global Atlantic salmon production [3]. The global production of Atlantic salmon reached approximately 2.5 million tons in 2018, which is 2.9 % of the global aquaculture production and expected to surpass three million tons by 2022 [4].

Norwegian aquaculture industry faces many challenges such as sea lice, environmental impact on the surrounding ecosystem, and lack of space for expansion. The occurrence of sea lice can cause catastrophic damage to the aquaculture industry since the fish are reared in a cage with high density, leading to a frequent transmission of the lice. The space for the fish farm near shore is limited as the aquaculture industry grows. Thus, new areas for the industry should be secured for further development. In addition, the feed residues and feces from cages have an impact on coastal wildlife such as algal bloom and disease infections. Moving aquaculture towards the open seas is beneficial to tackle these challenges. In the open seas where the water depth is relatively deep than the coastal regions, the occurrence of sea lice is expected to diminish by keeping the fish further below sea level. The strong current of the site offers frequent water exchange by removing feed residues and feces, and the greater distance from the shore minimizes the impact on the coastal wildlife [4]. Furthermore, ample space for the expansion of the aquaculture industry is provided in the open ocean. However, the exposed setting implies that the fish cages are to be subjected to harsh environmental conditions, which can increase the initial investment for cages and mooring system, the cost of maintenance, and the risk of failures [1]. Therefore, it is vital to accurately predict the loads imposed on the structure in the design phase concerning both the economic and safety aspects.

## 1.2 Overview of marine fish cage

Cage system can be classified according to its hydrostatic positioning with three different variants: (i) floating cages, (ii) semi-submerged cages, and (iii) submersible cages (Fig. 1-2). floating cages are traditional cages that deployed on the water surface and have a constant water line. Semi-submerged cages are able to vary the waterline and to operate in a partially submerged state (the upper part of the cage is always above the water surface) in order to reduce the wave load on the pontoons underwater. Submerged cages have a system to be fully submerged underwater in the case of a harsh environmental condition, *e.g.*, a storm. The cages of this type remain on the surface other than the undesirable situation [5].

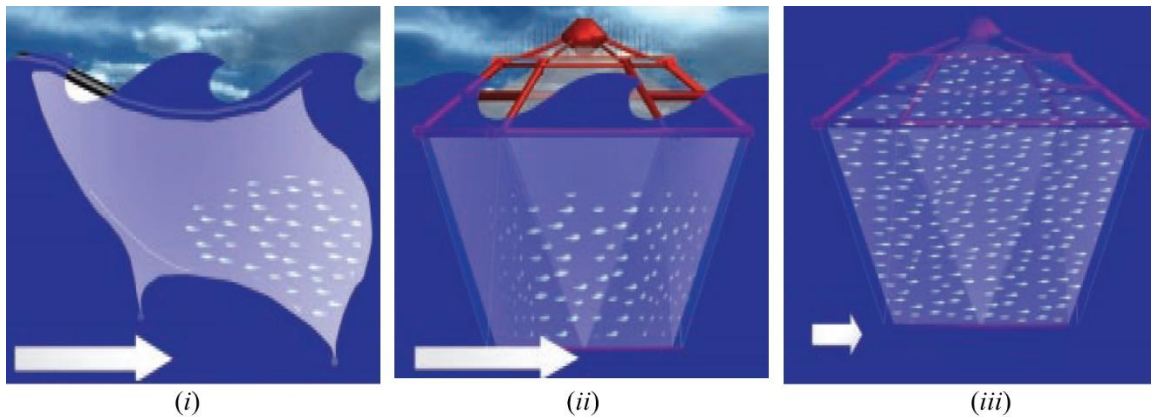


Fig. 1-2: Types of cage system according to its hydrostatic position [5].

Another way to classify the cage system is proposed by Loverich and Gace [6] based upon the structural systems used to maintain the cultivation volume. There are four types of cages; (a) Gravity cages, (b) anchor-tension cages, (c) semi-rigid cages, and (d) rigid cages (Fig. 1-3). Type (a), gravity cages are by far the most widely adopted cage system in the fish farming industry. These cages float by the buoyancy element, such as a floating collar, and the underwater weighing system is provided to maintain the cultivation volume by the force of gravity. Type (b) anchor-tension cages rely on a tensioned mooring system to maintain the cultivation volume as there is no rigid frame. Type (c) semi-rigid cages utilize the ropes to connect rigid steel parts to maintain the cultivation volume. Finally, the last type (d) rigid cages use the rigid structural components made of steel and other materials in order to maintain the cultivation volume [7].

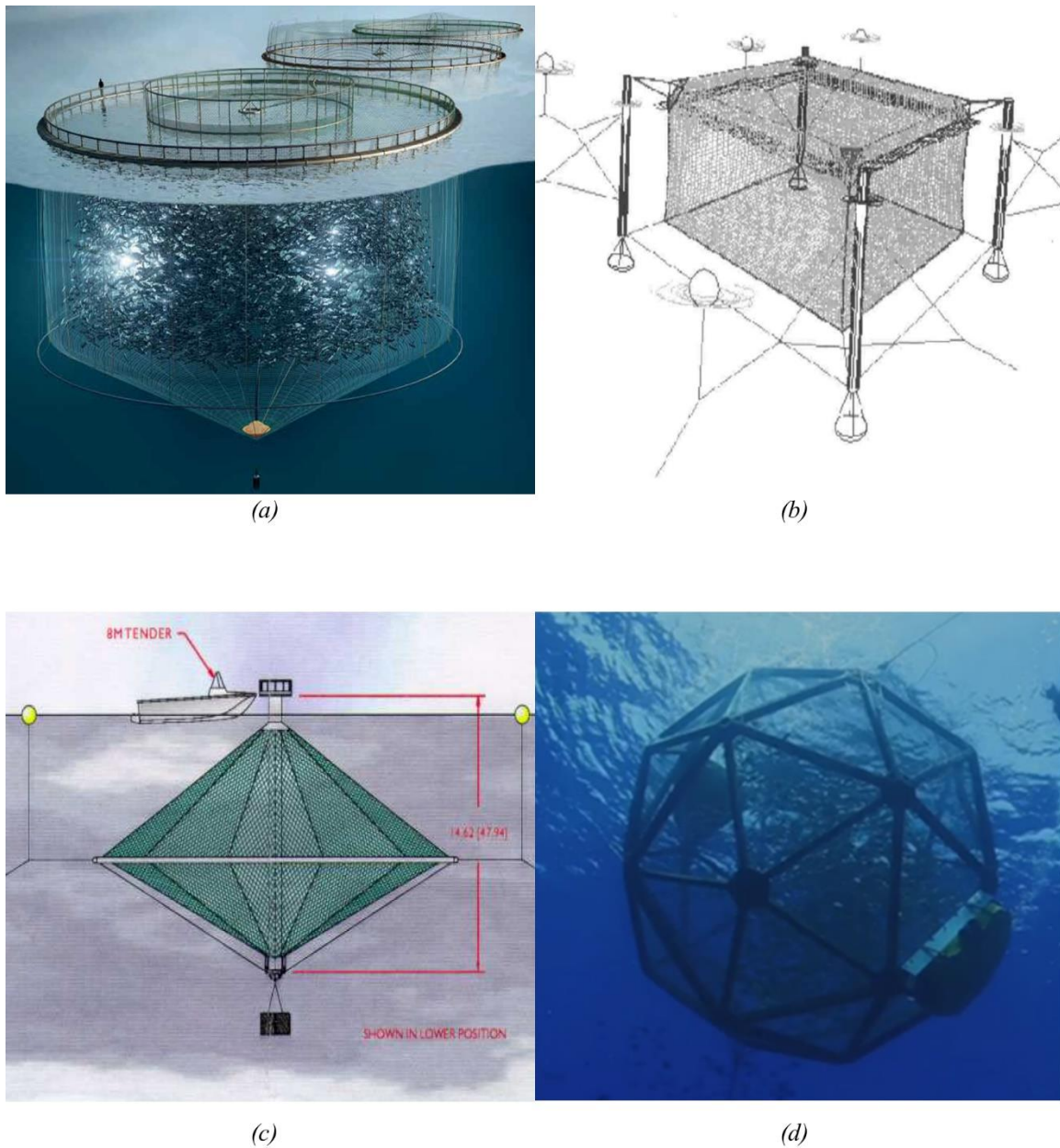


Fig. 1-3: Types of fish cages based on the means of maintaining cultivation volume. (a) Illustration of Gravity cages [8], (b) Illustration of anchor-tension cage [9], (c) semi-rigid fish cage [9], and (d) rigid fish cage [10].

## 1.2.1 New concepts of fish cage

Several new concepts of fish cages have been proposed for offshore applications to withstand the harsh environmental conditions of exposed seas. RefaMed [11] proposed a tension-leg cage that resembles an inverted gravity cage. However, the tension-leg cage differs from the gravity cage by having a small floating collar with no mooring lines attached to it. This configuration of the cage may enable the structure to avoid the high loadings in extreme wind and wave conditions [7]. Nordlaks AS [12] proposed a vessel-shaped fish farm with a multiple cage system. The vessel-shaped hull of the cage system is anticipated to reduce the wave load coming from the bow. Furthermore, the vessel-shaped fish cage system adopts the single-point mooring system, which allows the entire fish farm to rotate about the bow. Hence, the feces from the fish and the residue of the feed can spread in a wider range of areas, reducing the risk of fish infections [13].

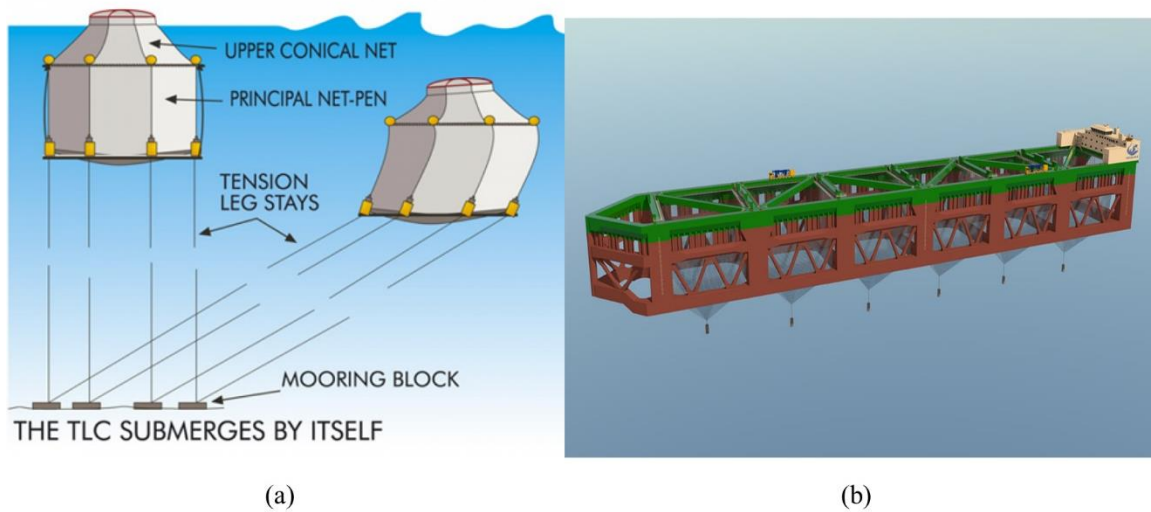


Fig. 1-4: An overview of new concepts of fish cages. (a) Tension-leg cage [11], and (b) Vessel-shaped fish cage [12]



## 1.2.2 Flexible gravity-based fish cage

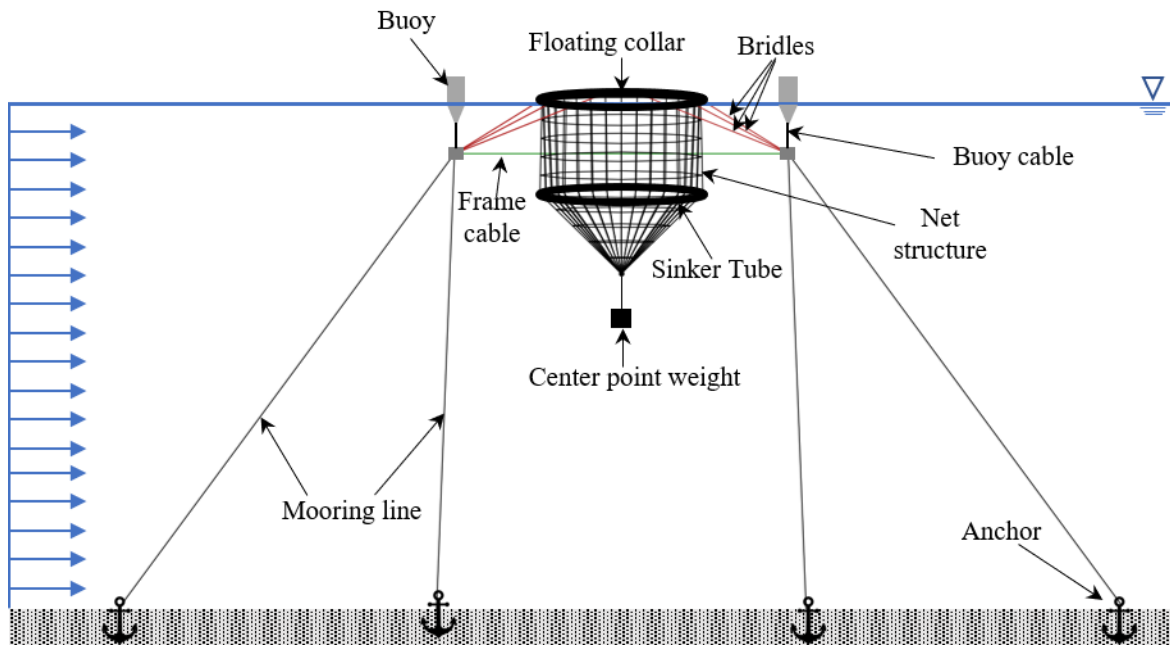


Fig. 1-5: Overview of a single gravity-based fish cage.

A type of fish cage chosen for the study in this thesis might be categorized as both the floating type and gravity type, which is called hereafter as a flexible gravity-based fish cage. The flexible gravity-based fish cage is a typical Norwegian fish cages used in the aquaculture industry. A schematic description of a single fish cage is given in Fig. 1-5. The same fish cage cell is used for the multi-cage array configuration. The fish cage is composed of a two-pipe floating collar, buoys, cylindrical net structure with a conical base, a sinker tube, and chains connecting the net with the sinker tube. Brief explanations regarding the components are as follows:

### Floating collar

The floating collar is a hollow pipe made of high-density polyethylene (HDPE) pipe. It is an essential component of the fish cage since it provides the majority of the buoyancy force of the fish cage to remain afloat. In addition, it provides the hang-off point for the net structure and connecting points for bridles.

## Net structure

The net structure is an essential part of the fish cage as it serves to keep the fish or any other biomass inside from escaping. A typical net structure of a gravity-based fish cage has a shape with a cylindrical body attached to the floating collar and conical body at the bottom. Twines of the net structure are made of the material, which has a very low bending stiffness to obtain enough flexibility. Therefore, it physically sounds to be deformed when the net structure is subjected to environmental loads such as current, wind, and wave. The sinker tube and center point weight are applied to maintain the shape of the net structure in such conditions.

## Buoy

The buoys serve as an additional buoyancy to the fish cage system, and each buoy has a steel plate underneath the waterline, attached through a cable (buoy cable). There are four buoys around a fish cage, and the buoys are connected with frame cables via steel plates, forming a grid for the cage, which is often called a fish cell. Also, the mooring line from the anchor at the seabed is attached to the steel plate.

## Sinker tube

As mentioned above, the purpose of the sinker tube is to provide the weight to maintain the volume of net structure in case of environmental loads. The sinker tube is a hollow pipe made of high-density polyethylene, as same as a floating collar. However, it is filled with heavy pieces of stuff to provide a sufficient gravitational force.

## Mooring system

A mooring system is a network of cables (mooring lines, frame cables, and bridles) to keep the position of the fish cages when the environmental loads are imposed onto the system. Therefore, the design of the mooring system is essential for the operation and performance of the fish farm. A floating collar provides three connection points to each steel plate of a buoy, *i.e.*, a total of 12 connection points are provided to four steel plates around the fish cell. The steel plates are connected to connection points of the floating collar by means of bridles so that the fish cage can hold its position within the fish cell in case of environmental loads. Anchors at the bottom of the seabed attached to the steel plates through mooring lines to prevent the fish farm structure from drifting.

## 1.3 Literature review

The fish farm structure system is often flexible and complex since the structure consists of several components, such as net structures, floaters, buoys, and cables. Thus, it is challenging to replicate physical behavior through a numerical simulation. A number of efforts have been made to estimate the responses of fish farm structures accurately. Several researchers put their efforts to identify the flow characteristics behind the net and fish cage. Løland [14] proposed an empirical expression for the velocity reduction behind a net panel based on model testing ( $r=1-0.46C_D$ ,  $r$  is the velocity reduction factor,  $C_D$  is the drag coefficient of a net panel) and applied this expression to represent the wake effect after a fish cage. The empirical expression gives a uniform reduced flow throughout the entire wake. However, the flow field after a circular net structure is not uniform since the flow is not always normal to the net panel due to different locations of the twines and the deformation of the fish cage. Bi and Xu [15] numerically simulated the flow field around a 4x2 fish farm using the porous-media model. However, the deformation of the fish cage was not considered in the simulation.

The experimental study of fish farms has been widely treated in scientific literature to investigate the wake effect among fish cages in an array. Turner *et al.* [16] conducted an experiment in a large flume tank to measure the drag forces of each square cage within a 2x3 array. The results showed that when the cages were aligned in a flow direction, the drag forces on the second and the third cages are reduced approximately 50% and 75%, respectively, compared to that of the first cage. Gansel *et al.* [17] conducted experiments to measure the wake characteristics behind a circular fish cage by using particle image velocimetry (PIV). The results indicated that the flow velocity was reduced up to 40% behind the fish cage and increased 20% at the flanks of the fish cage.

Other researchers have made their focus to estimate the load of the net structure in various approaches. Kristiansen and Faltinsen [18] used the screen type force model to calculate the load of the net structure and compared it with the experiment data. They found that the screen-type force model has shown a more satisfactory agreement for drag and lift force and claimed that the Morison-type force model over-estimates the drag force when the inflow angle exceeds 45°. Endresen *et al.* [19] developed a numerical method to predict the current load on a net structure using the Morison-type force model. The interaction between net twines has been taken into account based on Blevins virtual origin formula [20]. The results well agreed with experimental data but limited to the low flow velocities (< 0.33 m/s). Moe-Føre *et al.* [21] carried out a study to compare three different structural models (triangle, truss, and spring models) associated with the Morison-type force model and validated against physical model tests with different solidity ratios and flow velocities. They found that none of the numerical models were able to reproduce the hydrodynamic forces obtained from the physical model test. However, when the solidity ratio is 0.19, all models showed a good agreement with the values from the physical model tests for all flow velocities from 0.26 to 0.93 m/s.

Furthermore, various researches have been made to investigate the fish farm structure with multi-cage configurations. Zhao *et al.* [22] established a numerical model for multi-cage fish farms using a porous media model and showed 69% of velocity reduction when the flow passed through four cages. Tsarau and Kristiansen [23] studied the 2x4 multi-cage model to identify the mooring line tension and sensitivity of various parameters (structural stiffness, wave-spectrum, and hydrodynamic-drag law) to mooring loads. However, the research on the responses of fish cages under accidental failures is insufficient. Recently, Tang *et al.* [24] investigated structural responses of a single fish cage after a failure happened in the mooring system. The results indicated that the tension in the remaining mooring line could be 1.4 times of the tension under intact condition.

Regulations for certification and inspection of fish farms in Norway point to technical standards like NS9415 for specific technical requirements. This Norwegian standard, released in 2003 and revised in 2009, defines the technical requirements for site survey, risk analysis, dimensioning, design, construction, installation, and operations of floating fish farms [25]. It dictates the requirements to calculate and document the minimum accidental / damage conditions, which includes breaks in mooring lines, especially for progressive breaks. Thus, there is a need to assess the stability of the mooring system under accidental failures.

## 1.4 Scope and objective

The aquaculture industry tackles a number of challenges, such as lack of space for the cages, sea lice, environmental impact on the surrounding ecosystem, *etc.* The challenges might be solved by moving the cages to a more exposed area. Hence, technical solutions are required to overcome the challenges. One of the technical solutions is to accurately estimate the structural responses of the system. In this regard, the scope of this thesis focuses on mainly two topics as follows:

Firstly, the flow characteristics behind the permeable net cages are investigated by implementing nonuniform wake into a FE solver, FhSim, to simulate a 4x2 multi-cage fish farm under pure current conditions. To investigate how the wake region behind a fish cage affect the structural responses of a downstream cage and 4x2 multi-cage fish farm system, three cases, *i.e.*, (a) without wake effects, (b) with only cage-to-cage wake effect, (c) with all the wake effects, are applied in the simulations. The drag force and cultivation volume of each fish cage, and tensions in all anchor lines are presented to discuss the influence of wake effects on the structural behavior. With the comparative study between cases, this study can provide suggestions on how to consider the wake effects during the design of the multi-cage system.

Secondly, the responses of the fish farm system under intact and failure conditions for both single-cage and 4x1 multi-cage configuration of gravity-based fish cages are investigated. The wake effects are implemented on both single and multi-cage models. For the single-cage model, the cage-to-cage wake effect is omitted since there is no upstream cage for the model. For the multi-cage model, the structural behaviors are investigated (c) with all the wake effects. The most loaded cable for both models is investigated. In addition, the change in tension on a single cable is investigated by comparison between two conditions (intact and failure).

The structure of the thesis is given in Fig. 1-6 on the next page.

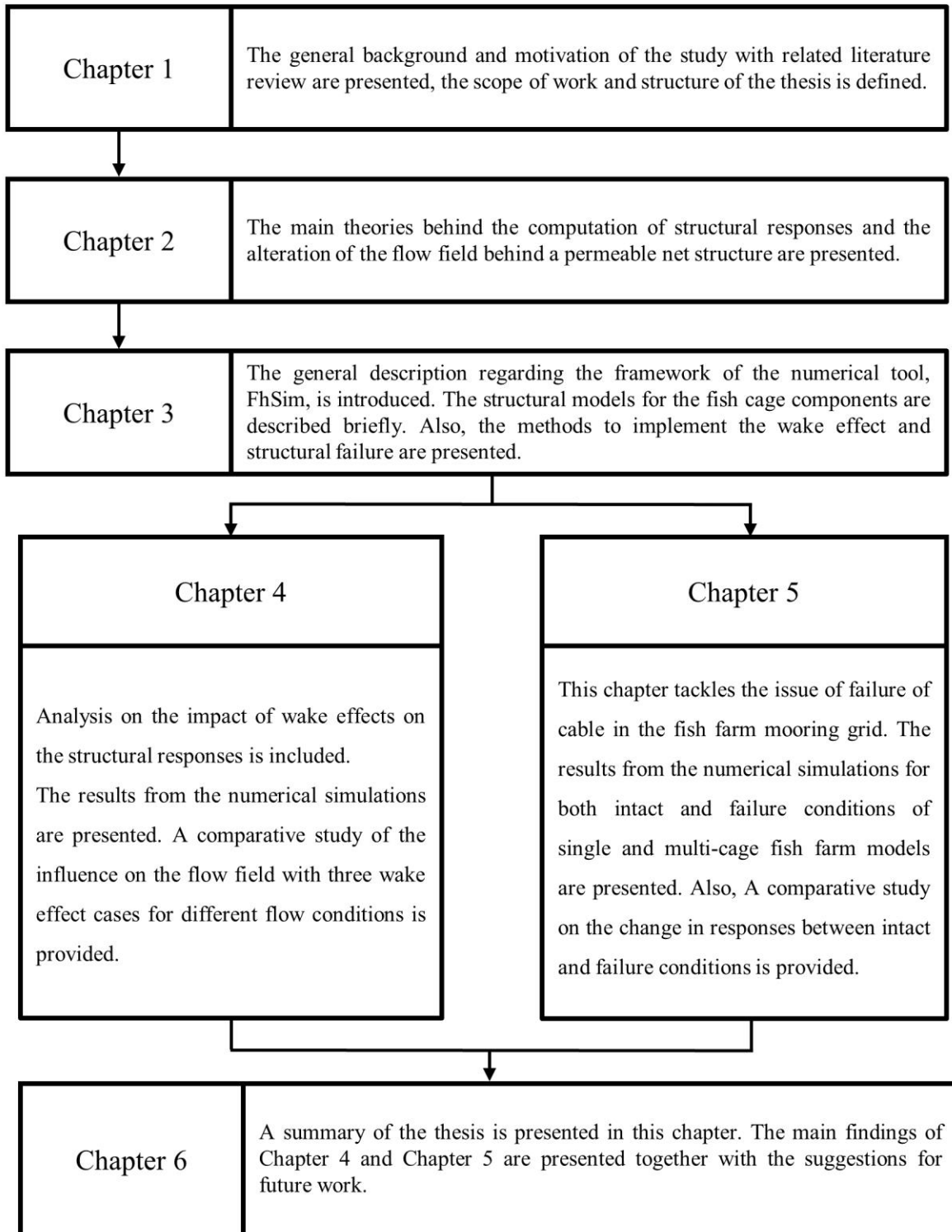


Fig. 1-6: Structure of the thesis.

# Chapter 2

## Theory

---

This chapter provides the fundamental theories regarding the computation of hydrodynamic forces on the fish cage. The major contribution of the forces exerted onto the fish farm structure might come from two components of the fish cage, such as net structure and floating collar. Therefore, the focus of this chapter is placed on the computation of hydrodynamic forces acting on these components. However, the force acting on the floating collar of the cage is largely due to the wave excitation force. Hence the large volume of this chapter is allocated for the background of the computation of force exerted on net structure as the environmental load in this thesis is limited to the pure current condition.

## 2.1 Hydrodynamic forces on net structure

In this section, the fundamental theories behind two hydrodynamic force models for the net structure are covered. The Morison type force model and screen type force model are the two types of force models that are mainly applied to compute the forces on the aquaculture net structure.

### 2.1.1 Morison type force model

In this approach, the net structure is considered as a collection of many twines, which is a slender cylinder. The hydrodynamic forces on each cylinder are computed using Morison's equation and summed to obtain the total drag force of the net structure. This approach is implemented in FhSim numerical tool in this thesis.

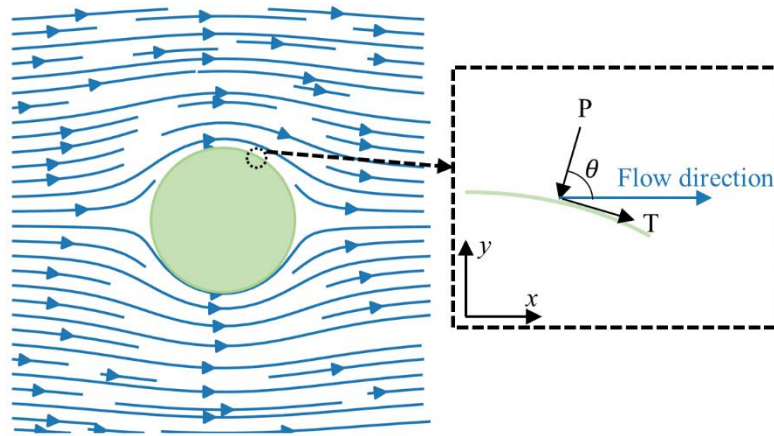


Fig. 2-1: The pressure and viscous forces acting on a circular cylinder.

As the twine of the net structure is considered as a circular cylinder in the Morison type force model approach, it is imperative to discern the force exerted on a cylinder when it is submerged in a flow. A fluid at rest exerts only normal pressure forces on the surface of an immersed cylinder. However, the fluid in motion also exerts tangential shear forces on the surface due to no-slip condition. The drag force is the product of pressure force and friction force in the direction of flow. The components of pressure force and friction force in the orthogonal direction of the flow is called lift force. However, the only time-averaged force exerted on the axisymmetric body, such as a circular cylinder, is the drag force [26]. The expression for the differential drag force  $dF_D$  is:

$$dF_D = -PdA \cos \theta + TdA \sin \theta \quad \text{Eq. 2-1}$$



where  $P$  is the pressure around cylinder,  $dA$  is the differential area of the cylinder,  $T$  is the shear stress acting on the cylinder, and  $\theta$  is the angle between the flow direction and the pressure vector which is inward normal to the surface of the cylinder (see Fig. 2-1). By integrating the Eq. 2-1 over the entire surface of the cylinder yields the expression for the total drag force acting on the cylinder.

$$F_D = \int_A (-P \cos\theta + T \sin\theta) dA \quad \text{Eq. 2-2}$$

The total drag force on a cylinder depends on the density of the fluid  $\rho$ , flow velocity  $U$ , and size of the cylinder (diameter)  $d$ . Thus, it is practical to express the drag force with dimensionless drag coefficient by dividing the Eq. 2-2 with stagnation pressure (kinetic energy of the flow)  $0.5d\rho U^2$ . The drag coefficient for a circular cylinder is as follows:

$$C_d = \frac{F_D}{0.5d\rho U^2} \quad \text{Eq. 2-3}$$

The drag force on a unit length of the cylinder can be arranged as a function of the stagnation pressure and drag coefficient. The drag coefficient is dependent on the Reynolds number since both the pressure and the friction force are dependent on the Reynolds number. The drag force on a circular cylinder with unit length is as follows:

$$F_D = 0.5\rho U^2 C_d(Re)d \quad \text{Eq. 2-4}$$

where  $C_d(Re)$  is the Reynolds number dependent drag coefficient.

The Morison's equation is applied to compute the hydrodynamic forces on a slender cylindrical body (net twine). The equation is based on the cross-flow principle that the force depends only on the velocity component normal to the cylinder axis. Morison *et al.* [27] superimposed the inertia force and the drag force to find the cross-flow force, which is acting on a unit length of the submerged slender cylindrical body (Eq. 2-5).

$$F(t) = \frac{\pi}{4} \rho C_m d^2 \cdot \dot{u}(t) + \frac{1}{2} \rho C_d d \cdot u(t)|u(t)| \quad \text{Eq. 2-5}$$

where  $C_m$  is the mass coefficient,  $C_d$  is the drag coefficient,  $\rho$  is the density of the fluid around the cylinder,  $d$  is the diameter of the cylinder,  $u$  is the velocity of the flow, and  $\dot{u}$  is the acceleration of the flow. The first term on the right side of the Eq. 2-5 is the inertial force, and the second is the drag force representing the viscous forces. The inertial term represents the Froude-Krylov force and diffraction force, which is the force exerted on a submerged body by the unsteady pressure field of the oscillatory flow and the force diffracted by the presence of the body, respectively. The inertial term becomes zero when the flow is steady, leaving only the drag term.

In case of inclined twines due to the geometry of the fish cage or the deformation of the cage, the velocity components which are normal and tangential to the twine should be taken into consideration to compute the drag associated with cross-flow principle (see Fig. 2-2).

$$\begin{aligned} F_N &= 0.5\rho|U_N|U_NAC_N \\ F_T &= 0.5\rho|U_T|U_TAC_T \end{aligned} \quad \text{Eq. 2-6}$$

where  $U_N$  and  $U_T$  are normal and tangential component of the ambient flow velocity, respectively.  $C_N$  and  $C_T$  are normal and tangential drag coefficients, and  $A$  is the reference area, which is the product of length and diameter of twine. The force normal to the axis of the cylinder  $F_N$  is computed by Morison's equation. The tangential force  $F_T$  is mainly due to the friction, which is typically very small for net twines [18].

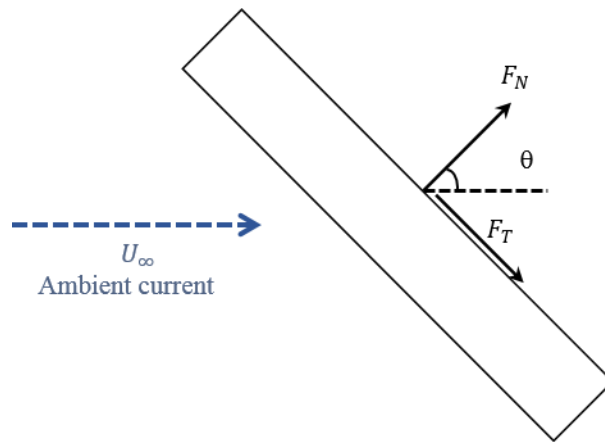


Fig. 2-2: Current loads acting on an inclined twine.

The Morison type force model, however, cannot be justified when the inflow angle is greater than  $45^\circ$ , and the interaction between twines are not considered [18]. The approach to consider the interaction between twines has been adopted in this thesis by implementing the twine-to-twine wake effect. The implementation of the wake effects into FE solver is presented in Section 3.3.

### 2.1.2 Screen type force model

In this approach, the net structure is divided into several net panels (screens). The hydrodynamic forces on each net panel are computed and summed to obtain the hydrodynamic force exerted on the net structure. The terms net panel and screen are used interchangeably hereafter. The net panel is a permeable element consisting of a number of twines, which experiences the viscous load and added mass load. Thus the orientation of the panel to the inflow and the solidity ratio are the main characteristics to describe the flow through net panel [18].

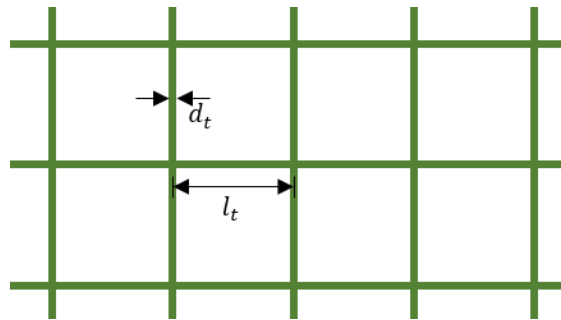


Fig. 2-3: Illustration of square-woven net.

The solidity ratio represents the permeability of the net structure. If the solidity ratio is 1, the cage can be considered as a solid structure, letting no water particles pass through it. The solidity ratio increases mainly due to biofouling, and it has a substantial impact on both the total drag force acting on the net structure and the wake region behind the net. According to the experiment done by Gansel *et al.* [17], the increase of drag force on the net structure is up to 40% when the solidity ratio is changed from 0.2 to 1. In this thesis, the solidity ratio is fixed to 0.2.

The definition of the solidity ratio is the ratio between the total area of the net and the projected area. Thus, it can be expressed in terms of twine diameter and size of a mesh (see Fig. 2-3) as it is written in Eq. 2-7.

$$S_n = 2 \frac{d_t}{l_t} - \left( \frac{d_t}{l_t} \right)^2 \quad \text{Eq. 2-7}$$

where  $S_n$  is the solidity ratio,  $d_t$  is the diameter of a twine, and  $l_t$  is the size of a mesh.

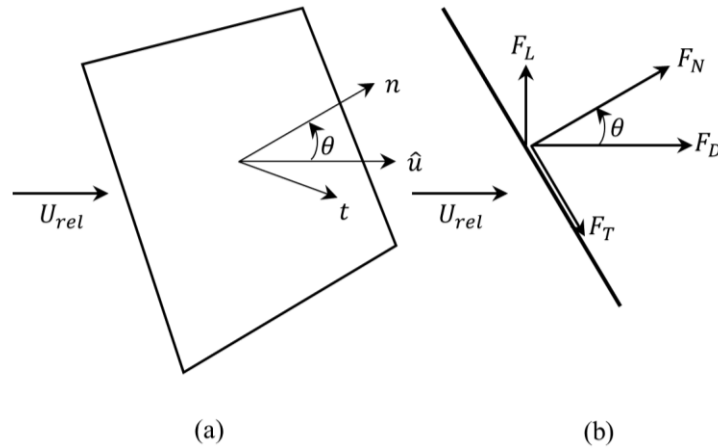


Fig. 2-4: Force and geometry of a net panel associated with the flow direction. (a) General panel with arbitrary orientation and (b) two-dimensional panel [18].

The drag and lift forces of the net panel are highly dependent on the inflow angle since the total force on a net panel is not in the inflow direction due to a deflection of the flow through the panel [18]. Løland [14] proposed a screen model which has a drag and lift coefficients as a function of solidity ratio and inflow angle for a limited range of solidity ratio (0.13 – 0.317) as follows:

$$\begin{aligned} C_D &= 0.04 + (-0.04 + 0.03S_n + 6.54S_n^2 - 4.88S_n^3) \cos \theta \\ C_L &= (-0.05S_n + 2.3S_n^2 - 1.76S_n^3) \sin 2\theta \end{aligned} \quad \text{Eq. 2-8}$$

where  $C_D$  is the drag coefficient for a net panel,  $C_L$  is the lift coefficient for a net panel,  $S_n$  is solidity ratio,  $\theta$  is the angle between the flow direction and vector normal to the net panel (Fig. 2-4). He introduced the factor 0.04 in the drag term to consider the drag on a net panel parallel to the flow. However, the formulation was not able to get a general relation between solidity ratio and drag coefficient accounting for different mesh type, mesh size, and the Reynolds number.

The screen model proposed by Kristiansen and Faltinsen [18] takes Reynolds number into account for generalization of Løland's model. They found a satisfactory agreement for drag and lift by comparison between physical model tests.

## 2.2 Hydrodynamic forces on floating collar

The hydrodynamic forces exerted on the floating collar are the sum of the wave excitation forces, added mass force, and damping forces (Eq. 2-9).

$$F_{float} = F_{fk} + F_{diff} + F_{add} + F_{damp} \quad \text{Eq. 2-9}$$

where  $F_{float}$  is the sum of the hydrodynamic forces acting on the floating collar,  $F_{fk}$  is Froude-Krylov force,  $F_{diff}$  is diffraction force,  $F_{add}$  is added mass force, and  $F_{damp}$  is damping force. The damping term includes the viscous drag force. A drag coefficient of 1.0 is used for the floating collar. However, the value of the drag coefficient does not have significant importance since the total drag force is dominated by the drag force from the net structure. The wave excitation forces are Froude-Krylov and diffraction force, which are the pressure force by the oscillating flow on the body. Froude-Krylov force represents the pressure force by undisturbed oscillating flow due to wave over the wetted surface of the floater, and the diffraction is the correction of the Froude-Krylov force since the flow is disturbed by the presence of the body. Nevertheless, the wave is not considered in this thesis. The environmental condition is regarded as pure current, which is uniform and steady along with the depth of the sea. Thus, the wave excitation force and the added mass force of the floating collar are negligible.

## 2.3 Wake behind a circular cylinder

In order to estimate the hydrodynamic forces on the net structure, the wake effect should be properly accounted for [19]. When a fluid flows over a cylinder, the fluid particle flows within the boundary layer near the cylinder wall due to the viscous effect. The pressure of the fluid around the cylinder is the maximum at the stagnation point. As it moves to the rear of the cylinder following the periphery of the cylinder, the pressure decreases until the rear half of the cylinder. In the region where the favorable pressure present, the flow stays attached to the surface of the cylinder. However, as the pressure increases, the pressure gradient within the boundary layer would be adverse, and backflow at the wall occurs, leading to a separation of flow. The effect of flow separation felt downstream in the form of reduced velocity is called the wake effect [26].

### 2.3.1 Flow around a circular cylinder

In the case of net structure, the twines can be aligned in tandem or staggered position due to its geometry and deformation, namely, the disturbed flow due to the presence of the upstream twine might influence the flow velocity

of downstream twines. Hence, the flow characteristic for the flow around and after a circular cylinder is vital for the determination of disturbed flow velocity.

The flow around a circular cylinder shows a complex flow pattern. The fluid that flows over the cylinder branches out and wraps the cylinder forming a boundary layer. At the front center of the cylinder, the fluid hits the cylinder at the stagnation point, stopping the fluid and raising the pressure at this point. The pressure decreases in the flow direction while the fluid velocity increases [26]. Zdravkovich [28] proposed four regions of disturbed flow over the circular cylinder, as shown in Fig. 2-5:

1. Narrow region of retarded flow
2. Boundary layers attached to the surface of the cylinder
3. Two sidewise regions of displaced and accelerated flow
4. Wide downstream region of separated flow called the wake

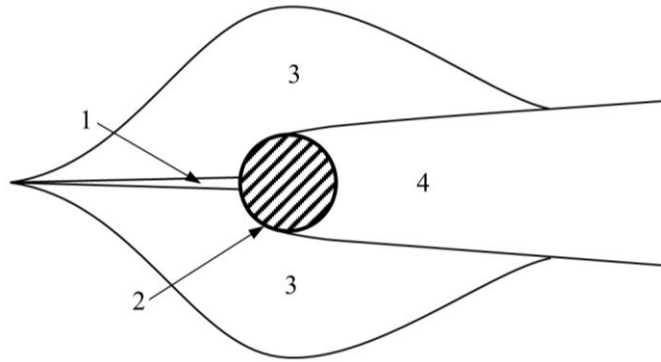



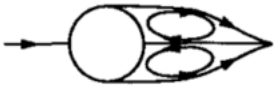


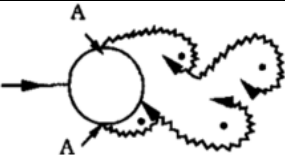
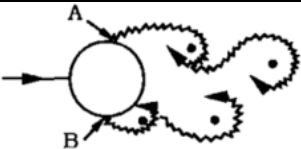
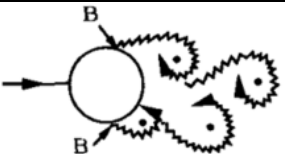
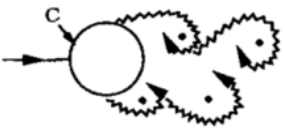

Fig. 2-5: Regions of disturbed flow [28].

The governing parameter for the flow regime of the flow around a smooth, circular cylinder is the Reynolds number  $Re$ .

$$Re = \frac{DU}{\nu} \quad \text{Eq. 2-10}$$

where  $D$  is the diameter of the cylinder,  $U$  is the flow velocity, and  $\nu$  is the kinematic viscosity. The flow regime changes tremendously as the Reynolds number increases from zero. The change of flow regime is summarized in Table 2-1. A typical Reynolds number range for a net structure is between  $10^2$  and  $10^4$ , which is in a subcritical regime where the wake is completely turbulent [29].

Table 2-1: Regimes of flow around a smooth, circular cylinder in steady current [30].

	No separation Creeping flow	$Re < 5$
	A fixed pair of symmetric vortices	$5 < Re < 40$
	Laminar vortex street	$40 < Re < 200$
	Transition to turbulence in the wake	$200 < Re < 300$
	Wake completely turbulent. A. Laminar boundary layer separation	$300 < Re < 3 \times 10^5$ Subcritical
	A. Laminar boundary layer separation B. Turbulent boundary layer separation; but boundary layer laminar	$3 \times 10^5 < Re < 3.5 \times 10^5$ Critical (Lower transition)
	B. Turbulent boundary layer separation; the boundary layer partly laminar partly turbulent	$3.5 \times 10^5 < Re < 1.5 \times 10^6$ Supercritical
	C. Boundary layer completely turbulent at one side	$1.5 \times 10^6 < Re < 4 \times 10^6$ Upper transition
	C. Boundary layer completely turbulent at two sides	$4 \times 10^6 < Re$ Transcritical

### 2.3.2 Velocity deficit within the wake region

Schlichting [31] derived an expression for the mean velocity deficit in the free turbulent flow. However, the expression is limited to a certain distance away from the body (far wake) since free turbulent flow means that the turbulent flow is not confined by any solid walls and is divided into free jet boundaries (neglecting the laminar friction).

When a cylinder is placed in a fluid flow, a wake region is formed behind the cylinder. The cylinder experiences the drag and, in turn, leads to a loss of momentum. As a result, the velocity of the flow in the wake region decreases. The wake region does not extend far in a transverse direction, compared to the main flow direction. Moreover, the transverse gradients are large, which is similar to the nature of the boundary layer. Therefore, the expression for velocity in the wake region is derived from a two-dimensional boundary layer equation for incompressible flow:

$$\begin{aligned} \frac{\partial u}{\partial t} + u \frac{\partial u}{\partial x} + v \frac{\partial u}{\partial y} &= \frac{1}{\rho} \frac{\partial \tau}{\partial t} \\ \frac{\partial u}{\partial x} + \frac{\partial y}{\partial y} &= 0 \end{aligned} \quad \text{Eq. 2-11}$$

where  $\tau$  denotes the turbulent shearing stress. The pressure across the wake is assumed to remain constant thus, the pressure term is neglected. Schlichting introduced the Prandtl's mixing length theory to express the turbulent shearing stress  $\tau$  in terms of the main flow parameters as follows:

$$\begin{aligned} \tau &= \rho l^2 \left| \frac{\partial u}{\partial y} \right| \frac{\partial u}{\partial y} \\ \tau &= \rho \varepsilon_\tau \frac{\partial u}{\partial y} = \rho \chi_1 b (u_{max} - u_{min}) \frac{\partial u}{\partial y} \end{aligned} \quad \text{Eq. 2-12}$$

where  $l$  denotes the mixing length,  $b$  is the width of the mixing zone,  $\chi_1$  is a dimensionless constant determined experimentally, and  $\varepsilon_\tau = \chi_1 b (u_{max} - u_{min})$  is the virtual kinematic viscosity, assumed constant over the whole width. the virtual kinematic viscosity is viewed as an empirical parameter denoted  $\varepsilon_0$  with further assumption that the virtual kinematic viscosity is independent of  $x$ . From Eq. 2-11 and Eq. 2-12, the same expression for the velocity difference between ambient flow velocity and the measured velocity in the wake is found as the laminar wake. Thus, he simply copied the solution found for the laminar wake and replaced laminar kinematic viscosity with  $\varepsilon_0$ , yielding the following expression for the velocity deficit:

$$\frac{u_1}{U_\infty} = \frac{1}{4\sqrt{\pi}} \sqrt{\frac{U_\infty C_d d}{\varepsilon_0}} \left( \frac{x}{C_d d} \right)^{-0.5} \exp \left( -\frac{y^2 U_\infty}{4\varepsilon_0 x} \right) \quad \text{Eq. 2-13}$$



where  $u_1$  is the velocity difference between the ambient flow velocity ( $U_\infty$ ) and the measured velocity at a point. the  $x$ -axis is in the direction of flow,  $d$  is the diameter of the cylinder, and  $C_d$  is the Reynolds number dependent drag coefficient for circular cylinder.

From the measurement, Schlichting suggested the value for the empirical parameter  $\varepsilon_0$  as:

$$\varepsilon_0 = 0.0222U_\infty C_d d \quad \text{Eq. 2-14}$$

Thus, the velocity profile behind a single cylinder in steady flow is given as:

$$u_1(x, y) = 0.95U_\infty \sqrt{\frac{C_d d}{x}} \exp\left(-\frac{y^2}{0.0888C_d d x}\right) \quad \text{Eq. 2-15}$$

### 2.3.3 Near-field modification of the velocity deficit in the wake region

Schlichting's formula for the velocity deficit in the wake shows good agreement with experiments in the far-field wake (typically a distance of 80 – 100 diameters downstream). However, the velocity deficits are too large, and the wake region is too narrow in the near field wake. The spacing between the twines of the net structure is typically 5d. Therefore, modification of the original formulation has been carried out to get good results in the near-field wake [29].

Blevins [20] introduced a virtual distance to Schlichting's formulation naming it a virtual origin of the wake. In addition, the constants of the original formula were modified. The velocity deficit in a turbulent wake behind a circular cylinder placed at the origin  $x=0, y=0$  becomes

$$\frac{u_1}{U_\infty} = 1.02 \sqrt{\frac{C_d}{6 + \frac{x}{d}}} \exp\left(\frac{-\left(\frac{y}{x}\right)^2}{0.0767C_d\left(6 + \frac{x}{d}\right)}\right) \quad \text{Eq. 2-16}$$

where  $u_1$  is the velocity reduction experienced at the coordinate  $x$  and  $y$ ,  $U_\infty$  is the undisturbed flow velocity, and  $C_d$  is the Reynolds number dependent drag coefficient for a circular cylinder. Fredheim [29] validated the Virtual origin wake model by experiments and found that the model can be used to calculate the drag force on a downstream cylinder after 3.8D behind the upstream cylinder at Reynolds number from  $2.0 \times 10^4$  to  $6.0 \times 10^4$ .

## 2.4 Wake behind a screen

Løland [14] proposed a wake model for a net panel based upon the Schlichting's velocity profile formula behind a single cylinder in a steady flow (Eq. 2-15). Since the screen consists of a number of cylinders (net twines), the contributions to the wake from individual cylinders within the screen are summed, neglecting the hydrodynamic interaction between the cylinders. This is a reasonable assumption when  $l_t/d_t > 5\sim 6$ , where  $d_t$  is the diameter of cylinder and  $l_t$  is the mesh size (Fig. 2-3), but the screen should be assumed to be rigid. The drag coefficient for a screen is considered to have a consistent solution for the current force as follows:

$$\begin{aligned}
 F_D &= \sum_{i=0}^N F_{d,i} \\
 \frac{1}{2} \rho C_D U_\infty^2 A &= \sum_{i=0}^N \frac{1}{2} \rho C_d U_\infty^2 d_i l_i \\
 C_d &= \frac{C_D A}{\sum_{i=0}^N d_i l_i}
 \end{aligned}
 \tag{Eq. 2-17}$$

where  $F_D$  is the drag force for a screen,  $F_d$  is the drag force for a twine,  $C_D$  is the drag coefficient for a screen,  $C_d$  is the drag coefficient for a twine,  $A$  is the area for a net panel,  $d_i$  is the diameter of the  $i^{\text{th}}$  twine,  $l_i$  is the mesh size of  $i^{\text{th}}$  twine,  $U_\infty$  is the flow velocity,  $\rho$  is the density of the fluid, and  $N$  is the total number of twines.

The velocity profile of the wake behind a screen is derived based on equations Eq. 2-15 and Eq. 2-17 as follows:

$$\begin{aligned}
 \frac{u(x, y, z)}{U_\infty} &= 1.0 - 0.95 \sum_{i=0}^{N_i} \sqrt{\frac{C_{d,i} d_i}{x - x_i}} \exp\left(-\frac{(y - y_i)^2}{0.0888 C_{d,i} d_i (x - x_i)}\right) \\
 &\quad - 0.95 \sum_{j=0}^{N_j} \sqrt{\frac{C_{d,j} d_j}{x - x_j}} \exp\left(-\frac{(z - z_j)^2}{0.0888 C_{d,j} d_j (x - x_j)}\right)
 \end{aligned}
 \tag{Eq. 2-18}$$

where  $N_i$  is the number of twines in  $y$ -direction,  $N_j$  is the number of twines in the  $z$ -direction,  $C_{d,i}$  is the drag coefficient for a  $i^{\text{th}}$  twine,  $C_{d,j}$  is the drag coefficient for a  $j^{\text{th}}$  twine, coordinates  $x, y, z$  are the field point for calculation of velocity, and  $x_i, y_i, z_i$  are the source point of the screen element.

The comparison between the model test and the computed value from the Eq. 2-18 showed a good agreement [14]. The velocity in the near wake field (1~2 times the dimension of the net) showed that the velocity in the wake was constant except the flanks of the wake region.

# Chapter 3

## Numerical method

---

### 3.1 FhSim Framework

The software used in this thesis is FhSim, which is a numerical program developed by SINTEF Ocean, and it is capable of performing dynamic simulations of marine structures under different environmental conditions. Fig. 3-1 shows a general overview of the FhSim system architecture. The software builds a model structure interconnecting several sub-models. The sub-models are called simulation objects, or for short, “SimObjects.” These objects are defined by states associated with ordinary differential equations (ODEs) to describe their dynamic responses. The interconnections between the objects are carried out by the software component “External ports” of the FhSim, facilitating the necessary exchange of information. In each time step, the states of the objects are tracked and updated by “Integrator” using several eligible integration methods [32]. In this thesis, the Forward Euler integration method is used for numerical simulations.

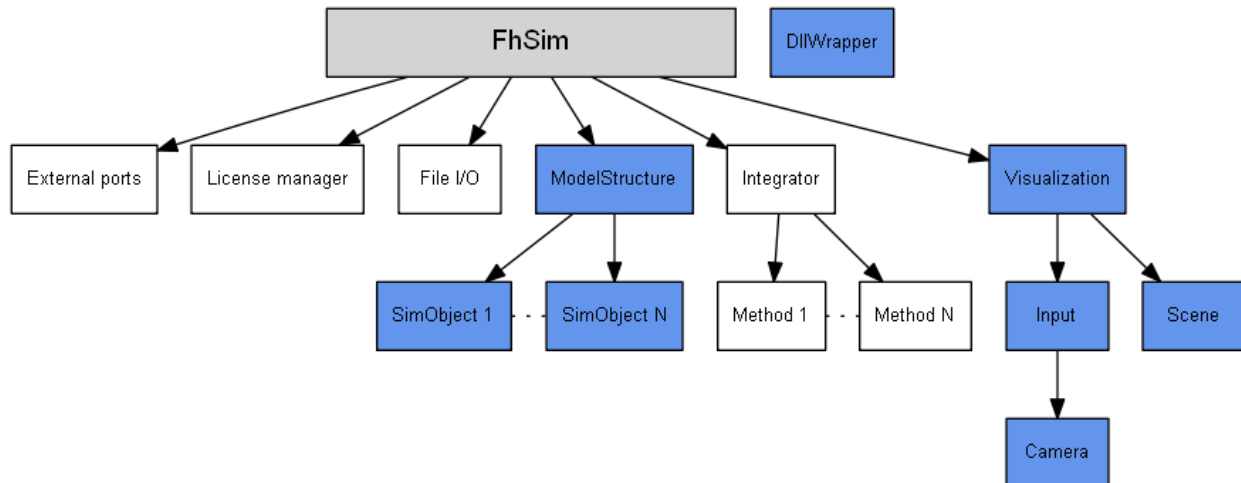


Fig. 3-1: Overview of the FhSim architecture [33].

In the present thesis, the FhSim framework is utilized to study the responses of the fish farm models (single-cage and multi-cage models). Fig. 3-2 represents how variables are transferred across objects in a fish cage model during numerical analysis in FhSim. The position and velocity variables of an object are its output ports, while the force variable is its input port. A newly compiled “Mooring” module (the dashed box in Fig. 3-2) is implemented in the existing program. By applying the new module, the initial setup and the exchange of forces become efficient since all the objects in the mooring system are packed into one module thus, the computational effort is greatly reduced [34].

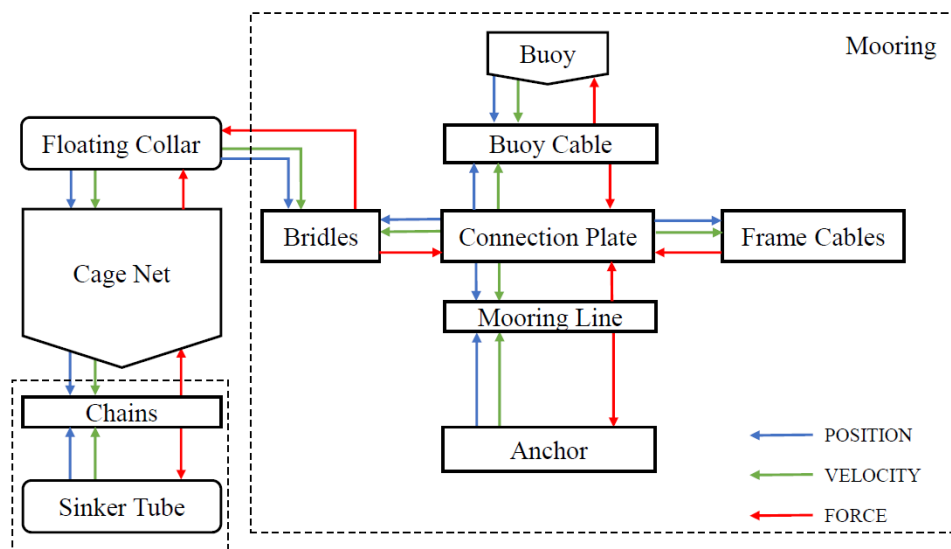


Fig. 3-2: Flow chart for the transfer of variables across interconnected sub-models during the numerical analysis [34].

The volume of a cage is computed utilizing the tetrahedron volume integration method. As shown in Fig. 3-3, the cage is considered as a cylindrical cake that has  $M$  layers and  $N$  slices from top to bottom, and a piece is extracted and divided into three tetrahedrons [35]. Three vectors,  $\vec{A}$ ,  $\vec{B}$ , and  $\vec{C}$  are assigned along the sides of the tetrahedron by choosing one point as an origin. The volume of the small piece of cake can be computed using the principle of the scalar triple product (Eq. 3-1). Subsequently, the volume of a cage is obtained by summing up all the volumes of tetrahedrons. In the present study, each fish cage is decomposed into ten layers and 32 slices, and thus, 960 tetrahedrons.

$$\begin{aligned}
 V_{cage} &= \frac{1}{6} \|A \cdot (B \times C)\| \\
 &= \frac{1}{6} [(a_1(b_2c_3 - c_2b_3) + a_2(b_3c_1 - c_3b_1) + a_3(b_1c_2 - c_1b_2))]
 \end{aligned}
 \tag{Eq. 3-1}$$

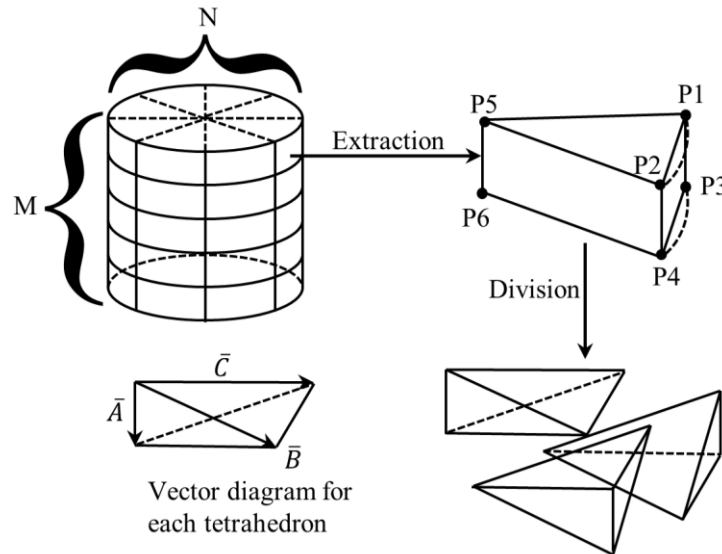


Fig. 3-3: Tetrahedron volume integration method [35].

## 3.2 Structural model

The mathematical sub-models representing the physical components of a fish cage are included in FhSim, such as net structure, floating collar, sinker tube, buoy, and cables. The numerical simulations of a fish cage containing these sub-models have been validated extensively against experiments [19], [36]. The validations for the drag force on net structure showed satisfactory results under low current velocities (0.21 to 0.33 m/s), where the deviations between the numerical and experimental results are as low as 7% [19]. General descriptions of sub-models are provided as follows:

### 3.2.1 Net structure

The net structure of the fish cage is discretized utilizing the triangular elements developed by Priour [37]. In this method, the triangular element is assumed to have constant material properties and geometry within the element, and the twines of the net have two directions ( $u$  and  $v$ ) in which all twines in each direction are parallel, as shown in Fig. 3-4. All the triangular elements in net structure are interconnected through nodes, and the total mass of the structure distributed onto the nodes. The hydrodynamic forces exerted on the triangular element, are computed as a summation of loads acting individual twines within the element and distributed onto the nodes [38]. With all the other external forces acting on the net element such as gravitational force, and external forces from other sub-model connected to the net structure, acceleration of the node is computed together with the lumped mass and added mass for each time step. Then the position and velocity are obtained from the acceleration of the node simulating the deformation and displacement of the net structure [36].

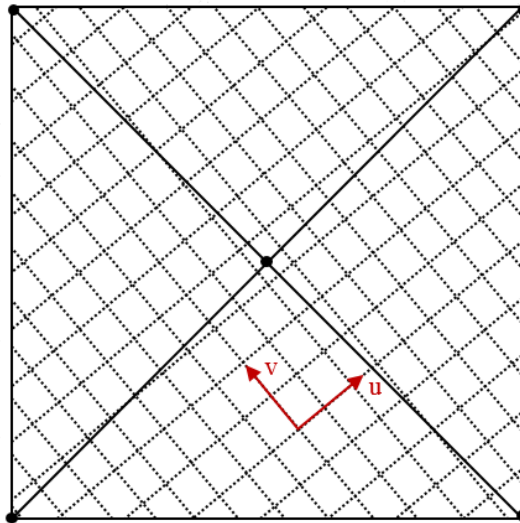


Fig. 3-4: Triangular element used for the net structure.

In the present study, the net structure comprises of 321 nodes and 608 triangular elements in each fish cage. A single layer is formed by a set of 32 nodes that are evenly distributed along with the circumference of the structure, as shown in Fig. 3-5. There are ten such layers along with the cage depth, and a single node is present at the cone-tip.

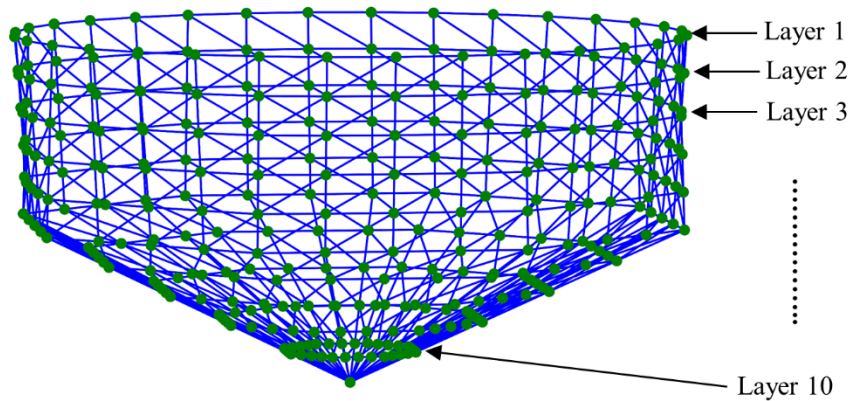


Fig. 3-5: Illustration of triangular elements for net structure.

### 3.2.2 Floating collar

The floating collar is modeled as a flexible circular ring with 6 degrees of freedom using beam elements. Elastic deformation induced by bending is considered, and the forces acting on the collar are wave excitation force (Froude-Kriloff and diffraction), structural force, hydrodynamic force, and damping force. Euler beam theory is used to compute the radial and vertical responses [36]. The floating collar serves as the hang-off point for the net structure and has 32 net connections corresponding to nodes of the first layer of net structure.

### 3.2.3 Cables

The components such as bridles, frame cables, and mooring lines are modeled using rigid bar elements. They are provided with material properties such as length, weight, diameter, Young's modulus, and the number of elements within the cable. Each end of the cable is connected to another sub-model or a fixed point in space. Thus, the interactions with other sub-models are accounted. The cable models are provided with constraint equations to achieve desired structural properties such as bending, axial, and torsional stiffness [36].

### 3.2.4 Buoy

The buoy is modeled as a shape with a vertical cylinder and cone attached to it. The tip of the cone is pointing downwards. The external forces acting on the buoy are the forces transferred from other-sub models, gravitational force, and the hydrodynamic forces. The hydrodynamic forces are computed over the submerged area of the buoy. The forces transferred from other sub-models are exerted on buoy through the buoy cable, which is attached to the submerged steel plate underneath the buoy. The buoy cable is connected to the tip of the cone at the bottom. Therefore, the buoy does not generate any great moment around the z-axis of the buoy. In other words, the buoy model is limited to 5 degrees of freedom [36].

### 3.2.5 Sinker tube

The sinker tube is modeled using a generic cable model connecting two endpoints. The input parameters such as axial stiffness, bending stiffness, and torsional stiffness are included to describe the responses of the model. In addition, the input variables, such as the radius of the tube, length, and mass per unit length, are provided to initialize the model. The model is subjected to hydrodynamic forces, gravitational force, and the forces transmitted from other sub-models connected to the sinker tube. The total external forces acting on the sinker tube are computed as a summation of the forces exerted on each cable element. Each force on the element is considered to act on the center of geometry [36].



### 3.3 Implementation of wake effects

Wake effects are essential and complex in analyses of permeable structures, such as the net structure of a fish cage, since they can alter the incoming flow velocity at a downstream structure by the presence of upstream structures. As the hydrodynamic force acting on the twine is proportional to the square of the flow velocity, it is imperative to discern the variation of the flow velocity to obtain precise force prediction. The wake region in a multi-cage system is decomposed into two domains for ease of implementation (see Fig. 3-6). One is within a cage, and the other is outside of a cage. The former comprises two wake effects, twine-to-twine wake effect and net-to-net wake effect. The latter is the cage-to-cage wake effect.

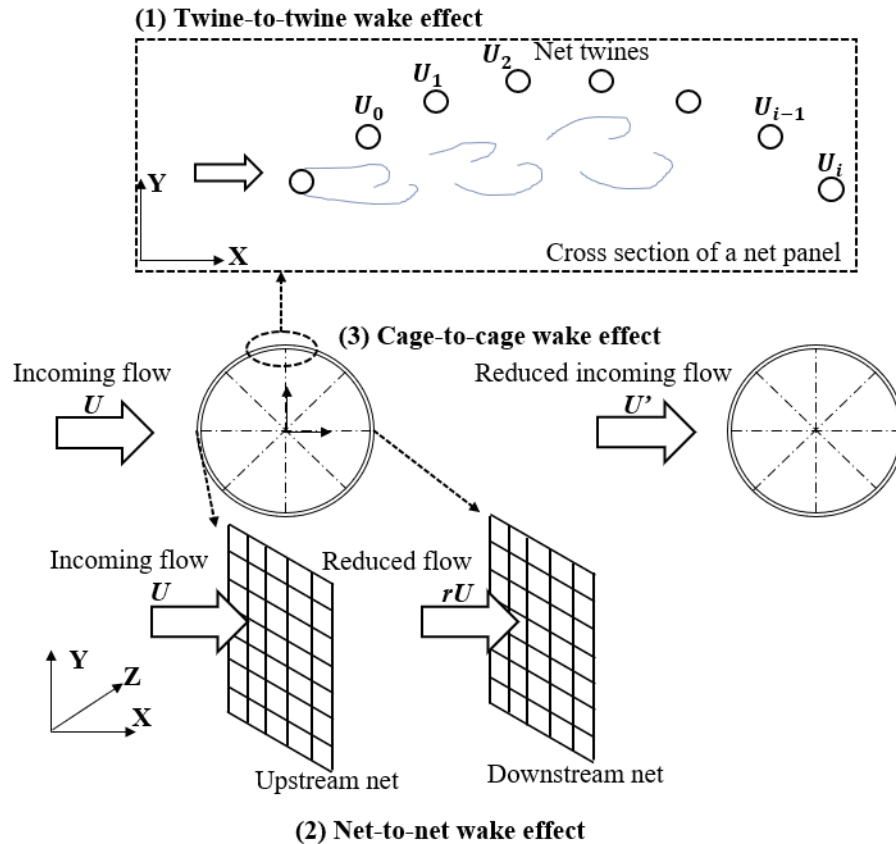


Fig. 3-6: Illustration of different wake effects [39]. (1) Twine-to-twine wake effect, where a grid of  $i+1$  cylinder (cross-section of a net panel) are exposed to an incident flow velocity  $U$ . The  $U_i$  ( $i = 0, 1 \dots$ ) denotes the velocity experienced by cylinder  $i$ , which is modified due to the presence of upstream cylinders. (2) net-to-net wake effect, where the upstream (left) net panel is exposed to an incoming flow velocity  $U$ . The net-to-net wake effects from the upstream net panel result in a reduced flow ( $rU$ ) at the downstream net panel. (3) Cage-to-cage wake effect, where the reduced incoming flow for the downstream (right) fish cage is anisotropic and smaller than the incoming flow for the upstream (left) fish cage.

### 3.3.1 Twine-to-twine wake effect

Twine-to-twine wake effect accounts for the interaction between the twines in a net panel. This effect has an influence region in the order of centimeters (see Fig. 3-6). Endresen *et al.* [19] proposed a method to take the interaction between twines into account for computation of the hydrodynamic forces on a net structure using Morison type force model. Blevins virtual origin formula (Eq. 2-16) [20] is used to achieve a function describing the flow pattern behind a cylinder [39]. Therefore, the wake effects for the locations where net twines are in tandem or staggered position due to geometry or deformation of the net structure are accounted.

### 3.3.2 Net-to-net wake effect

The net-to-net wake effect represents the interaction between net panels in a single fish cage. This effect has an influence region in the order of tens of meters (see Fig. 3-6). Approximately half of the net panels in a cylindrical fish cage are in the wake region of the upstream net panels [39]. The velocity reduction factor,  $r = 1 - 0.46C_D$ , is introduced to FhSim to represent the net-to-net wake effect, where  $C_D$  is the drag coefficient of a net panel when the flow is perpendicular to it. A uniform shape of the wake is formed behind a net using the velocity reduction factor  $r$  [14].

$$U_{downstream} = rU_{upstream} \quad \text{Eq. 3-2}$$

A part of the net structure that would experience the reduced velocity is determined by its position, flow direction, and the center of the fish cage [39]. The velocity reduction factor is applied to reduce the incoming flow velocity for the downstream net panels. As shown in Fig. 3-7, the net placed in the region colored in blue experience the reduced velocity.

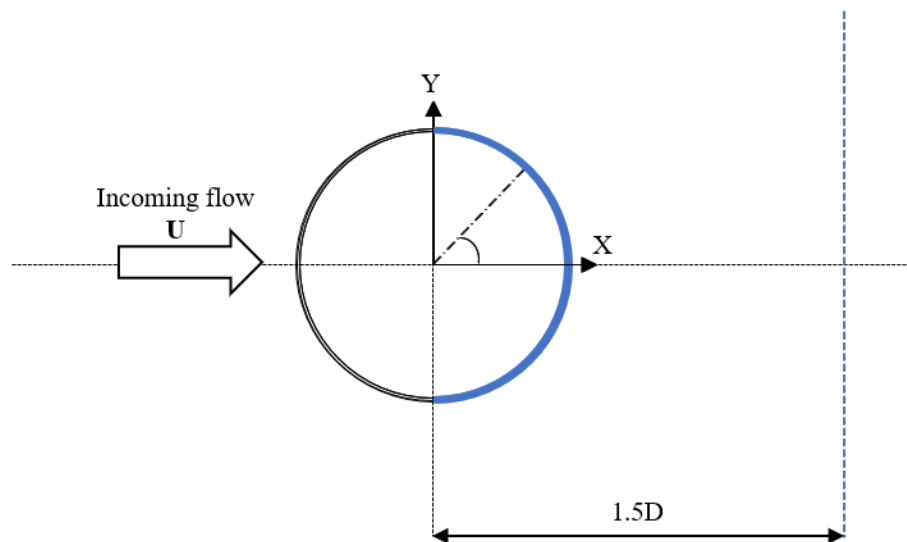


Fig. 3-7: Illustration of the method to identify the nets which experience the net-to-net wake effect [39].

### 3.3.3 Cage-to-cage wake effect

The cage-to-cage wake effect represents the interaction between fish cages. This effect has an influence region in the order of a few hundred meters (see Fig. 3-6). The fish cages are usually grouped to form an array as a fish farm in the marine aquaculture industry [39]. The flow experienced by the downstream cages is affected by the existence of the upstream cage, mainly because of two effects. One is the blockage of the flow, which makes the water go around the cage, and the other is the wake formed by the inflow through the net cage since recirculation and backflows occur in the region [19]. In the present study, the alteration of flow field behind a circular net structure is realized by a curve fitting according to the experiment done by Gansel *et al.* [17]. Fig. 3-8 shows the velocity defect factor along a horizontal line (the blue dash line in Fig. 3-7) at  $1.5D$  behind a fish cage which is symmetrical about  $Y/D = 0$ . With the increasing distance to the axis of symmetry, the flow defect factor first decreases and then becomes steady. When the distance to the axis of symmetry is approximately  $0.65D$ , the velocity reaches the undisturbed velocity (the same as incoming flow velocity). When the distance to the axis of symmetry exceeds  $0.65D$ , the flow velocity is slightly higher than the incoming velocity due to the conservation of mass. The blue curve in Fig. 3-8 is a Fourier series as given in Eq. 3-3.

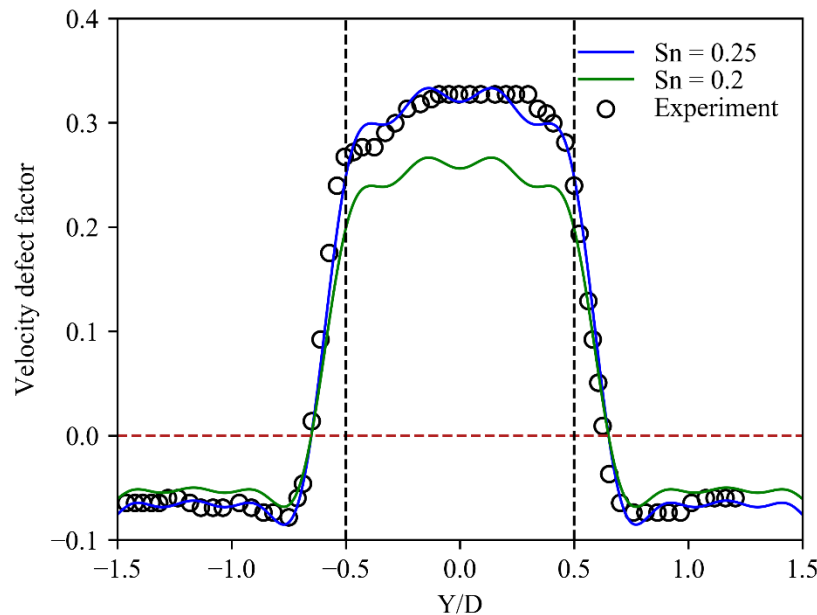


Fig. 3-8: Velocity profile  $1.5D$  downstream behind a fish cage according to the experiment done by Gansel *et al.* [17]. Black circles represent the experimental data with a solidity ratio of 0.25, the blue line is the curve fitting to the data, and the green line is the scaled velocity profile for a solidity ratio of 0.2.  $Y$  is the axis perpendicular to the flow direction,  $D$  is the diameter of the fish cage.

$$\begin{aligned}
V_r = & 0.1201 + 0.2414\cos(\omega y/D) + 0.0115\cos(2\omega y/D) - 0.0644\cos(3\omega y/D) \\
& + 0.0030\cos(4\omega y/D) + 0.0294\cos(5\omega y/D) - 0.0058\cos(6\omega y/D) \\
& - 0.0149\cos(7\omega y/D)
\end{aligned} \quad \text{Eq. 3-3}$$

Where  $\omega = 2.692$ . In the present study, the width of the wake region behind a cage is implemented as 2D thus,  $-1 < y/D < 1$ . The velocity profile in Eq. 3-3 is then extended to different solidity ratios and distances behind an upstream fish cage as Eq. 3-4.

$$V_{decay} = V_r \cdot \frac{S_n}{0.25} \sqrt{\exp\left(-\frac{x/D - 1.5}{25}\right)} \quad \text{Eq. 3-4}$$

Where  $V_r$  represents the velocity defect factor when  $S_n = 0.25$ ,  $S_n$  is the solidity ratio of the net. In addition, the reduced velocity factor decays as it propagates downstream,  $x/D$  is the nondimensionalized distance after the upstream fish cage in the flow direction.  $V_{decay}$  represents the velocity defect factor at different coordinates after a fish cage and is used in the present study. The incoming flow for the downstream cage,  $U'$ , is calculated by Eq. 3-5, where  $U$  is the incoming flow for the upstream cage.

$$U' = (1 - V_{decay})U \quad \text{Eq. 3-5}$$

## 3.4 Structural failure

In the numerical models used in Chapter 5, a function to control where and when the structural failure in the frame cable and mooring line occurs is implemented into the existing program, FhSim. For the failure cases, a simulation under an intact condition is run until it reaches a steady-state, and then the connection relationship between the elements is removed at the desired position to fulfill the accidental failure in the target cable.

## Chapter 4\*

# **Numerical investigation on the cage-to-cage wake effect: A case study of a 4x2 cage array**

---

In this chapter, the interactions between fish cages are implemented into the numerical program, FhSim, to investigate the influence of wake effects on the responses of a multi-cage fish farm. Structural responses such as tension in mooring line, drag force, and cultivation volume of each cage in a full-scale 4x2 cage array under different flow directions are analyzed numerically. The discrepancies of the responses between three cases, *i.e.*, (i) without wake effects, (ii) with only cage-to-cage wake effect, and (iii) with all the wake effects, are compared and discussed. The results indicate that neglecting the wake effects would overestimate the total drag force of the eight cages and underestimate the total cultivation volume of the eight cages significantly for various flow conditions. This study can provide suggestions on how to consider the wake effects during the design of the multiple-cage system.

---

\* The contents of this chapter are included in the paper [40] which is accepted for publication in Proceedings of the ASME 2020 39th International Conference on Ocean, Offshore and Arctic Engineering. The paper has been submitted to the Journal of Offshore Mechanics and Arctic Engineering.

## 4.1 Model set-up

A type of fish cage chosen for the present study is by far the most widely adopted type of fish cage in the aquaculture industry, namely, a flexible gravity-based fish cage. The flexible gravity-based fish cage consists of a floating collar, net structure, sinker tube, and mooring system. The general overview of the flexible gravity-based fish cage is provided in Section 1.2.2. Dimensions and properties of the material used for a single-cage model are given in Table 4-1. The identical fish cells are used to form a multi-cage fish farm model.

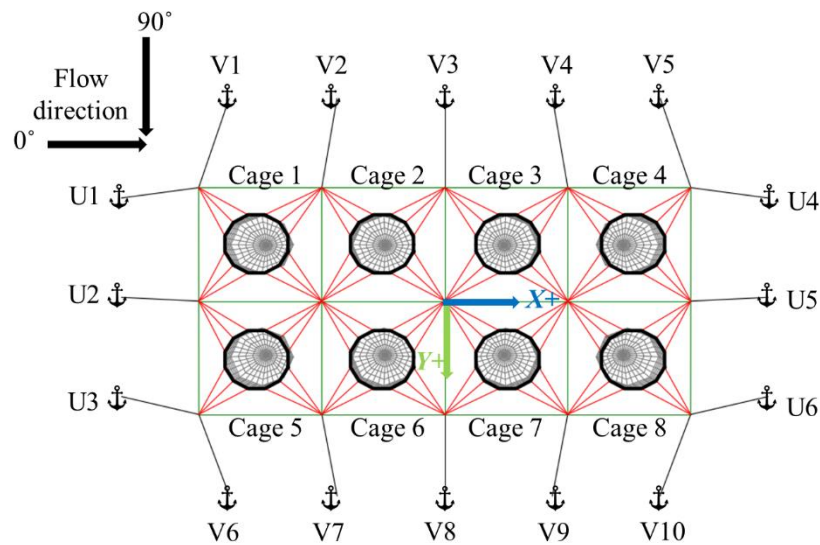


Fig. 4-1: Configuration of 4x2 multi-cage fish farm layout.

Fig. 4-1 shows the plan view of a multiple-cage system with a 4x2 configuration, which is used in the analysis of the implementation of wake effects. The blue and green arrows on the center of the multi-cage array represent the global coordinate system as the  $X$  and  $Y$  axes. The  $Z$ -axis is pointing into the paper. The eight cages are numbered in order from 1 to 8 along the positive  $X$ -axis. The mooring lines are denoted with U1-U6 and V1-V10. The black lines in the figure represent the mooring lines, the green lines represent the frame cables, and the red lines represent the bridles. The flow directions of  $0^\circ$  and  $90^\circ$  are expressed as black arrows on the upper left corner of the figure.

Table 4-1: Dimensions and properties of the fish cage used in this thesis.

<b>Sub model</b>	<b>Parameter</b>	<b>Value</b>	<b>Unit</b>
<b>Floating Collar</b>	Inside diameter	51	m
	Outside diameter	53	m
	Section diameter	0.25	m
	Wall thickness	28.4	mm
	Young's modulus	0.9	GPa
<b>Net structure</b>	Linear density	81	kg/m
	Twine diameter	2.5	mm
	Size of mesh	25	mm
	Density	1125	kg/m <sup>3</sup>
	Young's modulus	0.1	GPa
	Vertical cylinder depth	15	m
<b>Sinker Tube</b>	Conical bottom depth	28	m
	Tube diameter	51	m
	Section diameter	0.25	m
	Center point weight	100	kg
	Linear density	51	kg/m
<b>Buoy</b>	Diameter	2	m
	Vertical cylinder depth	1	m
	Conical bottom depth	2	m
<b>Mooring line</b>	Length	120	m
	Diameter	0.05	m
	Young's modulus	1.0	GPa
<b>Frame cable</b>	Length	100	m
	Diameter	0.05	m
	Young's modulus	1.0	GPa
<b>Bridle</b>	Length (center)	50	m
	Length (side)	46	m
	Diameter	0.05	m
	Young's modulus	1.0	GPa

The depth of the net structure is divided into two parts (“Vertical cylinder depth” and “Conical bottom depth” in Table 4-1) since the shape of the net structure consists of the cylindrical body attached to the floating collar and the conical body at the bottom. The term “Length (center)” for bridle in Table 4-1 refers to the length of the middle cable among three bridles on each corner of the fish cell, and “Length (side)” refers to the length of the other two bridles.

## 4.2 Environmental loading

Environmental condition is considered as a pure current condition in the numerical analysis. Ten flow directions (from  $0^\circ$  to  $90^\circ$  with  $10^\circ$  interval) are applied with a flow velocity of 0.5 m/s to investigate how the wake effects affect the structural responses of a multi-cage fish farm. The influence of the wake effects on (1) drag forces and cultivation volumes of individual fish cages, (2) total drag forces and cultivation volumes of the eight cages, (3) tensions in the mooring lines are compared and discussed based on the simulation matrix listed in Table 4-2. For each flow direction, a time-domain simulation of 500 seconds is performed. The structural responses used for discussions are taken as the average value after the simulation reached equilibrium. As shown in Fig. 4-2, the volume of a fish cage converges to a stable value approximately after 300 seconds. Thus, 500 seconds are long enough for the responses to reach equilibrium.

Table 4-2: Simulation matrix.

	Wake effect selection	Flow direction	Flow velocity
<b>Case 1</b>	without wake effects	$0^\circ$ to $90^\circ$	0.5 m/s
<b>Case 2</b>	with only cage-to-cage wake effect	$0^\circ$ to $90^\circ$	0.5 m/s
<b>Case 3</b>	with all the three wake effects	$0^\circ$ to $90^\circ$	0.5 m/s

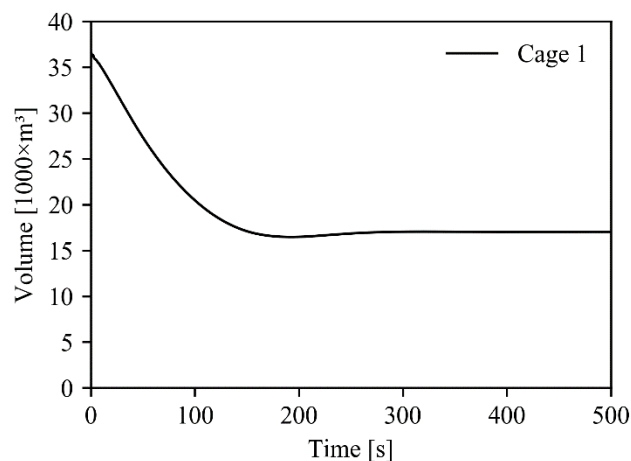


Fig. 4-2: Time history for the estimated cage volume of Cage 1 with an incoming flow velocity of 0.5 m/s and  $0^\circ$  flow direction.



## 4.3 Wake effects on drag forces and cultivation volumes of fish cages under different flow directions

### 4.3.1 Case 1 (without wake effect)

Without wake effects, the blockage and alteration of the flow field after the permeable net structure are neglected. All the fish cages are exposed to the same flow conditions, and thus, every triangular element on fish cages experiences the same flow velocity. Therefore, as shown in Fig. 4-3, the drag force and the cultivation volume of the eight fish cages are equal. In addition, due to the cylindrical shape of the fish cage, the drag force and cultivation volume become constant regardless of the flow direction (see Table A-2 and Table A-5 in Appendix).

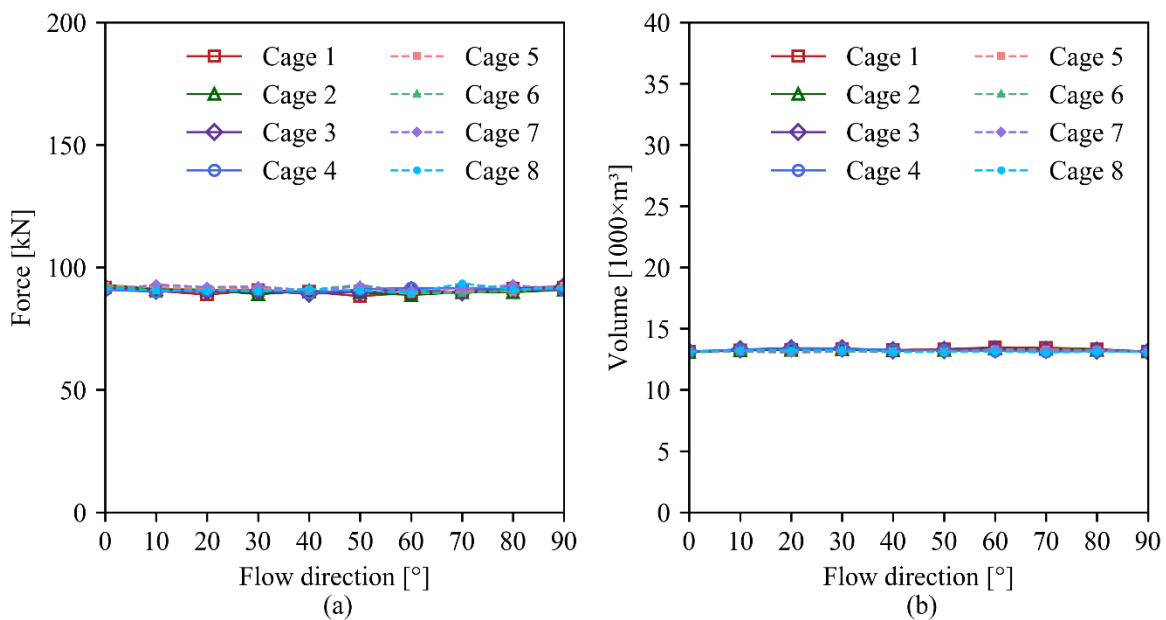


Fig. 4-3: Drag force and cultivation volume of cages (Case 1). (a) Drag force of the individual fish cages without wake effects. (b) Cultivation Volume of the individual fish cages without wake effects.

### 4.3.2 Case 2 (with only cage-to-cage wake effect)

In Case 2, the alteration of the flow field is realized by implementing the cage-to-cage wake effect according to Section 3.3.3. The two internal wake effects are not considered. As shown in Fig. 4-4 (a), with the changing flow direction, the drag force of Cage 1 is unchangeable and keeps the same value as that in Case 1. The reason is that in both Case 1 and Case 2, no matter under which flow direction, Cage 1 always experiences the same flow velocity without any disturbance from the other cages. Except for Cage 1, the flow velocities experienced by other fish cages vary with the changing flow direction and different from that under the corresponding condition in Case 1. Therefore, fish cages at different positions experience different ambient flow velocities, and thus, drag force and cultivation volume of the individual cages can differ from each other. The computed cultivation volume and drag force of all cages are presented in Appendix A.

As shown in Fig. 4-4, the drag force and cultivation volume of an individual fish cages are highly correlated, as larger cultivation volume comes with lower drag force. This relation is also seen in previous researches [14], [18], [35], and [34].

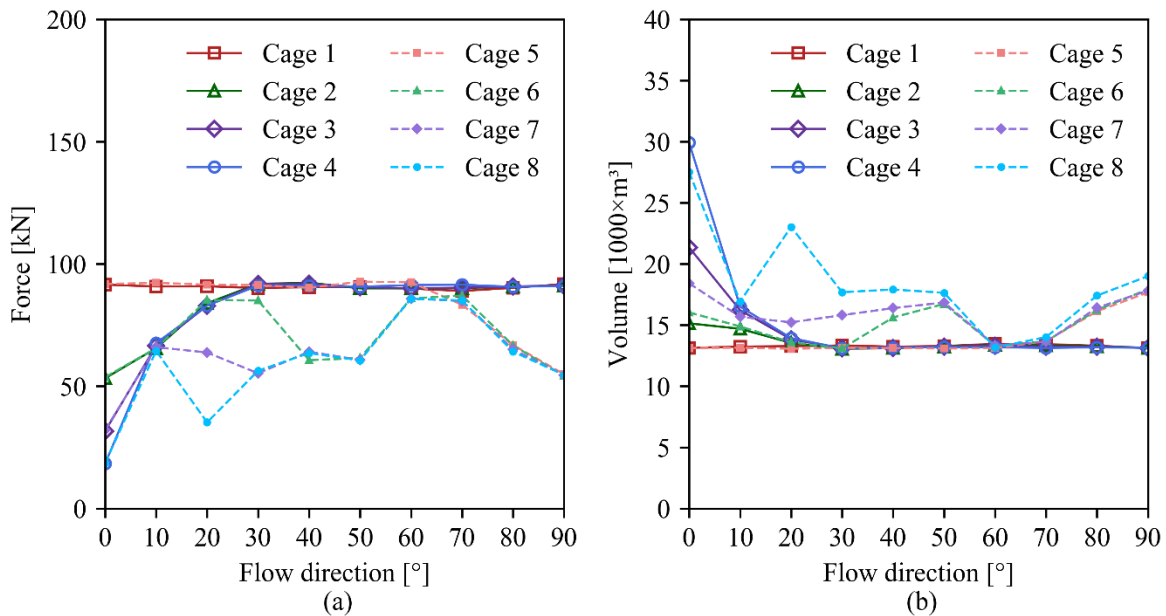


Fig. 4-4: Drag force and cultivation volume of cages (Case 2). (a) Drag force of the individual fish cages with only cage-to-cage wake effect and (b) Cultivation Volume of the individual fish cages with only cage-to-cage wake effect.

When the flow direction is  $0^\circ$ , the drag forces of the cages which are symmetric about the X-axis have the same value, *e.g.*, Cage 1 and Cage 5 have the same drag force when the flow direction is  $0^\circ$ . Because the flow comes along the X+ direction and the grid-like multi-cage fish farm is also symmetric about the X-axis, the cages which are symmetric about the X-axis experience the same flow velocity. Due to the existence of a cage-to-cage wake effect, the downstream fish cages experience a reduced flow velocity. Thus, the drag forces on Cage 2, 3, and 4 are reduced by 39%, 62%, and 76%, respectively (see Table 4-3) and the cultivation volume of the cages are changed accordingly, as shown in Fig. 4-5.

Table 4-3: Drag force of cages for Case 1 and Case 2 (flow velocity = 0.5 m/s, flow direction =  $0^\circ$ ).

	<b>Cage 1</b>	<b>Cage 2</b>	<b>Cage 3</b>	<b>Cage 4</b>	<b>Cage5</b>	<b>Cage 6</b>	<b>Cage 7</b>	<b>Cage 8</b>
<b>Case 1 [kN]</b>	91.8	92.9	91.2	90.9	92.6	92.3	90.5	91.4
<b>Case 2 [kN]</b>	91.5	53.3	31.6	18.4	91.8	53.7	32.1	18.5
<b>Discrepancy [%]</b>	0.3	42.6	65.3	79.8	0.9	41.8	64.5	79.8

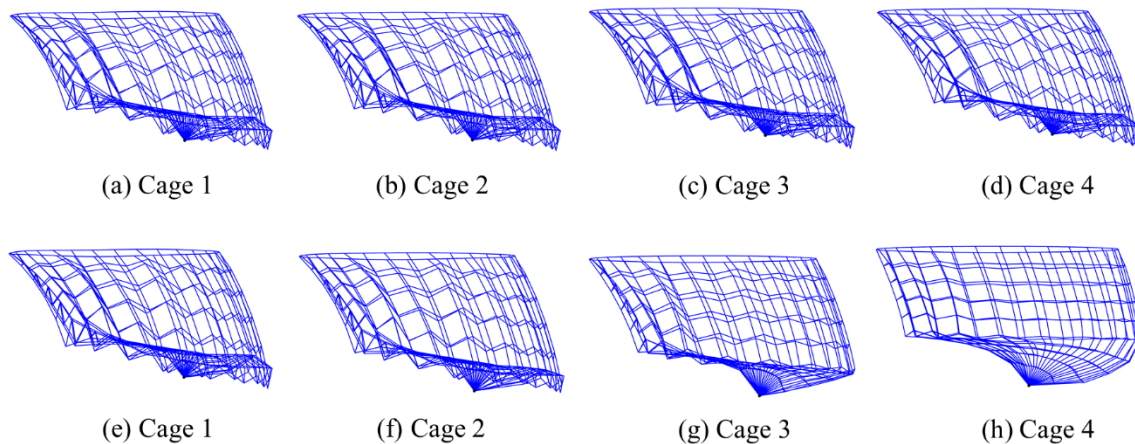


Fig. 4-5: Deformed state of cages for Case 1 and Case 2. Figure on the upper row (a) to (d) represents the deformed state of cages under Case 1 and from (e) to (h) shows the deformed state of cages under Case 2. For both cases, the flow condition is the same (flow velocity = 0.5 m/s, flow direction =  $0^\circ$ ).

With the increasing flow direction, the influences of cage-to-cage wake effect on Cage 2, 3, and 4 are reduced. As described in Section 3.3.3 and Eq. 3-3, the width of the wake region after a cage is twice the diameter of a fish cage in the present numerical model. Hence, the influence of the upstream cages on the flow field around the downstream cages (*e.g.*, the influence of Cage 1 onto Cage 2) vanishes once the flow direction exceeds  $48.6^\circ$  as illustrated in Fig. 4-6. However, the width of the velocity decreasing zone within the velocity profile after a permeable net structure is found as approximately  $1.3D$  as the flow velocity reaches the undisturbed flow velocity at  $\pm 0.65D$  (see Fig. 3-8). Thus, one can say that the reduction in flow velocity at a cage due to the presence of upstream cages diminishes once the flow direction exceeds a threshold angle,  $35.1^\circ$ . This agrees well with the responses (drag force and cultivation volume) of cage 2, 3, and 4 observed from Fig. 4-4, where the responses reach a similar value with Cage 1 after  $30^\circ$ . Since Cage 2, 3, and 4 shall not experience the flow velocity reduction induced by the upstream cages once the flow direction is greater than  $35.1^\circ$ , they show similar behavior as Cage 1. However, with the increasing flow direction, the influences of cage-to-cage wake effect on Cage 6, 7, and 8 are slightly complicated compared to Cage 2, 3, and 4. Because they might get influence from Cage 1, 2, 3, and 4, the drag force of Cage 6, 7, and 8 are smaller than Cage 1 in general.

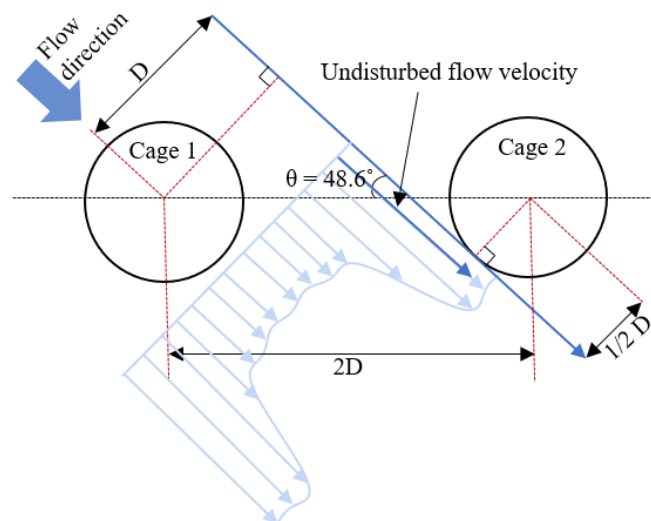


Fig. 4-6: Flow interference of upstream cage to downstream cage.  $D$  is the diameter of a cage, and the  $\theta$  is the flow direction. The illustration of the velocity profile with blue arrows is the velocity profile at  $1.5D$  downstream from a cage.

Interestingly, when the flow direction is between  $60^\circ$ - $70^\circ$ , all cages have similar drag forces and cultivation volumes. That can be explained with Fig. 4-7, where the variation of the flow field induced by the wake region is presented. The blue area behind cages represents the velocity decreasing zone, and the red area at the flanks of the wake region represents the velocity increasing zone. The downstream cages 5, 6, 7, and 8 have both blue and red colors on them, which means parts of the twines on these cages experience a reduced flow velocity and parts of them experience an increased flow velocity. Thus, if the effect of velocity increase compensates for the effect of velocity decrease, the structural responses of the downstream fish cages should be similar to that of the upstream fish cages.

When the flow direction exceeds  $70^\circ$ , the downstream Cage 5, 6, 7, and 8 start to sit in the wake regions of Cage 1, 2, 3, and 4, respectively. When the flow direction is  $90^\circ$ , the four downstream fish cages are totally in the velocity decreasing zone, and thus, the drag force is reduced to a small value. As expected, that small value is the same with the drag force of Cage 2 when the flow direction is  $0^\circ$  (see Table A-3 in Appendix A).

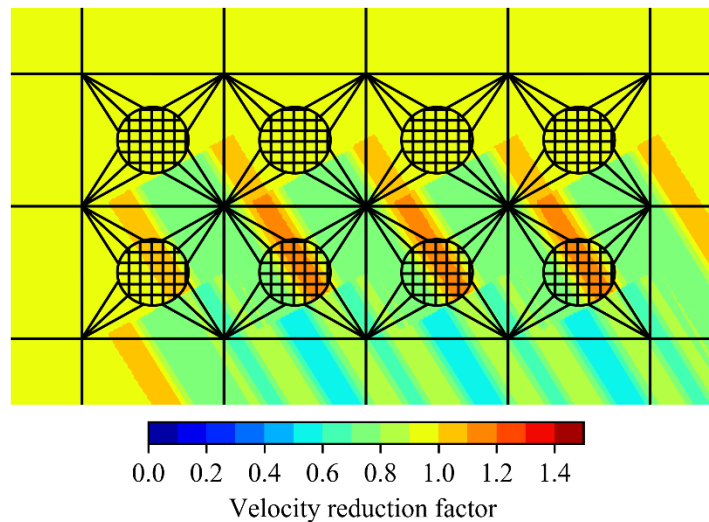


Fig. 4-7: Illustration of the velocity defect zone when the flow direction is  $60^\circ$ . The blue area behind cages represents the velocity decreasing zone, and the red area at the flanks of the wake region represents the velocity increasing zone.

### 4.3.3 Case 3 (with all the three wake effects)

In Case 3, all the three aforementioned wake effects are included in the numerical simulations. The two wake effects, *i.e.*, twine-to-twine wake effect and net-to-net wake effect, can reduce the flow velocity for the downstream twines and net panels inside a single fish cage. Therefore, the drag force of each cage is decreased, and the cultivation volume of each cage is increased compared to that under the corresponding condition in Case 2. The changes of the drag force and the cultivation volume of individual cages with changing flow direction follow a similar trend as those with Case 2. These can be observed in Fig. 4-8.

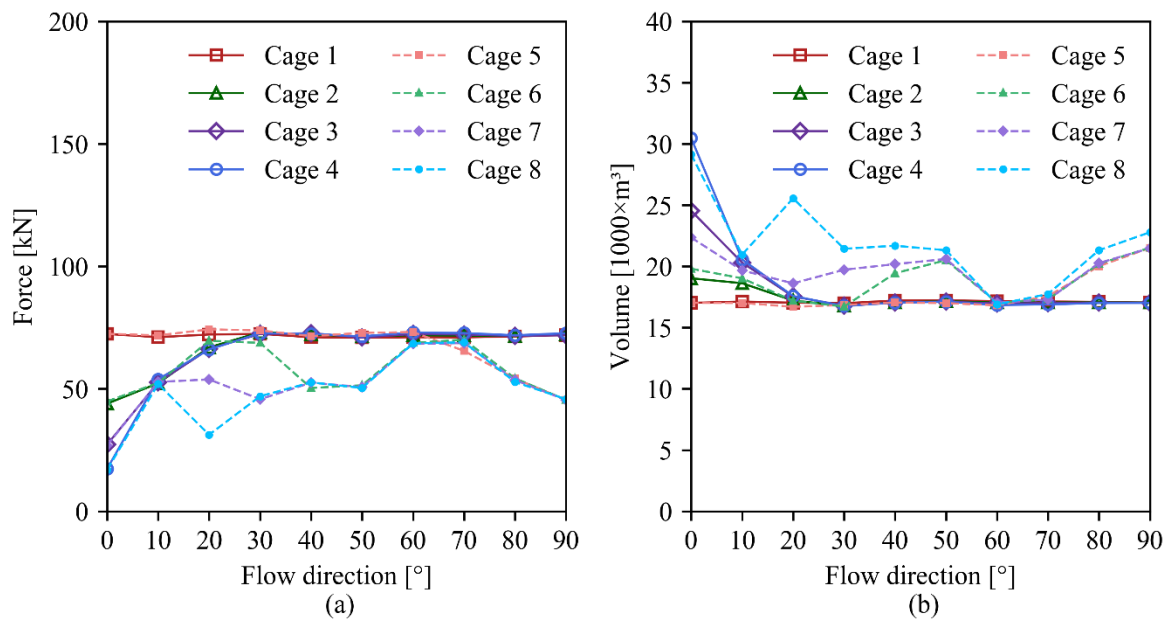


Fig. 4-8: Drag force and cultivation volume of cages (Case 3). (a) Drag force of the individual fish cages with all the three wake effects, and (b) Cultivation volumes of the individual fish cages with all the three wake effects.

### 4.3.4 Comparison between the three cases

Among all the cages, Cage 8 experiences the most significant variations in both drag force and cultivation volume. To have a better comparison between the three cases, the responses of the downstream cage, Cage 8, are discussed in this section.

The differences in the cultivation volume and drag force of Cage 8 based on the three cases are shown in Fig. 4-9. As explained in Section 4.3.1, the cultivation volume and drag force of Cage 8 based on Case 1 is constant with the flow directions. Compared to Case 3, Case 2 is always smaller, and the discrepancy between the two cases is almost constant with the flow directions. As mentioned in Section 4.3.3, that discrepancy comes from the two wake effects. The discrepancy between Case 2 and 3 for drag force at  $0^\circ$  is smaller than the other flow directions, as shown in Fig. 4-9 (b), (see Table A-3 and Table A-4 in Appendix). The reason for that might come from the twine-to-twine wake effect. The twine-to-twine wake effect varies with the angle between flow direction and the normal vector of the triangular element [19]. As the cage deforms by the current loads, the twine-to-twine wake effects are altered due to the change of this angle. The smaller the cage deforms, the less the twine-to-twine wake effect contributes, *i.e.*, the discrepancy between Case 2 and 3 is small where the incoming velocity is small enough to moderate the twine-to-twine wake effect. When the flow direction is  $0^\circ$ , it appears to have a minor change in drag force on Cage 8 since the flow passes through three cages, and the flow velocity decreases drastically. The contribution of the twine-to-twine wake effect is clearly seen when Cage 8 is compared to the cage that experiences the higher flow velocity, as shown in Fig. 4-10.

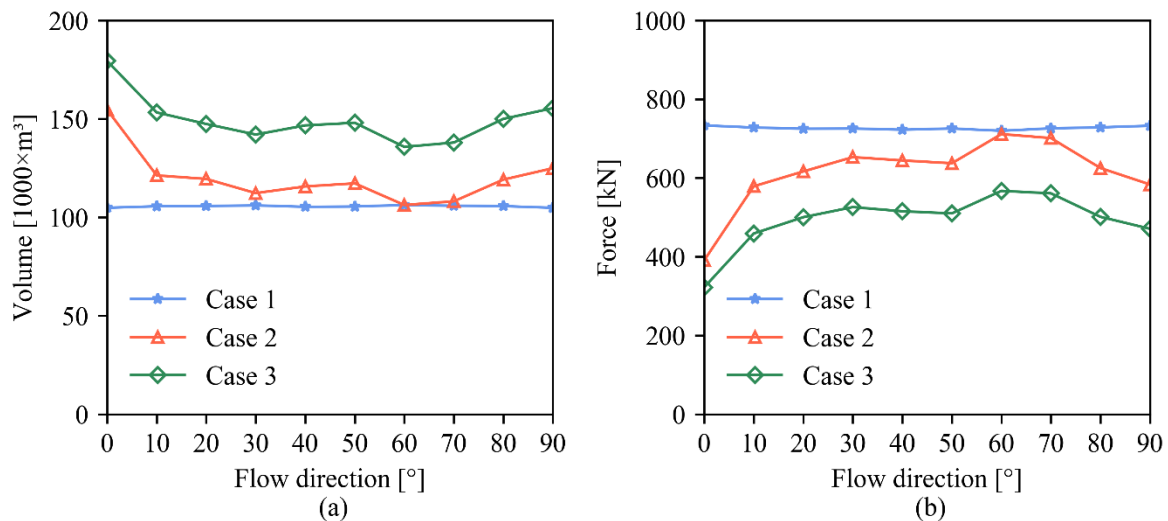


Fig. 4-9: Drag force and cultivation volume of Cage 8. (a) Comparison of the cultivation volume of Cage 8 in different cases. (b) Comparison of the drag force of Cage 8 in different cases.

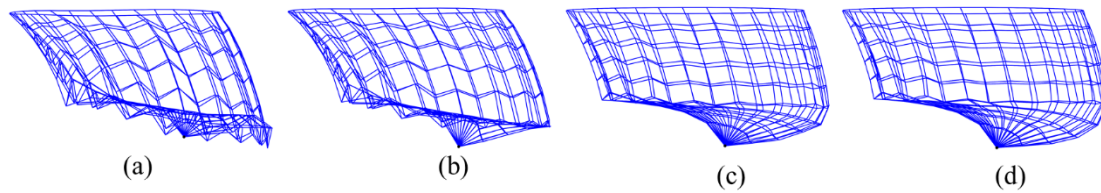


Fig. 4-10: Deformed states of Cage 5 and 8. The flow condition is considered as 0.5 m/s flow velocity and  $0^\circ$  flow direction. (a) shows the deformed state of Cage 5 for Case 2, (b) shows the Cage 5 for Case 3, (c) represents the deformed state of Cage 8 for Case 2, and (d) shows Cage 8 for Case 3.

As shown in Fig. 4-9, Cage 8 experiences a sudden change in drag force and cultivation volume when the flow direction is  $20^\circ$  for both Case 2 and Case 3. That can be explained with Fig. 4-11, where the red and blue areas illustrate the flow velocity increase and reduction due to cage-to-cage wake effect. As shown in Fig. 4-11, the blue on Cage 8 is the darkest among the eight cages, which means the ambient flow velocity for Cage 8 is the smallest. Therefore, it is reasonable that Cage 8 experiences the smallest drag force and largest cultivation volume among all cages, when the flow direction is  $20^\circ$  as the velocity decreasing zones are superimposed the most on Cage 8.

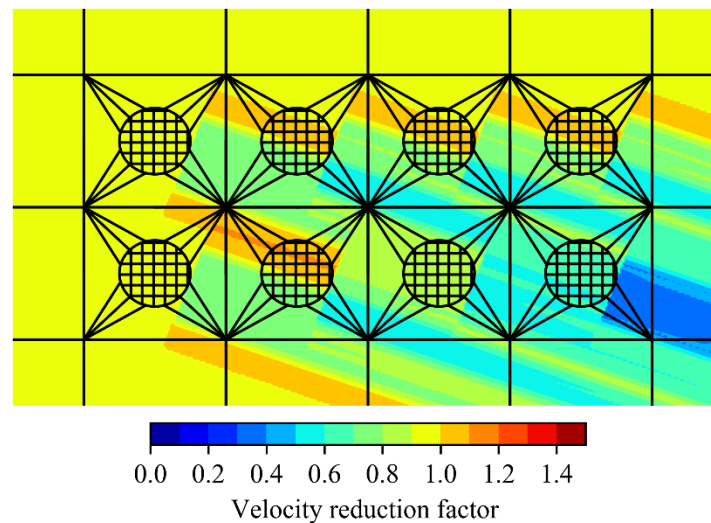


Fig. 4-11: Illustration of the velocity defect zone when the flow direction is  $20^\circ$ . The blue area behind cages represents the velocity decreasing zone, and the red area at the flanks of the wake region represents the velocity increasing zone.



## 4.4 Wake effects on the total drag force and cultivation volume under different flow directions

The total cultivation volume and drag force of all the eight fish cages are presented in Fig. 4-12 to show how the wake effects influence structural responses with different flow directions. The total cultivation volume of the eight fish cages is highly correlated with the total drag forces. The larger volume corresponds to a lower drag force. Thus, the change of the drag force with respect to the flow direction follows the opposite trend as that for the cultivation volume.

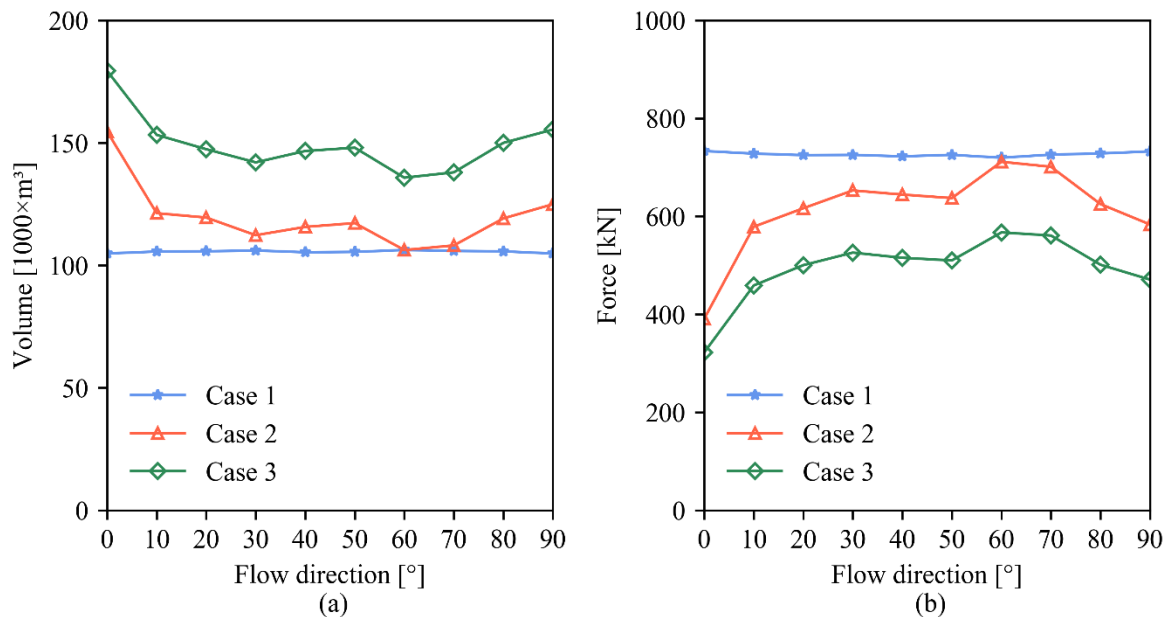


Fig. 4-12: Total drag force and cultivation volume of all cages. (a) Comparison of the total cultivation volume of all cages in different cases. (b) Comparison of the total drag force of all cages in different cases.

As shown in Fig. 4-12, the total cultivation volume and drag force in Case 1 are constant with the flow directions. Because no wake effect is applied in Case 1, each fish cage has the same flow condition for different flow directions, and thus, the sum of the drag force of each fish cage is constant with the flow directions. For the same reason, the sum of the cultivation volume of each cage is constant with the flow directions as well.

The change of the total drag force with different flow directions in Case 2 and 3 have the same trend. The total drag force first increases with the increasing flow direction when the flow direction is less than  $30^\circ$ , then keeps similar value when the flow direction is between  $30^\circ$ - $50^\circ$ , next increases to the highest value when the flow direction is  $60^\circ$ ,

---

and finally decreases when the flow direction exceeds  $70^\circ$ . The trend of the total cultivation volume follows the opposite trend as that of the total drag force. This trend of changes in total drag force and cultivation volume with different flow directions can be explained by the cage-to-cage wake effect. With the changing flow direction, the flow velocities experienced by fish cages vary, and thus, the total drag force and cultivation volume are changed. However, compared to Case 3, the total drag force of Case 2 is averagely 20% smaller, and the total cultivation volume is averagely 25% larger. These discrepancies between the two cases are almost constant with different flow directions. As explained in Section 4.3.4, these discrepancies come from the two internal wake effects, *i.e.*, twine-to-twine wake effect and net-to-net wake effect, and agree with the previous research regarding the wake effects on drag force of a single fish cage [19].

Interestingly, when the flow direction is  $60^\circ$ , the total drag force of the eight cages in Case 2 is similar to that in Case 1. As explained in Section 4.3.2, the downstream cages experience both the velocity increasing and decreasing zones. When the wake regions from different upstream cages are superimposed in a certain flow direction, the velocity reduction zone from an upstream cage might be compensated with the flanks of wake region from another upstream fish cage(s). Thus, all cages experience a similar ambient flow velocity.

## 4.5 The wake effects on tensions in anchor lines under different flow directions

The extreme tension in anchor lines (ETAL) is defined as the maximum tension in all the 16 anchor lines under a given flow direction. The sum of the environmental loads is distributed to the anchors according to the mooring system configuration and flow directions. As shown in Fig. 4-13, the maximum ETAL among all the flow directions based on Case 1, 2, and 3 are 274.5 kN, 241.3 kN, and 204.5 kN, respectively.

For Case 1, the ETAL first decreases, and then increases slightly with the increasing flow direction. As expected, the ETAL and total drag force change differently with flow directions. As shown in Fig. 4-12 (b), the total drag force in Case 1 is constant with flow directions, that means the same amount of current load is distributed to the anchor lines. Because the number of anchor lines which contribute to holding the current load varies as the flow direction changes, ETAL changes with flow directions. Therefore, the change of ETAL with different flow directions in Case 1 only comes from the different tension distributions among the anchor lines.

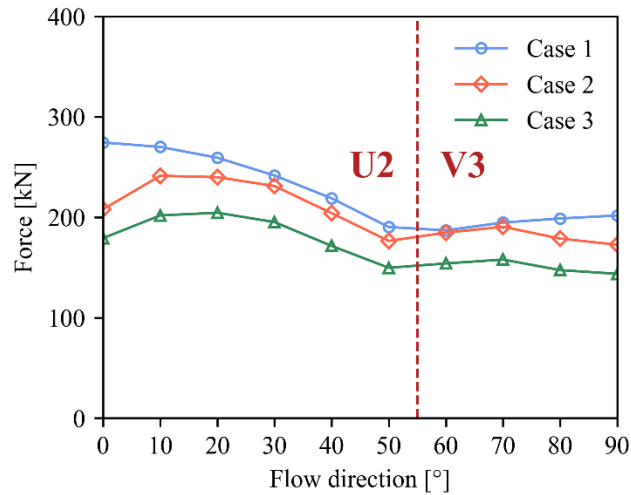


Fig. 4-13: Comparison of ETAL based on the three cases when the ambient flow velocity is 0.5 m/s. The ETAL occurs in U2 when the flow direction  $< 50^\circ$  and in V3 when the flow direction  $> 50^\circ$ .

For Case 2 and 3, the change of ETAL with different flow directions has the same trend. With the increasing flow direction, ETAL increases at the beginning then reduces until  $50^\circ$  and keeps a similar value. Different from Case 1, the change of ETAL with different flow directions in Case 2 and 3 comes from both the total drag force of the eight cages and the force distribution among anchor lines. When the drag forces from the fish cages transfer to the mooring system, the forces are distributed according to the flow direction and the mooring configuration. Thus, the changes of ETAL with different flow directions in Case 2 and 3 are determined by the total drag force and the configuration of the mooring system.

## 4.6 Summary

Numerical simulations of the 4x2 multi-cage fish farm model are performed to identify the impacts of the wake effect. The wake effect is divided into three regions and implemented into FE solver with different combinations, *i.e.*, (i) without wake effects, (ii) with only cage-to-cage wake effect, and (iii) with all the wake effects. The results show the impacts of wake effects clearly in terms of drag force, cultivation volume, and tension in anchor lines. The following are the main results from this study:

- 1) With all the three wake effects, the drag force on a single cage reduces by 39%, 62%, and 76%, as the flow passes through one, two, and three cages, respectively, when the flow direction is  $0^\circ$  and velocity is 0.5 m/s.
- 2) With all the three wake effects, the cultivation volume of a single cage increases by 12%, 44%, and 79% as the flow passes through one, two, and three cages, respectively, when the flow direction is  $0^\circ$  and velocity is 0.5 m/s.
- 3) Without the two internal wake effects, *i.e.*, twine-to-twine wake effect and net-to-net wake effect, the drag force of a single fish cage is overestimated by 19%, and the cultivation volume of a fish cage can be underestimated by 26%.
- 4) The flow field disturbed by the presence of fish cages can influence the maximum tension in anchor lines. Regardless of flow directions, the maximum tension in anchor lines with all wake effects is reduced up to 35% compared to that without wake effects.

## Chapter 5\*

# Numerical study on the structural responses of fish farms under accidental failure condition

---

In this chapter, the responses of fish farm models, such as the tension in cable of mooring grid, drag force of net structure, and cultivation volume, are investigated associated with accidental failure. The numerical simulations are performed using two different fish farm models. One is the single-cage model, and the other is the 4x1 multi-cage model. The responses of the two models are discussed in two sections (Section 5.2 and Section 5.3). Each section comprises both results from the intact model and failure mode model. The focus of this chapter is placed on the distribution of tensions in cables. The drag force and cultivation volume of cages are briefly discussed since the failure of a cable does not affect the flow velocity of the current. In Section 5.2, the single-cage model is studied to identify the impact of a failure in the mooring grid with a simple configuration. The responses of the model are computed, accounting for the wake effects within a cage. In Section 5.3, the 4x1 multi-cage is investigated to understand the responses of a functional fish farm. The wake effects for the inside and outside of a cage are accounted. Both models indicate that the failure in a cable might induce a significant increase in tensions of a cable.

---

\*The contents of this chapter are included in the paper which will be submitted to Aquacultural Engineering for possible publication.

## 5.1 Environmental loading

The environmental condition is considered to be a pure current condition with uniform velocity along with the depth. The current velocity is set to 0.5 m/s. Ten flow directions are used for simulations from  $0^\circ$  to  $90^\circ$  with an interval of  $10^\circ$ . The time-domain simulations are performed for both single-cage and 4x1 multi-cage model with 500 seconds as the simulation matrix, given in Table 5-1. As shown in Fig. 5-1, the cultivation volume of a fish cage for two numerical models converges to a single value approximately after 300 seconds. Therefore, the results used for the discussion of this chapter are taken as average value after 300 seconds.

Table 5-1: Simulation matrix.

	Mode	Flow direction	Flow velocity
<b>Single-cage</b>	intact	$0^\circ$ to $90^\circ$	0.5 m/s
	failure	$0^\circ$ to $90^\circ$	0.5 m/s
<b>4x1 multi-cage</b>	intact	$0^\circ$ to $90^\circ$	0.5 m/s
	failure	$0^\circ$ to $90^\circ$	0.5 m/s

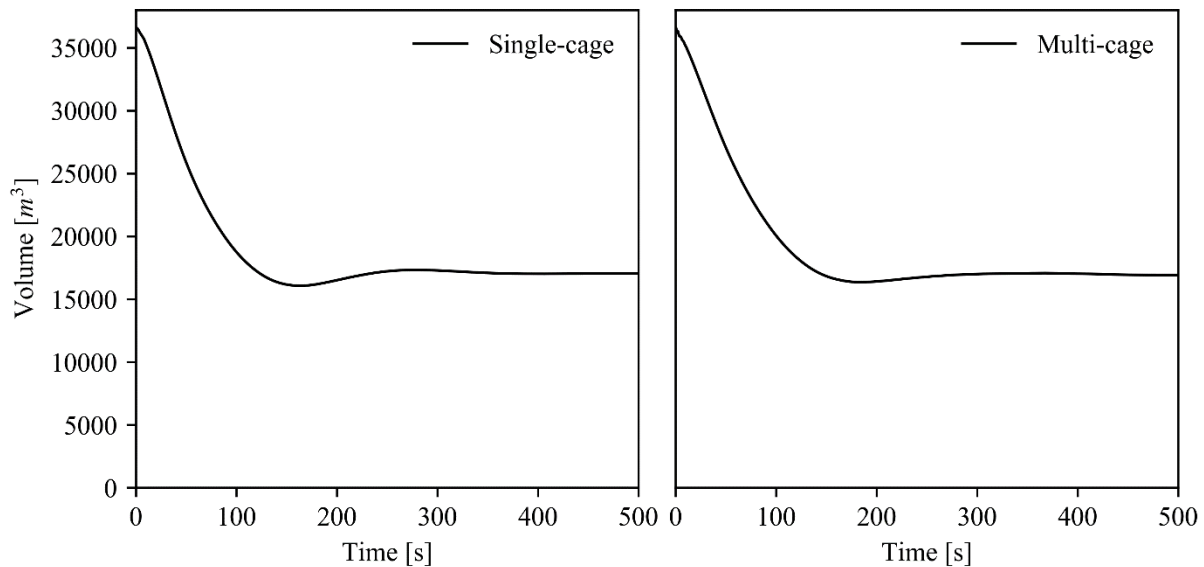


Fig. 5-1: Time history of estimated cage volume. Cage 1 with an incoming flow velocity of 0.5 m/s and  $0^\circ$  flow direction.

## 5.2 Single-cage model

### 5.2.1 Model set-up

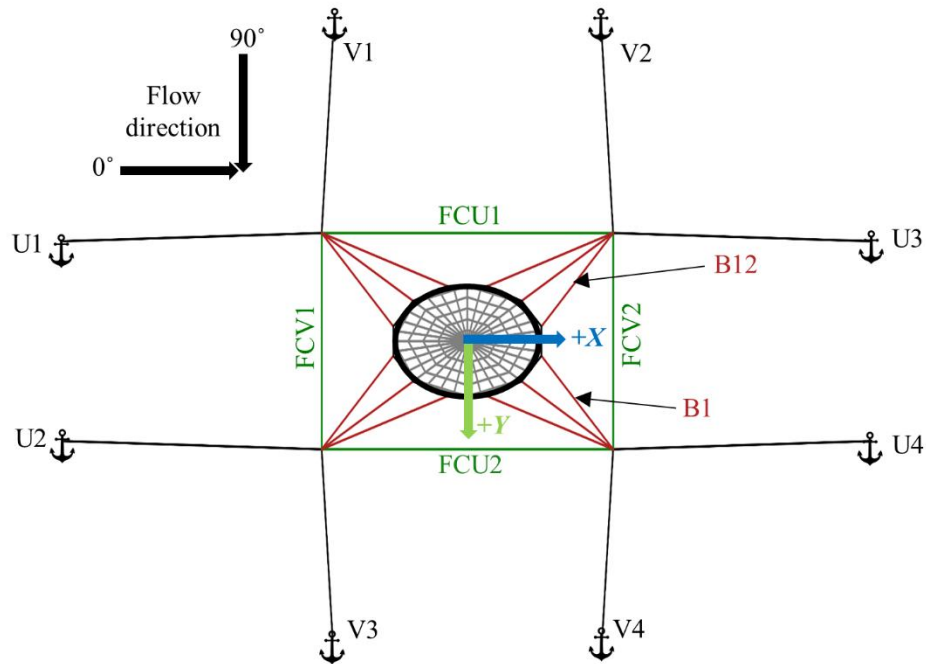


Fig. 5-2: Plan view of the single-cage model.

The single-cage fish farm is modeled, as shown in Fig. 5-2. The same fish cell in Chapter 4 is used for the numerical model (see Table 4-1 for dimensions and properties). The notations for the cables are as follows; U represents the mooring line in the  $x$ -direction, V is the mooring line in the  $y$ -direction, FCU is the frame cable in the  $x$ -direction, FCV is the frame cable in the  $y$ -direction, and B denotes the bridle. The bridles are numbered in clockwise order from the lower right corner of the cage to the upper right corner (from B1 to B12). The coordinates system is represented by the blue and green arrows, representing  $+x$  and  $+y$ -directions, respectively.  $+z$ -direction is facing into the paper. The black arrows on the upper left corner of the figure represent the direction of flow.

## 5.2.2 Tensions in mooring lines and frame cables

The tensions in cables of the mooring grid are the reactionary forces against the external forces such as hydrodynamic forces, gravitational force, and the forces transmitted from the other sub-models. The most significant contribution to the sum of external forces comes from the drag force of the net structure, which is in the direction of flow. Thus, one could say that the distribution of the tension among cables is highly dependent on the mooring grid configuration and the flow direction. In this section, the tensions in cables of the intact model and the failure model are studied over different flow directions to see the trend of the tensions in the cables. In addition, the most loaded cable is identified. The failure condition is defined later in this section, where the results of failure mode are discussed. Furthermore, the loads obtained from two modes (intact and failure) are compared to reveal the severity of the failure.

### Intact model

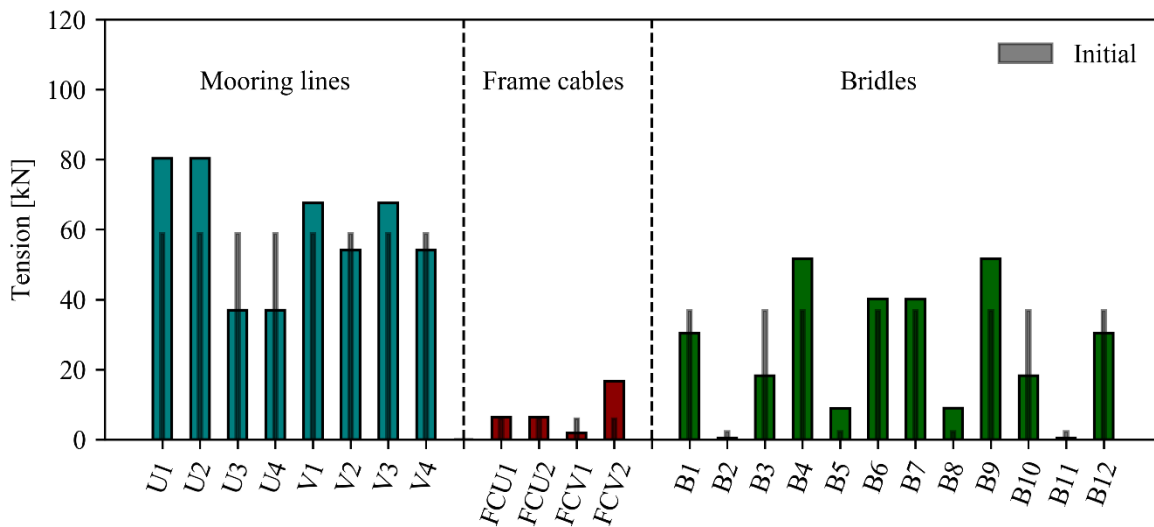


Fig. 5-3: Distribution of tensions in cables of the intact single-cage model (flow direction =  $0^\circ$ ). The thin grey bar represents the initial tension without any environmental loads, which is also called pre-tension.



Fig. 5-3 shows the tensions in each cable of the single-cage model, both initial condition and loaded condition with the current velocity of 0.5 m/s when the flow direction is  $0^\circ$ . The initial condition represents the pre-tension of the fish farm structure without any environmental loads. When the current load is imposed on the fish farm model, the maximum tension in a single cable occurs at upstream mooring lines (U1, U2 for  $0^\circ$  and V1, V2 for  $90^\circ$ ). The maximum tensions in U mooring lines and V mooring lines are having an identical value of 80.3 kN due to the symmetric geometry of the single-cage model (see Table B-4 in Appendix B).

By comparison of tension between the initial and loaded cases from Fig. 5-3, the reason for the change in tension may be explained. The components of fish farm structure such as buoys, floating collar, cables under loading are subjected to dislocate from its original location since the mooring lines and the frame cables are elastic bars, which deforms according to their elastic properties. In this perspective, the decrease of tension in U3 and U4 from their initial tension can be accounted. The elongations of U1 and U2 allow ends of U3 and U4 to dislocate from their initial positions, resulting in the release of elastic energy stored in U3 and U4 (see Fig. 5-3). The tensions in frame cables can be explained in the same manner as U3 and U4 by observing their changes in lengths (see Table 5-2). The results show that FCV1 experiences the lowest tension, and FCV2 experiences the largest tension among frame cables. The increment of tensions in the mooring lines U1, U2, V1, and V3 allows them to stretch out, letting the length of FCV1 to be shortened. Thus, the tension in FCV1 decreases to 1.8 kN from 6 kN of initial tension. On the contrary, FCV2 is elongated by 0.6 m from its initial length due to the change in lengths of V2 and V4.

Table 5-2: Change of length and strains of mooring lines and frame cables (flow velocity = 0.5 m/s, flow direction =  $0^\circ$ ).

	<b>U1</b>	<b>U2</b>	<b>U3</b>	<b>U4</b>	<b>V1</b>	<b>V2</b>	<b>V3</b>	<b>V4</b>	<b>FCV1</b>	<b>FCV2</b>
<b>Change[m]</b>	+1.3	+1.3	-1.0	-1.0	+0.4	-0.2	+0.4	-0.2	-1.0	+0.6
<b>Strain</b>	0.011	0.011	-0.008	-0.008	0.003	-0.002	0.003	-0.002	-0.01	0.0059

The frame cables can be considered as subsidiary cables to the mooring lines since the responses of the frame cables substantially change according to the loading condition of mooring lines. In addition, the bridles attached to the floating collar experience the tension according to the movement of the floating collar. Therefore, the tension in the bridle is highly correlated to the drag force of the net structure. The upstream bridles B4-9 are increased in tension, and downstream bridles B1-3 and B 10- 12 are decreased in tension when the flow direction is  $0^\circ$ , as shown in Fig. 5-3 (see Table B-3 and Table B-6 in Appendix B).

A single cable tension, which is the maximum at a given flow condition, is referred to as an extreme load in this chapter. The extreme load occurs at U1 from the flow direction of  $0^\circ$  to  $45^\circ$ . The magnitude of the extreme load in U1 becomes smaller as the flow direction increases. Once the flow direction is larger than  $45^\circ$ , V1 holds the extreme load until  $90^\circ$ . The extreme loads in U1 and V1 are symmetric about  $45^\circ$  due to the geometry of the single-cage model, as shown in Fig. 5-4. (Table B-4 in Appendix B).

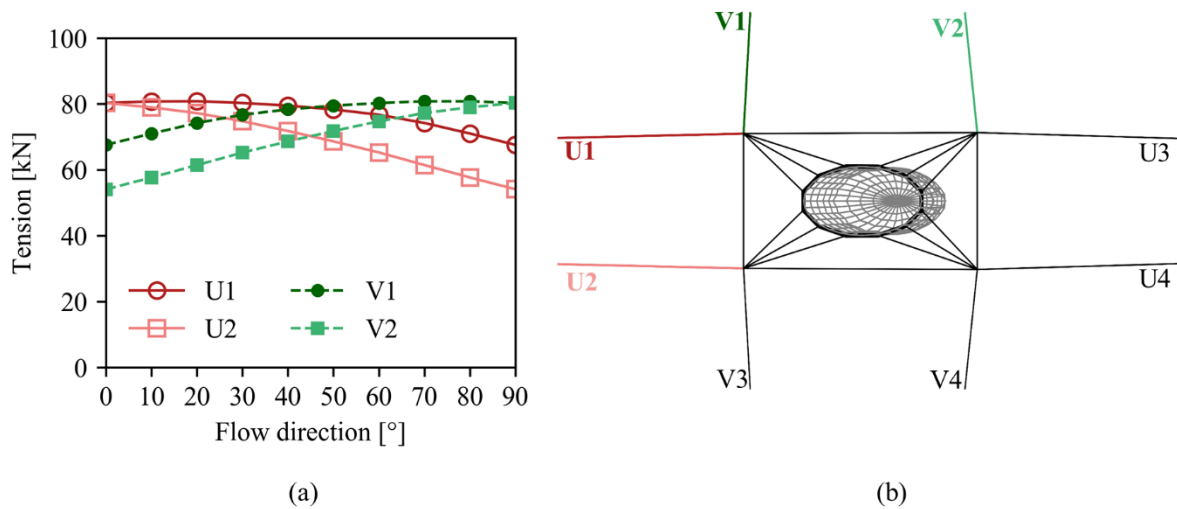


Fig. 5-4: Upstream mooring line tension for the intact single-cage model. (a) Tensions of upstream mooring lines of the intact single-cage model over different flow directions. (b) The single-cage model under the current load. The upstream mooring lines are highlighted in the right figure with the same color that appears in (a).

## Failure modes

All the tensions in mooring lines, frame cables, and bridles are investigated in a number of failure cases to identify which failure results in the most significant change in the responses of the structure. The failure mode is considered to fail one of the cables among frame cables and mooring lines. Furthermore, the numerical simulations are performed for different flow directions from  $0^\circ$  to  $90^\circ$  with an interval of  $10^\circ$ . Therefore, the tensions of all cables are studied through 120 different cases. Among all the failure mode cases, U1, U2, V1, and V2 mooring lines are identified as the most loaded cables when one of the neighboring mooring lines in the same direction fails to hold the load (*e.g.*, max. load in U1 when U2 fails). In other words, the maximum tension in all 120 cases occurs when one of U1, U2, V1, and V2 fails. Therefore, U1, U2, V1, and V2 are referred to as the critical cables for the single-cage model in this study. The maximum tensions in U and V mooring lines occur when the flow directions are  $0^\circ$  and  $90^\circ$ , respectively. The values of the maximum tensions in U1, U2, V1, and V2 are identical due to symmetric geometry and the absence of an upstream structure to alter the flow. The maximum tension of 106 kN in the critical cable is increased by 25.2 kN compared to the maximum tension of the intact model. The discrepancy of maximum tension between the intact model and the failure mode model shows a similar value compared to the previous research [24].

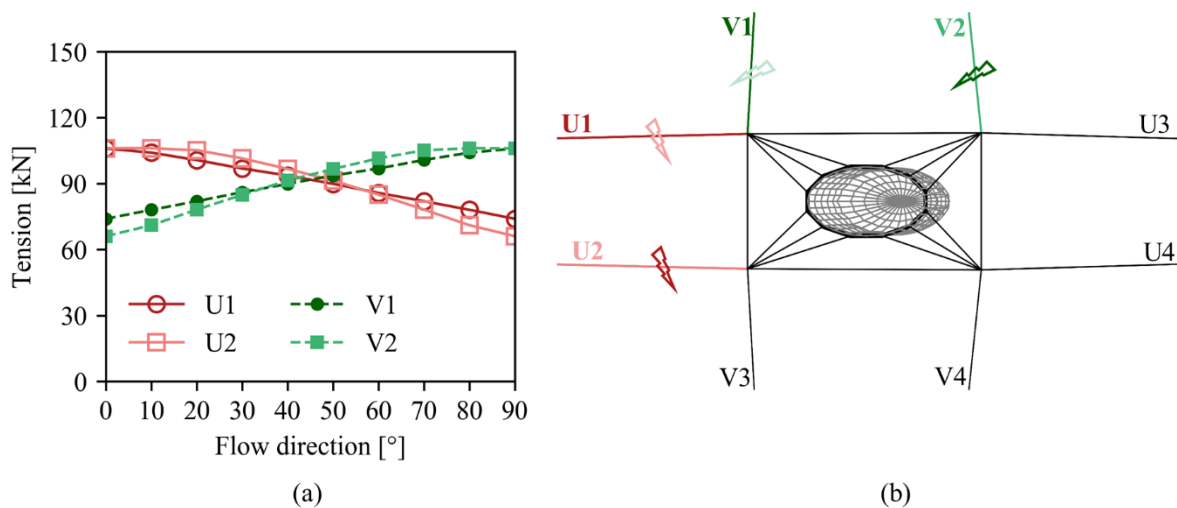


Fig. 5-5: Critical cable tension in case of failure. (a) shows the critical cable tensions. The failure mode considered for each critical cable tension is the case when the neighboring critical cable in the same direction fails. (b) Illustration of a failure condition for each critical cable. The position of a thunderbolt figure shows the which cable is considered to fail and the color of the thunderbolt represents the cable considered to plot the tension in (a).

The cable, which experiences the extreme load, however, is not the same as the intact model. As shown in Fig. 5-5, U2 holds the extreme load from flow direction  $0^\circ$  to  $45^\circ$ , and V2 holds the extreme load from  $45^\circ$  to  $90^\circ$ . This difference may account for the failure of critical cable, which originally holds the extreme load in the intact model.

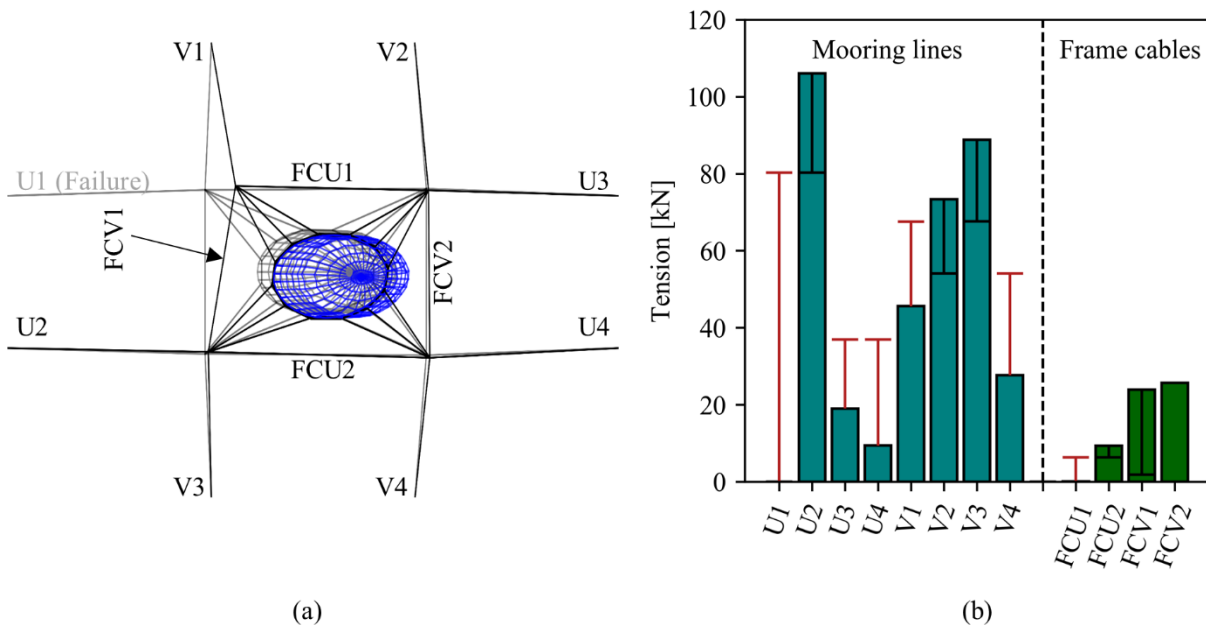


Fig. 5-6: Tension distribution and the location of the structure when U1 fails. (a) The position of the single-cage model when U1 fails in the  $0^\circ$  flow direction. The grey line represents the intact model, the black lines represent the mooring grid when U1 fails in the same flow condition, and the blue lines represent the position of net structure in failure condition. (b) Tension distribution among mooring lines and frame cables when U1 fails with the flow direction of  $0^\circ$ . The solid red lines on the histogram represent the decrease in tension compared to the intact model, and the solid black lines on the histogram represent the increase in tension compared to the intact model.

Fig. 5-6 shows one example of dislocation of structure when U1 fails under the current load in the flow direction of  $0^\circ$ . When a failure happens in one of the cables, the load taken by the failed cable is transferred to the other cables. Moreover, the constraint of the location of the relevant structure provided by the failed cable fails, resulting in a severe dislocation from its original position. As U1 fails, U2 increases by 25.8 kN in tension compared to the U2 tension of the intact model, and it holds the largest tension among all cables, letting the elongation of U2 of the failure mode model larger than the elongation of U2 of the intact model. Due to the increment of elongation, the fish farm structure shifts in the direction of flow more than the intact model. It results in the reduction of tension in the downstream mooring lines U3 and U4. In addition, the buoy connected to the mooring line U1 shifts in the direction of flow due to the loss of its constraint. Therefore, FCV1 experiences a significant increase in tension since the frame cable FCV1, which is originally subsidiary to the mooring lines, takes the part of mooring line tension. As expected, the mooring lines U3 and U4 decrease by 18 kN and 28 kN in tension, respectively. The frame cable FCV1 increases by 22 kN in tension from the intact model FCV1 tension of 1.8 kN.

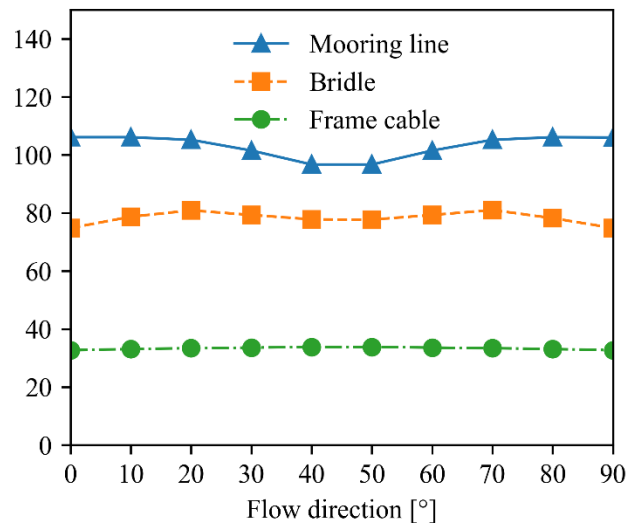


Fig. 5-7: Maximum tensions of the mooring line, bridle, and frame cable. Each triangular mark represents the maximum tension among mooring lines in 12 failure modes for a given flow direction, the square marks are for bridles, and the circular marks represent the frame cables.

The increments of tensions for the bridles and frame cables due to failure are not smaller than the increment of tension in the mooring line. The largest increment of frame cable tension compared to the intact model occurs at FCU1 when V1 fails with the flow direction of 20° (the same increase in tension occurs at FCV1 when U1 fails with the flow direction of 70° due to symmetry). The largest increment for bridle tension occurs at B4 when V1 fails with the flow direction of 40° (the same increase of tension occurs at B12 when U1 fails with the flow direction of 50°). The tensions in a frame cable and bridle are increased by 28.1 kN and 31.6 kN, respectively, while the most significant increase in tension for the mooring line is 28.0 kN. The most significant increase in tension for the mooring line occurs at U2 when U1 fails with the flow direction of 20° (the same increase in tension occurs at V2 when V1 fails with the flow direction of 70°). However, the largest tensions in a frame cable and bridle among all failure mode cases, are 34 kN and 81 kN, respectively. Both of the values are similar to or less than the maximum mooring line tension of the intact model. Therefore, the largest tension in the mooring line for each flow direction is always higher than that of bridle and frame cable, as appears in Fig. 5-7.

### 5.2.3 Drag force and cultivation volume

The drag force and the cultivation volume of the net structure of the fish cage are highly correlated since the hydrodynamic forces induced by the current is the major component to displace the nodes of the net elements. When the single-cage model is exposed to the flow condition with a flow velocity of 0.5 m/s, the results from the numerical simulation show that the cultivation volume decreases by 53.4% of the initial volume. The deformed state of the net structure due to drag force is shown in Fig. 5-8.

In the case of the single-cage model, there is no significant change in terms of drag force and cultivation volume due to the failure of one of the cables. The results from the numerical simulations show the changes are less than 5% among all simulation cases. The shape of the net structure underwater remains almost similar to the intact model since the major contribution to the deformation of the net structure comes from the incoming flow velocity, and the ambient flow velocity is always kept constant regardless of the failure. In addition, the single-cage model does not have the upstream cage, which alters the incoming flow field. Consequently, the net structures of both intact and failure mode models experience the same incoming flow velocity.

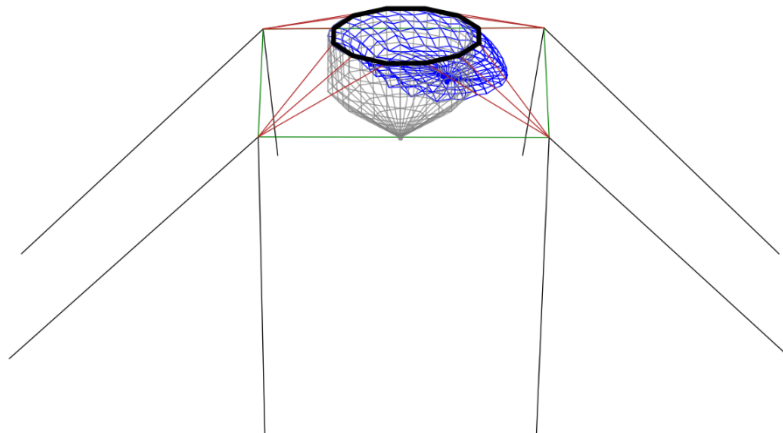


Fig. 5-8: Deformed state of the net structure of the single-cage model when exposed to the current load with the flow velocity of 0.5 m/s. the grey lines show the initial state of the net structure, and the blue line is the deformed state under the current load.

## 5.3 4x1 multi-cage model

### 5.3.1 Model set-up

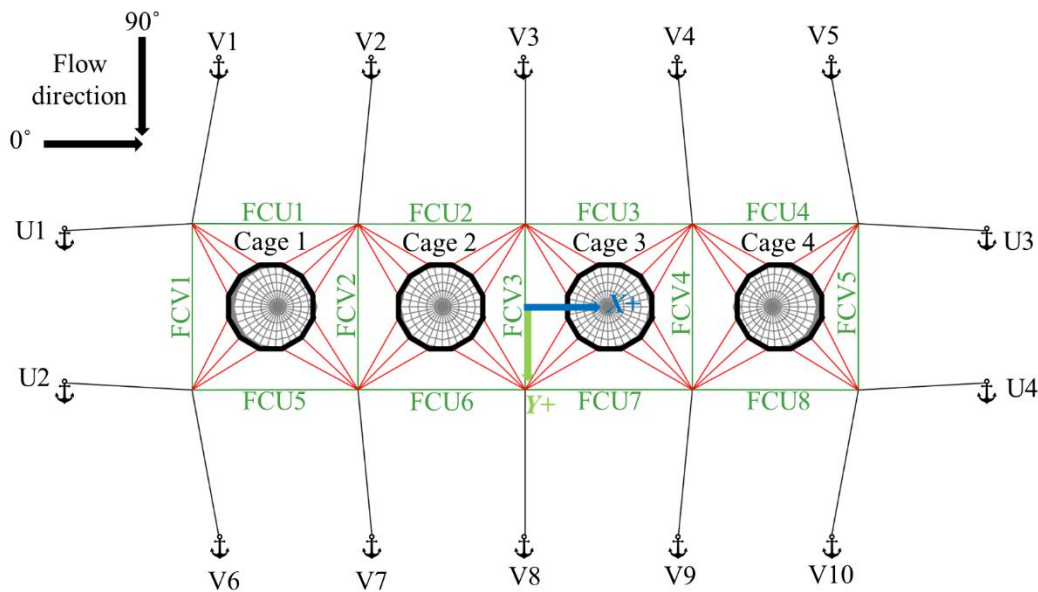


Fig. 5-9: Planview of 4x1 multi-cage fish farm model. The black arrows at the left corner of the figure represent the current direction. Blue and green arrows at the center of the fish farm grid represent the +x and +y-directions. +z-direction is facing into the paper.

The same fish cell as the single-cage model is used to form a 4x1 multi-cage model (see Table 4-1 for dimensions and properties). Fig. 5-9 shows the configuration of the 4x1 multi-cage fish farm. U and FCU denote the mooring line and frame cable in the  $x$ -direction. V and FCV denote the mooring line and frame cable in the  $y$ -direction. The bridles of each cage are denoted from B1 from B12 in the same manner as the single-cage model. The origin of the coordinate system is located at the center of the fish farm grid.

In the multi-cage configuration, the interaction between cages becomes vital since the presence of the upstream cage can change the incoming flow velocity for the downstream cage(s). The interaction between the cages is maximized when the flow direction is  $0^\circ$ . As explained in Section 3.3.3, the wake region after a cage is realized with a width of  $2D$ . Furthermore, the velocity reduction zone within the wake region is  $1.3D$  in the numerical model. Therefore, the reduction in velocity downstream will vanish once the flow direction is greater than  $35.1^\circ$ , and all the cages will experience the same incoming flow velocity when the flow direction is greater than  $48.6^\circ$  (see Fig. 5-11, Fig. 5-12, and Fig. 5-13). The sum of the drag forces exerted four cages is the largest when the flow direction is  $30^\circ$  since the downstream cages are only influenced by the flanks of the wake region where the flow velocity is slightly increased. The smallest total drag force of all four cages, as expected, is found when the flow direction is  $0^\circ$ .

The tensions in each cable vary as the flow direction changes according to its configuration. A cable aligned in  $x$ -direction decreases in tension as the flow direction increases from  $0^\circ$  to  $90^\circ$ , and for a cable aligned in  $y$ -direction increases in tension as the flow direction increases. Moreover, the magnitude of the tension in a single cable is dependent on the sum of the forces exerted on the entire fish farm structure since the tensions in the cables are the distributed reactionary forces. Thus, the tension in each cable should be examined considering both the sum of drag forces and its configuration according to the flow direction. The extreme tension occurs upstream mooring lines, as shown in Fig. 5-10. U1 holds the extreme load from  $0^\circ$  to  $40^\circ$ , and V2 holds the extreme load from  $50^\circ$  to  $90^\circ$  (see Table C-1 in Appendix C).

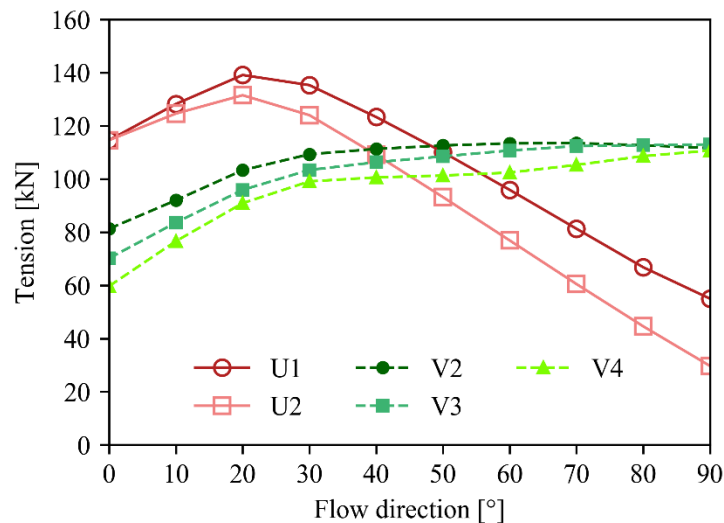


Fig. 5-10: Extreme loads for intact 4x1 multi-cage model.



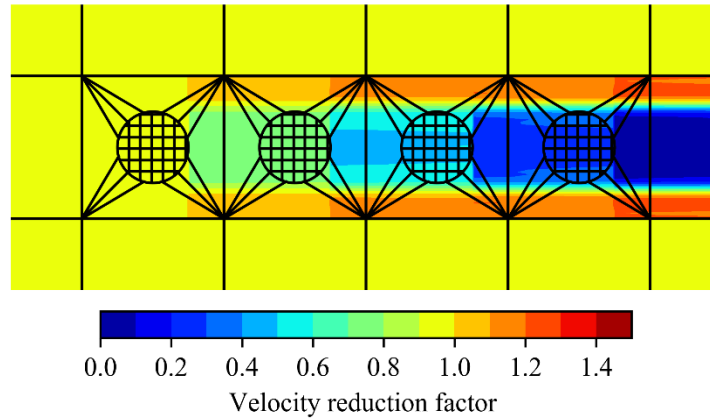


Fig. 5-11: Velocity contour associated with the velocity reduction after a permeable net structure. This figure represents the velocity reduction after one or several cages when the flow direction is  $0^\circ$ . The flow velocity after three cages is severely reduced.

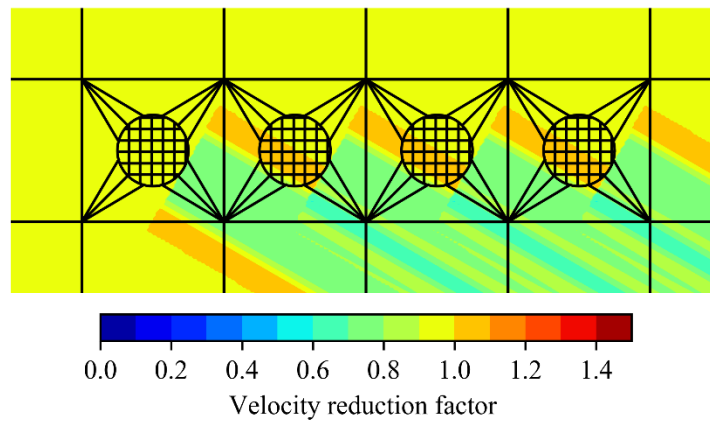


Fig. 5-12: Velocity contour when the flow direction is  $30^\circ$ . The downstream cages Cage 2, 3, and 4 are influenced by the flank of the wake region (red color) in which the flow velocity is slightly increased.

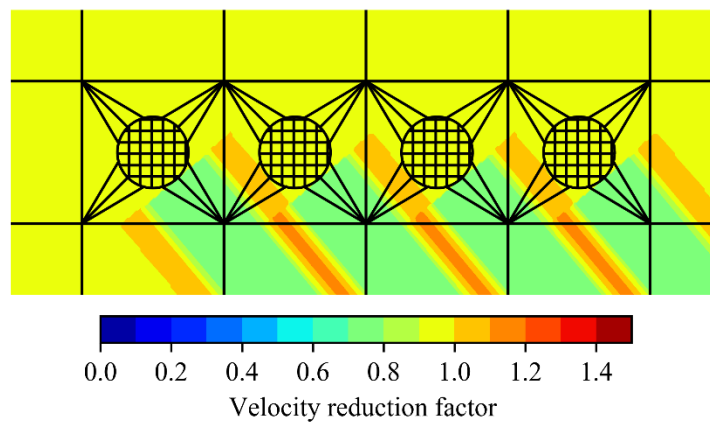


Fig. 5-13: Velocity contour when the flow direction is  $50^\circ$ . All the cages are not influenced by one another. Therefore, the incoming flow velocity for every cage is identical.

### 5.3.2 Tensions in mooring lines and frame cables

Intact model

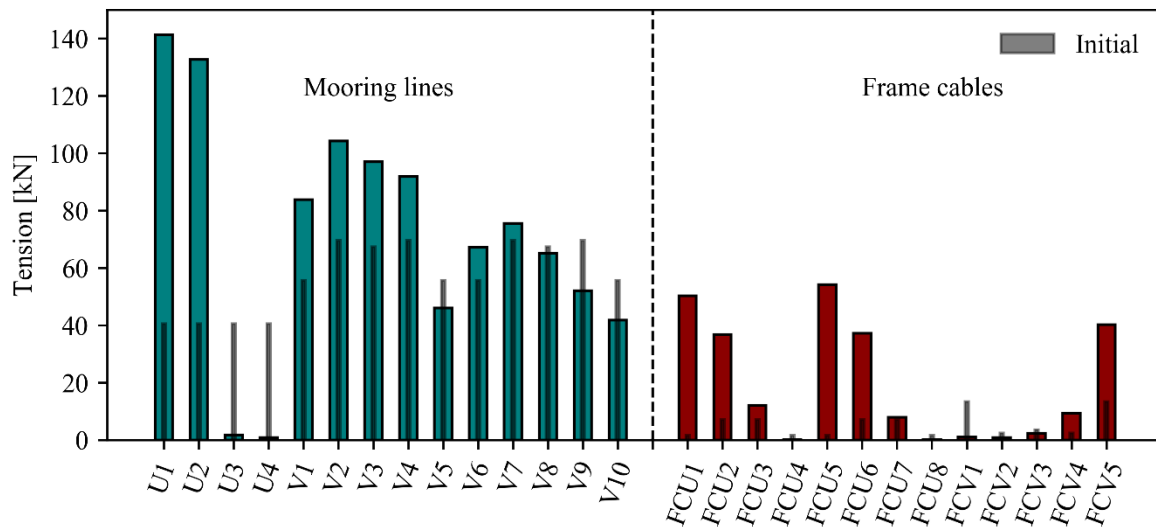


Fig. 5-14: Distribution of tension among mooring lines and frame cables when the flow direction is 20°. The grey bars represent the initial tensions.

Fig. 5-14 shows the tension distribution among mooring lines and frame cables in the 4x1 multi-cage model when the flow direction 20°. Unlike the single-cage model, the maximum tension among mooring lines does not occur when the flow direction is 0° due to the cage-to-cage wake effect. As expected, when the flow direction is 0°, the sum of all drag forces of four cages is the smallest among all flow directions. The results from the numerical simulations show that the maximum tension of 139.1 kN in a cable occurs at U1 when the flow direction is 20°, while the sum of drag forces of all cages is the largest when the flow direction is 30°. This may account for the contribution of V mooring lines is greater than the increment of the sum of drag forces when the flow direction is 30°. The most significant tensions exerted on bridle and frame cable are 57.7 kN and 53.5 kN, respectively, and both of them occur when the flow direction is 20° (see Section C.1 in Appendix C). In addition, the comparison between initial tension and the loading condition shows a great amount of change for U mooring lines, implying a significant change in lengths of the cables.

The mooring line tension is associated with the length of the mooring line according to the axial stiffness of the cable. Furthermore, the mooring line tension influences the position of a buoy in addition to the bridle tension. Thus, one can say that the tension in the frame cable reflects the position of the attached buoys, which corresponds to the length of the frame cable (see Fig. 5-15). When the flow direction is  $20^\circ$ , the largest increase and decrease in tension among frame cables occur at FCU5 and FCV1 in which they are the longest and the shortest frame cables, respectively.

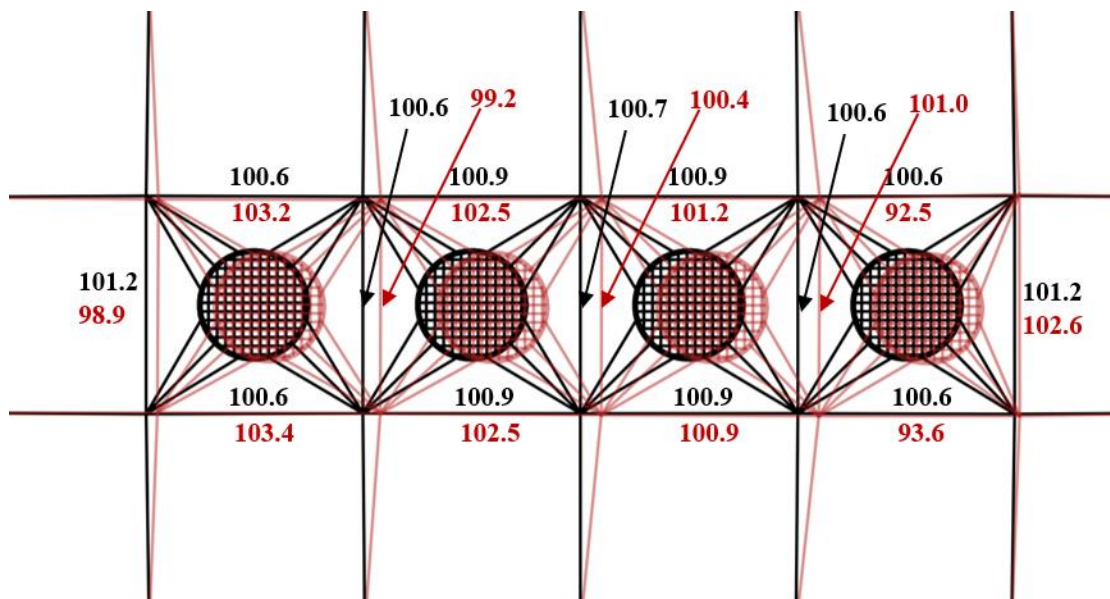


Fig. 5-15: The shifted position of the 4x1 multi-cage model (flow direction =  $20^\circ$ ). Black color represents the initial position, and the red color represents the shifted position. The number written in black represents the initial length of the adjacent cable, and the number written in red represents the length of the adjacent cable under the current load.

## Failure modes

In the numerical simulation of the 4x1 multi-cage model, the failure mode is considered in the same manner as the single-cage model. One of the cables among mooring lines and frame cables fails for each case. Twenty-seven failure modes for each flow direction are investigated thus, 270 cases in total. The tensions of mooring lines, frame cables, and bridles are investigated throughout the 270 cases to identify the maximum tension and significant changes in tension compared to the intact model.

Among all the cases, the most significant changes in tension for the mooring line, frame cable, and bridle are +80.0 kN, +39.1 kN, and +61.0 kN, respectively, compared to the intact model (see Section C.2 in Appendix C). The most significant change in tension of the mooring line occurs at U2 when U1 fails in the flow direction of 20° while the most significant changes in tension of frame cable and bridle occur at FCU7 and B12 of Cage 4, respectively, when V4 fails in the flow direction of 50°. When flow direction is 20°, the intact model shows the tension of 139.1 kN in U1, which is the largest tension in a single cable. Thus, it physically sounds to have the most significant increment in tension at U2 when U1 fails with the flow direction of 20°.

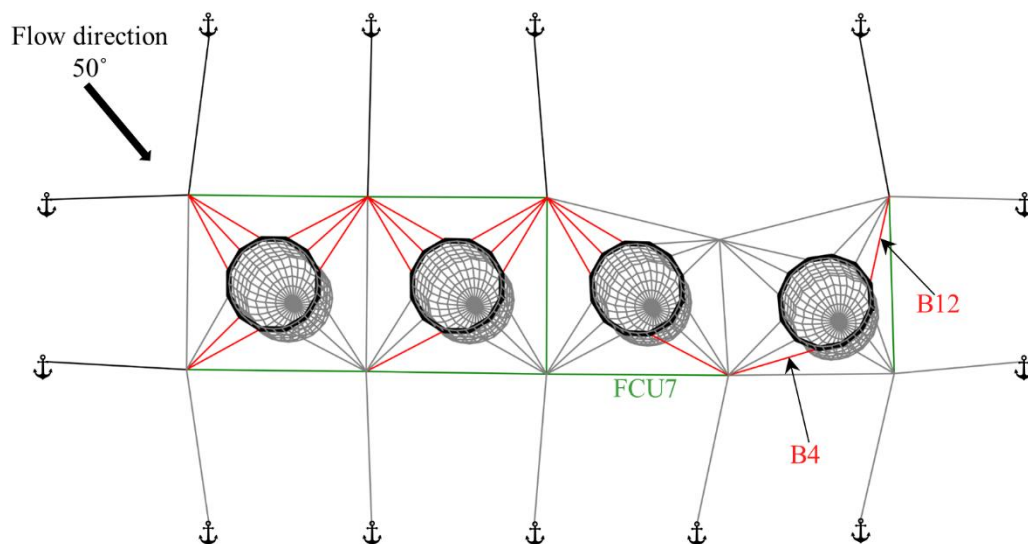


Fig. 5-16: Dislocation of the 1x4 multi-cage model when V4 fails. The cable experiences decreased tension compared to the pre-tension colored in grey.

For the frame cable, the tension in FCU7 of the intact model when the flow direction is 50° is 8.0 kN. Once V4 fails, the tension increases significantly up to 47.1 kN. This may account for the dislocation of the buoy, which attached to the V4. The loss of constraint of the buoy attached to V4 lets all the bridles of Cage 4 to shrink in length except B4

and B12. Thus, the only bridles to hold the Cage4 within the fish cell in this situation are B4 and B12 (see Fig. 5-16). It appears that FCU7 increases in tension since the increment of tension in B4 of Cage4 is transmitted to FCU7. In the same flow condition, the tension in B12 of Cage 4 of the intact model is 26.8 kN. The tension increases significantly up to 87.8 kN when V4 fails. The reason why B12 holds the larger tension than B4 might be accounted for the larger y-component drag force in the flow direction of 50°.

However, the cables which undergo the most significant change in tension do not experience the maximum tension among all cases. The maximum tensions in the mooring line, frame cable, and bridle occur at U1, FCU5, and B12 of Cage 4, respectively, among all 270 cases. The failure modes that cause the maximum tensions for mooring line, frame cable, and bridle are U2, U1, and V4, respectively. The flow direction for maximum mooring line and frame cable tension is 20° while the maximum tension in bridle occurs when the flow direction is 70°.

The maximum mooring line tension is the largest value among all cable tensions throughout the entire failure mode cases. On the other hand, the maximum frame cable tension and the maximum bridle tension are not the extreme load in the flow condition in question. Fig. 5-17 shows the largest tension in each upstream mooring line throughout entire failure modes with different flow directions. Since the largest tension in mooring line among all failure modes for a given flow condition is always greater than the that of frame cable and bridle, U1 holds the extreme load until the flow direction of 50° and V3 holds the extreme load when the flow direction is larger than 50° as appears in Fig. 5-17. The value of the largest tension in each upstream mooring line for a given flow condition and the failure mode that triggers the largest tension are presented in Table 5-3.

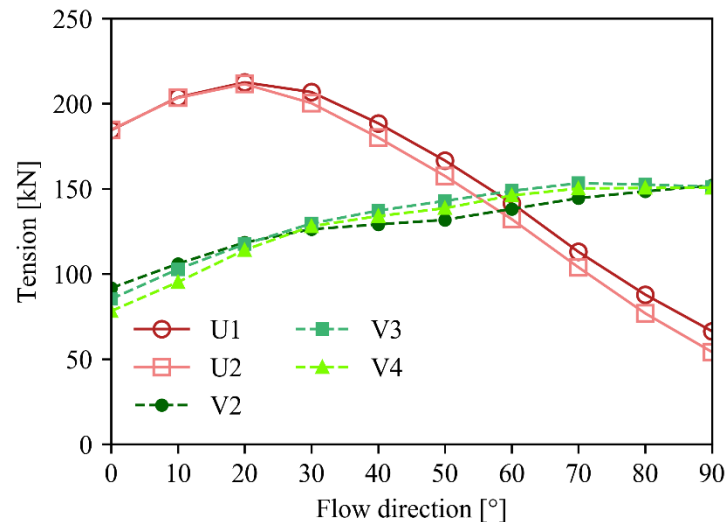


Fig. 5-17: The largest tension of each upstream mooring line among all failure modes for different flow directions.

Table 5-3: The largest tension in upstream mooring line and failure mode.

Flow direction [°]	U1 [kN]	Failure mode	U2 [kN]	Failure mode	V2 [kN]	Failure mode	V3 [kN]	Failure mode	V4 [kN]	Failure mode
0	184.4	U2	184.7	U1	100.9	U1	85.3	V2	78.2	V3
10	203.7	U2	203.4	U1	115.6	U1	102.8	V2	95.2	V3
20	212.5	U2	211.5	U1	128.5	U1	117.5	V2	114.1	V3
30	206.8	U2	200.3	U1	132.9	U1	129.6	V2	128.0	V3
40	188.5	U2	180.1	U1	134.1	V1	137.2	V2	134.0	V3
50	166.6	U2	157.5	U1	139.6	V1	142.9	V2	138.6	V3
60	141.6	U2	132.2	U1	144.3	V1	148.8	V2	146.1	V3
70	113.0	U2	103.9	U1	147.9	V1	153.3	V2	150.2	V3
80	87.9	U2	76.9	U1	148.5	V3	152.5	V2	150.5	V3
90	66.4	U2	54.2	U1	152.0	V3	151.2	V2	150.6	V3

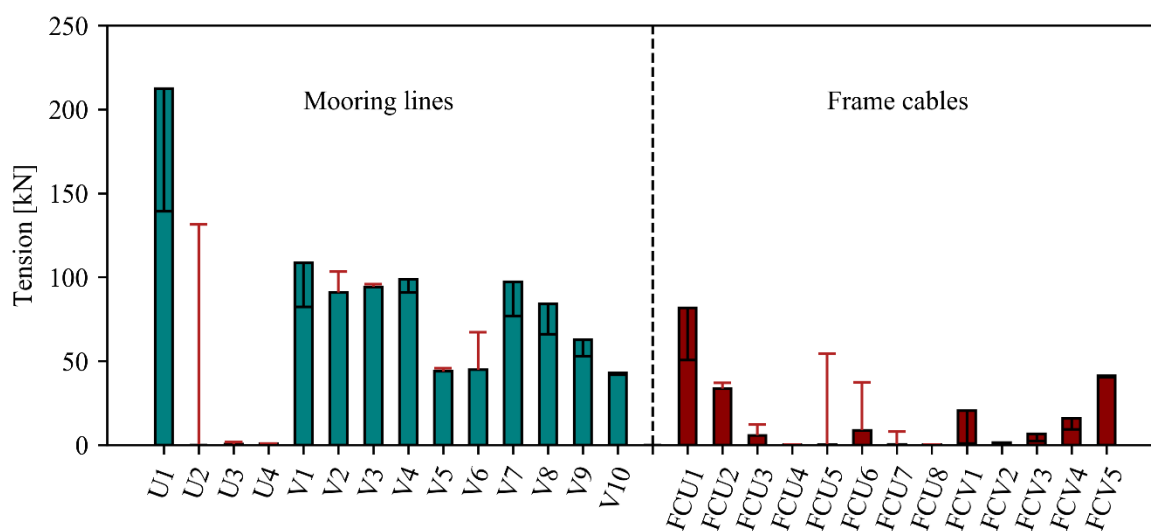


Fig. 5-18: Tension distribution among mooring lines and frame cables (U2 fails, flow direction = 20°). The black line inside of each histogram shows the increment of tension compared to the intact model, and the red lines represent the decrease in tension compared to the intact model.

The change in tension for all mooring lines and frame cables compared to the intact model is shown in Fig. 5-18. The flow condition and the failure mode considered for the figure is the case when the mooring line U1 holds the maximum tension among all cables throughout 270 cases. *i.e.*, U1 experiences the maximum tension of 212.5 kN when U2 fails with the flow direction of 20°, which is increased by 73.4 kN compared to the tension of U1 for the intact model with the same flow condition.

### 5.3.3 Drag force and cultivation volume

The drag force and the cultivation volume of a cage are highly correlated since the drag force, sinker tube, and center point weight are the main contributor for the determination of the net structure node position. In the numerical simulations of the multi-cage model, the drag force and the cultivation volume of a cage vary as the flow direction changes. As mentioned in 5.3.1, the velocity reduction on downstream cages vanishes when the flow direction is greater than  $35.1^\circ$ . Thus, the responses of all cages are similar to each other when the flow direction is greater than  $35.1^\circ$  (see Fig. 5-19). When flow direction is  $0^\circ$ , the reduction of incoming flow velocity for downstream cages is maximized. The drag force on Cage 4 reduces by 76.7% compared to Cage 1. The cultivation volume of Cage 4 increases by 84.8% compared to Cage 1.

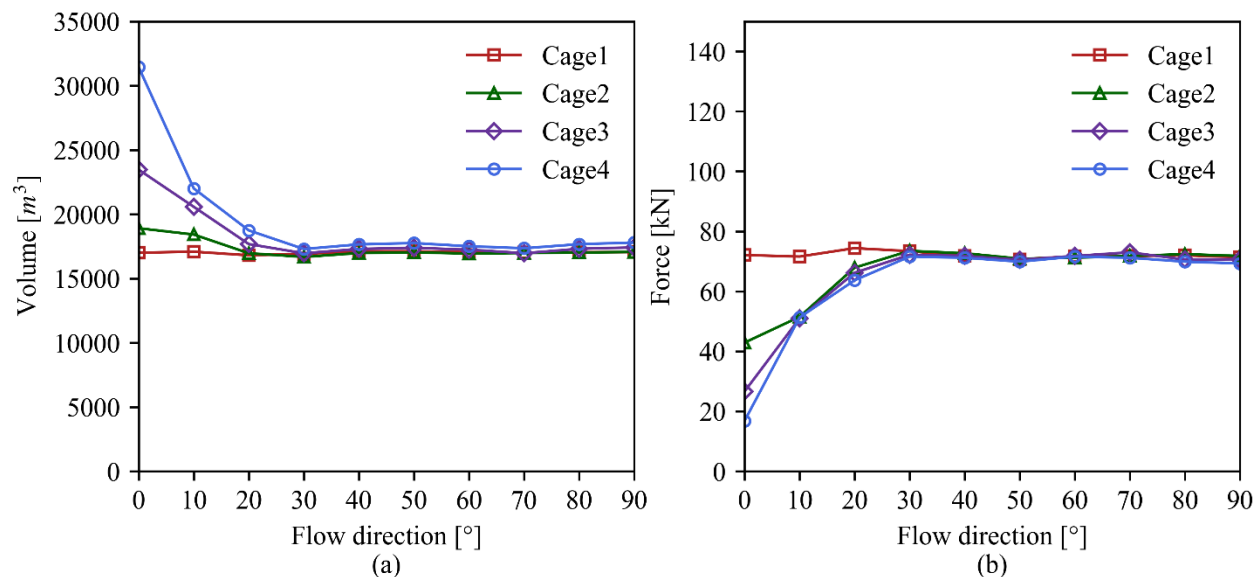


Fig. 5-19: Cultivation volume and drag force of all cages for the intact model. (a) Cultivation of volumes of all cages for all flow directions. (b) Drag force of all cages for all flow direction. The ambient flow velocity is 0.5 m/s for all cases.

For the cases where one cable fails among the mooring lines and frame cables, the results show similar responses to the intact model. The deviation from the intact model is less than 5% for all cases. The responses are highly dependent on the weights of the cage and the incoming flow velocity. Therefore, the drag force and cultivation volume appear to have similar values since the failure of a single cable does not alter the flow velocity nor the gravitational force of the cage weights.

---

## 5.4 Summary

Two fish farm models, namely single-cage and 4x1 multi-cage fish farms under uniform current, are investigated numerically. The responses such as tensions in cables, drag force of the net structures, and the cultivation volume are discussed associated with the failure modes. The focus is placed on the tensions in cables to identify the most loaded cables and the significant increase in tension due to failure.

The responses of the single-cage model present a symmetric trend about  $45^\circ$  due to its geometry. The largest increments in tensions for bridle and frame cable due to failure show a similar value compared to that for the mooring line. However, the mooring lines are found to hold extreme loads for all flow directions. Furthermore, the cables that undergo the largest increase in tension are not the same cables that experience the largest tensions in mooring lines, frame cables, and bridles. The cable which takes the maximum tension among all failure cases is identified and compared to the intact model.

The multi-cage model takes the flow disturbance by the upstream structures into account. Therefore, extreme loads show a different trend from the single-cage model. The flow direction in which the maximum tension occurs, are determined by the total drag force of four cages and contribution of  $x$  and  $y$ -direction mooring lines. The cables experiencing the most significant increase in tension and the cable that holds the maximum tension are identified through the results of the simulations. The main findings of this chapter are summarized as follows:

- 1) For the single-cage model, the increment of tensions induced by failure in the mooring line, frame cable, and bridle are up to 36%, 969%, and 69%, respectively. The increments are 28.0 kN, 28.1 kN, and 31.6. The percentile increase in tension for the frame cable has a much larger value than the others since the corresponding frame cable tension of the intact model is trivial (2.9 kN).
- 2) For the single-cage model, the maximum tension of 106.0 kN occurs at upstream mooring lines when one of the mooring grid cables fails. The maximum tension is increased by approximately 32.0 % compared to the maximum tension of the intact model.
- 3) For the 4x1 multi-cage model, the most significant increase in mooring line, frame cable, and bridle tensions due to failure are up to 61%, 488%, and 228%, respectively. The increments are 80.0 kN, 39.1 kN, and 61.0 kN. Although the percentile increase in tension suggests tremendous tension, the value of the tension under corresponding failure condition is not significant since the cable has a trivial tension before failure.
- 4) For the 4x1 multi-cage model, the results show that the maximum tension in a cable occurs at U1 when U2 fails with the flow direction of  $20^\circ$ . The maximum tension is increased by 52.8% compared to that of the intact model. The maximum tension is increased by 73.4 kN from 139.1 kN of the intact model to 212.5 kN of the failure mode model.



## Chapter 6

# Conclusions and future work

---

In this thesis, a numerical study on fish farm model using software, FhSim, is performed to estimate the load of the fish farm structure. Precise estimation of the load is essential to avoid the rupture of a cable and escape of fish. Therefore, the first study in Chapter 4 tackles the influence of the wake effect on the downstream structures, using a 4x2 multi-cage fish farm model. The flow field behind a permeable net structure is realized by implementing three wake effect implementation scheme, *i*) without wake effect, *ii*) with cage-to-cage wake effect, and *iii*) with all wake effects (twine-to-twine, net-to-net, cage-to-cage wake effects). The comparative study between results associated with each wake effect implementation scheme shows that the reduction of drag force is up to 76%, and the cultivation volume increases up to 79%. The results imply that the design of the fish farm structure might be conservative without considering the wake effect behind a net structure.

The second study in Chapter 5 deals with the accidental failure of a cable in the mooring grid how it influences the responses of the fish farm structure. By implementing a function to control the structural failure in a cable into a numerical software, the failure cases of the single-cage model and 4x1 multi-cage model are investigated. A comparison between the intact model and the failure mode model presents the cable, which would undergo the most significant change in tension. Furthermore, the maximum tension in a cable among all cases is found from the numerical simulations. The single-cage model and 4x1 multi-cage model differ in the flow direction where the maximum tension occurs due to interaction between cages and configuration of the mooring grid. The results show that the failure on one of the cables in the single-cage model and multi-cage model could increase the maximum tension by up to 31.4% and 52.8 %, respectively. The results may provide the guideline to determine the safety factor of the design load and the properties of the materials in the fish farm structure.

However, the environmental load is limited to the current load with uniform velocity in this thesis. The variation in flow velocity should be taken into account in analyzing the hydrodynamic loads of the structure. Furthermore, the wave excitation force should be included to examine the more realistic movement of the fish farm model, especially the floater of the cage. With more realistic environmental conditions implemented in numerical models, more accurate loads imposed on fish farm structure might be obtained. In addition, the fish inside of a cage should be accounted for the influence on the structural loads as they disturb the flow and hit the net structure.

The net-to-net wake effect implemented inside of a fish cage uses a velocity reduction factor that generates a uniform reduced velocity profile over the wake region. The expression for the velocity reduction factor, is based on the assumption that the flow is normal to the net panel, and the panel is considered as a rigid panel. However, the net panel is flexible, which is subject to deform. The deformation of a net panel changes the incoming flow direction, resulting in a non-uniform wake region behind. Therefore, a proper numerical method should be developed to account for the deformation of the net structure in the implementation of the net-to-net wake effect.

In addition, a physical model test should be conducted to obtain meaningful information about the physical effects. By doing so, the results from the numerical simulations can be justified.

# References

---

- [1] FAO, 2018. “The state of world fisheries and aquaculture 2018,” Meeting the sustainable development goals, Rome, Italy.
- [2] FAO, 2020. “The state of world fisheries and aquaculture 2020,” Sustainability in action, Rome, Italy.
- [3] Tacon, A. G. and Halwart, M., 2007. “Cage aquaculture: a global overview,” FAO Fisheries Technical Paper. No. 498, Rome, Italy.
- [4] Ernst & Young AS, 2019. “The Norwegian Aquaculture Analysis 2019,” Ernst & Yong AS, Accessed 10 June 2020, <https://www.ey.com/no>.
- [5] Bugrov, L. Y., 2006. “The SADC0 underwater fish-farming system,” Underwater Technology & Ocean World, Vol.1, p. 34-45.
- [6] Loverich, G. F. and Gace, L., 1998. “The effect of currents and waves on several classes of offshore sea cages,” Charting the future of ocean farming, p. 131-144.
- [7] Ryan, J., 2004. “Farming the deep blue,” Bord Iassaigh Mhara and Irish Marine Institue, Ireland.
- [8] AKVA group, 2020. “Cage farming aquaculture,” Exhibition catalogue, Accessed 5 June 2020, <https://www.akvagroup.com/download-catalogues>.
- [9] Scott, D. C. B. and Muir, J. F., 2000. “Offshore cage systems: A practical overview,” Option Mediterranennes-International Centre for Advanced Mediterranean Agronomic Studies, p. 79-89.
- [10] Keith, H. G. and James, D., 2020. “Offshore aquaculture project underway in Hawaii,” earthsky.org, posted 19 Oct 2011, Accessed 6 June 2020, <https://earthsky.org/human-world/offshore-aquaculture-project-underway-in-hawaii>.
- [11] RefaMed, 2020. “Fish farming technology for the open seas,” Exhibition catalogue, Accessed 15 June 2020, [https://refamed.com/gabbie\\_mare/tlc\\_system.html](https://refamed.com/gabbie_mare/tlc_system.html)
- [12] Nordlaks, 2020. “Havfarm,” Nordlaks, Accessed 15 June 2020, <https://www.nordlaks.no/havfarm>
- [13] Li, L., Jiang, Z., Høiland, A. V. and Ong, M. C., 2018. “Numerical analysis of a vessel shaped offshore fish farm,” Journal of Offshore Mechanics and Arctic Engineering, Vol. 140, 041201.
- [14] Løland, G., 1991. “Current forces on and flow through fish farms,” PhD thesis, NTNU, Trondheim, Norway.

- 
- [15] Bi, C. W. and Xu, T. J., 2018. "Numerical study on the flow field around a fish farm in tidal current," *Turkish Journal of Fisheries and Aquatic Sciences*, Vol. 18, p. 705-716.
- [16] Turner, A. A., Jeans, T. L. and Reid, G. K., 2016. "Experimental investigation of fish farm hydrodynamics on 1:15 scale model square aquaculture cages", *Journal of Offshore Mechanics and Arctic Engineering*, Vol. 138, 061201.
- [17] Gansel, L. C., McClimans, T. A. and Myrhaug, D., 2008. "The effects of fish cages on ambient currents," In *Proceedings of the ASME 27th International Conference on Offshore Mechanics and Arctic Engineering*, OMAE2008-57746.
- [18] Kristiansen, T. and Faltinsen, O. M., 2012. "Modelling of current loads on aquaculture net cages," *Journal of Fluids and Structures*, Vol. 34, p. 218-235.
- [19] Endresen, P. C., Føre, M., Fredheim, A., Kristiansen, D. and Enerhaug, B., 2013. "Numerical modeling of wake effect on aquaculture nets," In *Proceedings of the ASME 2013 32nd International Conference on Ocean, Offshore and Arctic Engineering*, OMAE2013-11446.
- [20] Blevins, R. D., 2001. "Flow-Induced Vibration," Krieger Publishing Company, Malabar, United States.
- [21] Moe-Føre, H., Endresen, P. C., Aarsæther, K. G., Jensen, J., Føre, M., Kristiansen, D., Fredheim, A., Lader, P. and Reite, K., 2015. "Structural Analysis of Aquaculture Nets: Comparison and Validation of Different Numerical Modeling Approaches," *Journal of Offshore Mechanics and Arctic Engineering*, Vol. 137, 041201.
- [22] Zhao, Y., Bi, C., Dong, G., Gui, F., Cui, Y. and Xu, T., 2013. "Numerical simulation of the flow field inside and around gravity cages," *Aquacultural Engineering*, Vol. 52, p. 1-13.
- [23] Tsarau, A. and Kristiansen, D., 2019. "Application of Fhsim for the analysis of environmental loads on a complete fish-farm system," In *VIII International Conference on Computational Methods in Marine Engineering*, p. 271-284.
- [24] Tang, H. J., Yang, R. Y. and Huang, C. C., 2019. "Numerical modelling of the mooring line failure induced performance changes of a marine fish cage in irregular waves and currents," In *Proceedings of the ASME 2019 38th International Conference on Ocean, Offshore and Arctic Engineering*, OMAE2019-95730.
- [25] Standards Norway, 2009. "NS9415: Marine fish farms: Requirements for design, dimensioning, production, installation and operation," Standards Norway, Oslo, Norway, Standard No. NS9415.
- [26] Çengel, Y. A. and Cimbala, J. M., 2010. "Fluid mechanics: Fundamentals and applications." McGraw-Hill Education, Singapore.
- [27] Morison, J. R., O'Brian, M. P., Johnson, J. W. and Schaaf, S. A., 1950. "The force exerted by surface waves on piles," *Journal of Petroleum Technology*, Vol. 2, pp. 149-154.
- [28] Zdravkovich, M. M., 1997. "Flow around circular cylinders Vol 1: Fundamentals," Oxford Science Publications, New York, United States.
- [29] Fredheim, A., 2005. "Current forces on net structures," PhD thesis, NTNU, Trondheim, Norway.
- [30] Sumer, B. M. and Fredsøe, J., 2006. "Hydrodynamics around cylindrical structures," World Scientific Publishing, Singapore.
-

- 
- [31] Schlichting, H., 1979. "Boundary-Layer Theory," Mcgraw-hill book company, New York, Unites States.
- [32] Reite, K. J., Føre, M., Aarsæther, K. G., Jensen, J., Rundtop, P., Kyllingstad, L.T., Endresen, P. E., Kristiansen, D., Johansen, V. and Fredheim, A., 2014. "FhSim – Time domain simulation of marine systems," In Proceedings of the ASME 2014 33rd International Conference on Ocean, Offshore and Arctic Engineering, OMAE2014-23165.
- [33] SINTEF Ocean, 2020. "FhSim – time domain simulation," FhSim, Accessed 10 June 2020, <https://fhsim.no/>
- [34] Cheng, H., Aarsæther, K. G., Li, L. and Ong, M. C., 2018. "Numerical study of a single-point mooring gravity fish cage with different deformation-suppression methods," Journal of Offshore Mechanics and Arctic Engineering, Vol. 142, 041301.
- [35] Huang, C. C., Tang, H. J. and Liu, J. Y., 2006. "Dynamical analysis of net cage structures for marine aquaculture: Numerical simulation and model testing," Aquacultural Engineering, Vol. 35, p. 258-270.
- [36] Endresen, P. C., Birkevold, J., Føre, M., Fredheim, A., Kristiansen, D. and Lader, P., 2014. "Simulation and validation of a numerical model of a full aquaculture net-cage system," In Proceedings of the ASME 2014 33rd International Conference on Ocean, Offshore and Arctic Engineering, OMAE2014-23382.
- [37] Priour, D., 1999. "Calculation of net shapes by the finite element method with triangular elements," Communications in Numerical Methods in Engineering, Vol. 15, p. 775-763.
- [38] Enerhaug, B., Føre, M., Endresen P. C., Madsen, N. and Hansen, K., 2012. "Current loads on net panels with rhombic meshes," In Proceedings of the ASME 2012 31st International Conference on Ocean, Offshore and Arctic Engineering, OMAE2012-83394.
- [39] Cheng, H., Li, L., Aarsæther, K. G. and Ong, M. C., 2020. "Typical hydrodynamics models for aquaculture nets: A comparative study under pure current conditions," Aquacultural Engineering, Vol.90, 102070.
- [40] Sim, J., Cheng, H., Aarsæther, K. G., Li, L. and Ong, M. C., 2020. "Numerical investigation on the cage-to-cage wake effect: A case study of a 4x2 cage array," In Proceedings of the ASME 2020 39th International Conference on Ocean, Offshore and Arctic Engineering, OMAE2020-18928.

## Appendix A

# Results of simulations for 4x2 multi-cage fish farm model

---

This appendix provides the results of the simulations performed for the 4x2 multi-cage fish farm model. The results are categorized based on three responses of the fish farm model, *i.e.*, drag force and cultivation volume of a fish cage, and mooring tension of fish farm model. The results presented in each category of this appendix correspond to the discussion in Chapter 4 associated with wake effect implementation scheme. For the convenience of the reader, the configuration of the 4x1 multi-cage system and the simulation matrix are presented on the next page.

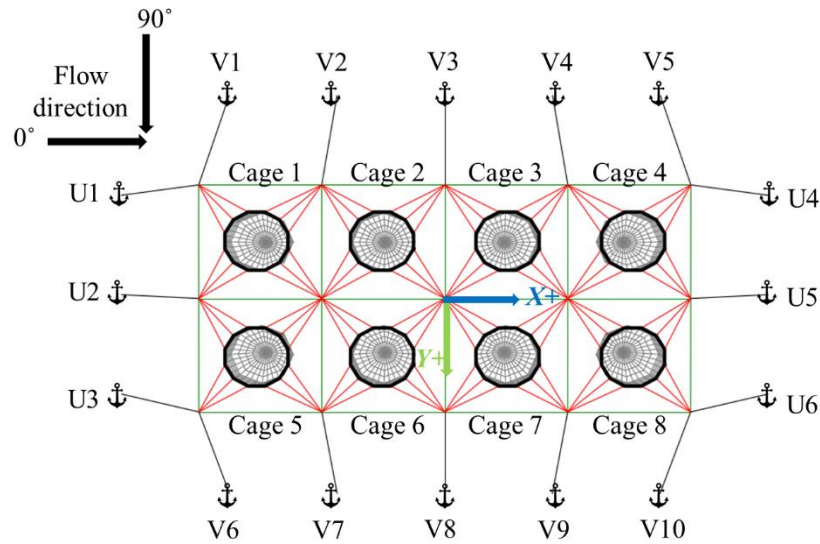


Fig. A-1: Configuration of 4x1 multi-cage model.

Table A-1: Simulation matrix for 4x1 multi-cage model.

	Wake effect selection	Flow direction	Flow velocity
Case 1	without wake effects	0° to 90°	0.5 m/s
Case 2	with only cage-to-cage wake effect	0° to 90°	0.5 m/s
Case 3	with all the three wake effects	0° to 90°	0.5 m/s

## A.1 Drag force of all cages with different flow directions and wake effects (Case 1, 2, and 3)

Table A-2: Total drag force for all cages for different flow directions (Case 1).

Flow direction [°]	Cage 1 [kN]	Cage 2 [kN]	Cage 3 [kN]	Cage 4 [kN]	Cage 5 [kN]	Cage 6 [kN]	Cage 7 [kN]	Cage 8 [kN]
0	91.8	92.9	91.2	90.9	92.6	92.3	90.5	91.4
10	90.4	91.0	90.5	90.1	92.0	90.5	93.0	90.6
20	88.9	90.9	90.2	90.8	91.2	90.8	91.9	90.4
30	90.8	89.0	90.3	90.9	91.6	90.2	92.2	90.4
40	90.0	90.3	89.3	89.5	90.8	90.8	90.6	91.2
50	88.2	89.9	89.9	91.1	90.9	92.9	92.3	90.5
60	89.7	88.7	90.8	91.6	89.2	89.8	90.5	89.6
70	90.2	89.9	89.9	91.4	90.3	89.5	91.4	93.5
80	91.4	89.9	91.4	91.2	90.1	90.7	92.7	91.1
90	91.8	90.8	92.3	90.6	92.5	92.0	91.2	91.3

Table A-3: Total drag force for all cages for different flow directions (Case 2).

<b>Flow direction</b> [°]	Cage 1 [kN]	Cage 2 [kN]	Cage 3 [kN]	Cage 4 [kN]	Cage 5 [kN]	Cage 6 [kN]	Cage 7 [kN]	Cage 8 [kN]
<b>0</b>	91.5	53.3	31.6	18.4	91.8	53.7	32.1	18.5
<b>10</b>	90.8	65.5	66.6	67.6	92.3	65.6	66.0	64.4
<b>20</b>	90.9	84.0	82.9	83.0	91.5	85.3	63.8	35.2
<b>30</b>	90.1	91.8	91.8	91.1	91.4	85.1	55.3	56.3
<b>40</b>	90.5	92.3	91.9	91.1	90.3	60.7	64.1	63.6
<b>50</b>	90.6	90.0	90.5	90.7	92.7	61.5	60.7	60.6
<b>60</b>	89.9	90.0	90.1	91.4	92.5	85.9	85.8	85.8
<b>70</b>	89.0	90.1	90.3	91.5	83.3	87.1	84.9	85.1
<b>80</b>	90.2	90.7	90.8	90.6	66.8	66.7	65.1	64.2
<b>90</b>	91.8	91.1	91.2	91.0	54.9	54.3	54.6	54.6

Table A-4: Total drag force for all cages for different flow directions (Case 3).

<b>Flow direction</b> [°]	Cage 1 [kN]	Cage 2 [kN]	Cage 3 [kN]	Cage 4 [kN]	Cage 5 [kN]	Cage 6 [kN]	Cage 7 [kN]	Cage 8 [kN]
<b>0</b>	72.4	44.0	27.3	17.4	72.5	44.9	27.0	17.0
<b>10</b>	71.1	52.3	52.6	53.9	71.8	52.4	52.8	52.0
<b>20</b>	72.2	66.9	66.2	66.1	74.3	69.6	53.8	31.3
<b>30</b>	72.4	73.1	72.4	72.7	73.9	68.8	45.7	47.0
<b>40</b>	71.1	72.2	72.7	72.4	71.5	50.3	52.5	52.6
<b>50</b>	70.9	71.3	71.0	71.4	72.9	51.5	50.7	50.4
<b>60</b>	71.1	71.9	72.4	73.0	73.2	68.7	68.4	68.5
<b>70</b>	71.0	71.7	72.2	72.8	65.5	70.1	68.7	69.0
<b>80</b>	71.4	71.5	71.6	71.9	54.2	54.3	53.6	52.8
<b>90</b>	71.9	72.2	71.9	72.7	45.5	45.5	45.4	45.8



## A.2 Volume of all cages with different flow directions and wake effects (Case 1, 2, and 3)

Table A-5: Cultivation volume of all cages for different flow directions (Case 1).

Flow direction [°]	Cage 1 [m <sup>3</sup> ]	Cage 2 [m <sup>3</sup> ]	Cage 3 [m <sup>3</sup> ]	Cage 4 [m <sup>3</sup> ]	Cage 5 [m <sup>3</sup> ]	Cage 6 [m <sup>3</sup> ]	Cage 7 [m <sup>3</sup> ]	Cage 8 [m <sup>3</sup> ]
0	13088.9	13083.3	13129.0	13138.0	13096.9	13076.0	13120.9	13123.3
10	13225.7	13214.8	13298.1	13279.5	13115.4	13122.6	13167.8	13212.7
20	13288.7	13267.0	13400.6	13348.3	13053.3	13045.8	13102.3	13229.5
30	13343.5	13301.4	13379.9	13380.3	13128.9	13128.2	13179.6	13225.9
40	13247.6	13191.9	13228.8	13259.5	13115.2	13074.8	13108.1	13127.0
50	13316.8	13262.1	13248.3	13223.7	13128.2	13110.2	13111.1	13101.3
60	13466.5	13381.8	13316.6	13182.1	13290.8	13268.1	13237.5	13130.2
70	13447.7	13338.7	13244.1	13133.6	13282.0	13225.8	13174.3	13050.8
80	13316.8	13267.4	13216.6	13156.7	13242.9	13202.8	13188.7	13120.4
90	13124.2	13128.9	13128.3	13127.1	13090.6	13077.8	13079.0	13091.5

Table A-6: Cultivation volume of all cages for different flow directions (Case 2).

Flow direction [°]	Cage 1 [m <sup>3</sup> ]	Cage 2 [m <sup>3</sup> ]	Cage 3 [m <sup>3</sup> ]	Cage 4 [m <sup>3</sup> ]	Cage 5 [m <sup>3</sup> ]	Cage 6 [m <sup>3</sup> ]	Cage 7 [m <sup>3</sup> ]	Cage 8 [m <sup>3</sup> ]
0	13135.0	15143.0	21349.8	29917.5	13131.3	16037.8	18411.8	27520.8
10	13242.4	14697.0	16214.7	16513.0	13150.9	14887.4	15678.9	16922.6
20	13279.8	13543.2	13844.2	13939.3	13066.4	13596.2	15226.1	23020.8
30	13338.9	13058.9	13090.4	13095.5	13140.6	13087.4	15813.6	17687.6
40	13236.4	13121.3	13139.4	13164.0	13122.2	15624.5	16388.4	17909.7
50	13289.7	13232.9	13226.0	13213.7	13089.9	16724.1	16846.6	17639.5
60	13462.2	13379.8	13318.2	13187.6	13115.7	13315.1	13324.0	13173.2
70	13438.2	13330.8	13239.1	13129.4	13681.4	13672.2	13639.1	14016.1
80	13310.1	13269.7	13227.8	13183.3	16128.4	16228.8	16417.0	17412.1
90	13130.1	13125.7	13132.4	13138.9	17676.1	17935.7	17820.6	19002.9

Table A-7: Cultivation volume of all cages for different flow directions (Case 3).

<b>Flow direction</b> [°]	Cage 1 [m <sup>3</sup> ]	Cage 2 [m <sup>3</sup> ]	Cage 3 [m <sup>3</sup> ]	Cage 4 [m <sup>3</sup> ]	Cage 5 [m <sup>3</sup> ]	Cage 6 [m <sup>3</sup> ]	Cage 7 [m <sup>3</sup> ]	Cage 8 [m <sup>3</sup> ]
<b>0</b>	17023.4	19026.0	24543.1	30478.9	17026.7	19809.5	22355.8	29148.9
<b>10</b>	17120.4	18625.3	20304.4	20563.6	17011.8	19023.8	19671.2	20959.2
<b>20</b>	17037.3	17207.0	17543.0	17579.5	16700.3	17193.3	18613.1	25557.5
<b>30</b>	16990.7	16783.6	16793.2	16757.7	16847.2	16718.3	19727.0	21437.7
<b>40</b>	17210.5	17052.7	17040.1	17034.5	17048.5	19440.6	20184.2	21685.4
<b>50</b>	17219.5	17153.0	17125.0	17113.6	17001.5	20506.0	20603.0	21316.5
<b>60</b>	17163.8	17041.0	16960.5	16844.6	16824.2	17027.6	17037.9	16890.9
<b>70</b>	17135.1	17049.8	16999.4	16888.9	17569.6	17308.6	17293.6	17741.7
<b>80</b>	17093.5	17058.8	17038.6	17007.0	20020.1	20204.6	20274.8	21319.4
<b>90</b>	17048.2	17050.2	17029.7	17017.6	21510.4	21528.9	21485.7	22787.1

### A.3 Mooring line tensions with different flow directions and wake effects (Case 1, 2, and 3)

Table A-8: Mooring line tension for different flow directions (Case 1).

Anchor [kN]	Flow direction [°]									
	0	10	20	30	40	50	60	70	80	90
<b>U1</b>	225.6	227.5	223.9	214.1	199.9	180.2	156.3	130.0	103.9	79.1
<b>U2</b>	274.5	270.0	259.3	241.5	218.9	190.3	158.3	127.9	96.8	62.7
<b>U3</b>	225.6	216.1	201.2	179.2	151.1	118.6	83.4	49.8	27.2	18.2
<b>U4</b>	0.1	0.1	0.2	0.5	1.4	6.7	14.5	30.4	53.1	79.1
<b>U5</b>	0.0	0.0	0.2	1.2	5.0	10.1	16.8	24.9	39.6	62.8
<b>U6</b>	0.1	0.1	0.2	0.4	0.5	0.6	0.7	1.7	9.0	18.2
<b>V1</b>	101.0	110.4	117.8	122.8	126.3	129.6	132.0	135.9	135.5	131.0
<b>V2</b>	114.2	130.0	143.7	154.4	164.8	174.7	181.5	187.5	189.6	189.2
<b>V3</b>	102.7	121.9	138.7	152.8	165.7	177.6	187.0	194.7	198.8	201.8
<b>V4</b>	86.5	107.5	125.9	141.6	156.5	165.9	172.6	179.0	183.4	189.2
<b>V5</b>	33.1	33.7	35.8	40.2	48.7	65.8	83.6	105.0	121.0	131.0
<b>V6</b>	100.9	89.0	75.6	60.7	29.5	28.0	13.0	5.3	0.1	0.1
<b>V7</b>	114.2	95.4	74.7	53.1	19.6	17.5	7.5	2.1	0.1	0.1
<b>V8</b>	102.7	80.7	57.3	35.4	12.4	11.3	5.9	2.3	0.1	0.0
<b>V9</b>	86.5	63.7	43.8	26.1	12.8	12.2	9.5	6.9	3.3	0.1
<b>V10</b>	33.1	32.0	28.4	23.9	9.6	8.6	1.3	0.2	0.1	0.1

Table A-9: Mooring line tension for different flow directions (Case 2).

Anchor [kN]	Flow direction [°]									
	0	10	20	30	40	50	60	70	80	90
<b>U1</b>	165.3	201.1	205.8	203.8	184.6	164.4	154.8	127.0	94.4	69.5
<b>U2</b>	208.0	241.3	239.9	231.1	204.1	176.5	157.5	124.2	84.3	51.7
<b>U3</b>	165.3	190.8	184.0	170.5	140.6	110.5	83.3	48.9	26.8	17.0
<b>U4</b>	0.1	0.1	0.3	0.5	2.1	7.4	14.5	30.9	49.9	70.0
<b>U5</b>	0.1	0.1	0.3	2.1	5.3	10.1	17.0	24.4	33.7	51.4
<b>U6</b>	0.1	0.3	0.4	0.5	0.5	0.7	0.5	1.4	7.3	16.5
<b>V1</b>	82.6	100.8	110.4	118.6	118.6	121.0	131.2	133.5	121.7	112.7
<b>V2</b>	83.7	113.4	130.3	146.4	152.6	159.6	179.7	184.1	172.0	164.1
<b>V3</b>	69.4	104.4	122.1	142.3	151.3	160.2	184.6	190.6	178.8	172.7
<b>V4</b>	53.7	91.8	113.6	135.3	145.7	152.3	170.8	175.2	165.5	162.9
<b>V5</b>	31.8	32.4	34.6	39.0	47.4	62.7	82.7	101.8	108.1	111.0
<b>V6</b>	82.0	82.1	72.3	58.8	29.5	28.1	13.3	5.2	0.3	0.1
<b>V7</b>	81.9	83.1	68.4	51.1	19.3	17.4	8.0	2.6	0.2	2.0
<b>V8</b>	70.2	70.1	52.3	33.1	12.3	11.4	6.5	2.8	0.3	0.1
<b>V9</b>	55.2	54.5	36.0	23.5	11.9	11.5	10.0	7.9	5.6	2.3
<b>V10</b>	32.3	30.9	28.2	24.2	11.2	10.4	1.0	0.2	0.2	0.1

Table A-10: Mooring line tension for different flow directions (Case 3).

Anchor [kN]	Flow direction [°]									
	0	10	20	30	40	50	60	70	80	90
<b>U1</b>	141.6	166.4	173.4	170.0	152.7	136.4	128.4	106.6	79.7	60.0
<b>U2</b>	179.2	201.8	204.5	195.2	171.5	149.7	133.4	104.7	74.6	50.3
<b>U3</b>	141.6	158.2	156.1	143.9	119.2	95.9	74.1	46.6	26.6	16.0
<b>U4</b>	0.1	0.1	0.3	0.6	2.4	7.2	13.7	29.0	44.5	60.3
<b>U5</b>	0.1	0.2	0.5	2.7	5.7	10.2	16.3	23.2	33.8	50.0
<b>U6</b>	0.1	0.4	0.5	0.6	0.6	0.8	0.7	1.6	7.1	15.6
<b>V1</b>	73.8	87.0	96.0	102.1	101.3	103.5	110.5	109.5	101.4	95.8
<b>V2</b>	77.5	98.6	114.0	126.5	130.5	135.8	150.9	153.1	143.0	137.9
<b>V3</b>	65.2	90.6	106.4	121.9	128.5	135.1	154.0	157.9	147.4	143.7
<b>V4</b>	51.5	79.7	98.4	115.6	123.3	128.2	143.1	145.6	138.1	137.1
<b>V5</b>	31.4	32.5	34.5	38.2	45.3	57.5	73.0	86.7	91.7	94.7
<b>V6</b>	73.4	72.2	65.0	53.7	30.5	29.5	16.9	6.3	1.5	0.3
<b>V7</b>	76.4	74.4	63.0	47.9	21.9	20.5	10.8	3.7	1.9	4.1
<b>V8</b>	65.4	63.0	48.7	32.2	12.4	11.4	6.7	3.3	0.9	0.1
<b>V9</b>	52.2	48.8	34.2	23.3	11.7	11.3	9.8	8.3	6.8	4.4
<b>V10</b>	32.0	30.4	28.3	24.8	13.9	13.2	4.3	0.4	0.3	0.4

## Appendix B

# Results of simulations for single-cage fish farm model

---

This appendix provides the results of the simulations performed for the single-cage fish farm model. The results are categorized based on two models, the intact and failure model. In addition, the results for the failure mode is limited to the flow directions in which the maximum mooring line tension occurs. The results presented in this appendix correspond to the discussion in Section 5.2. For the convenience of the reader, the configuration of the single-cage model and the notation of the cables are provided on the next page.

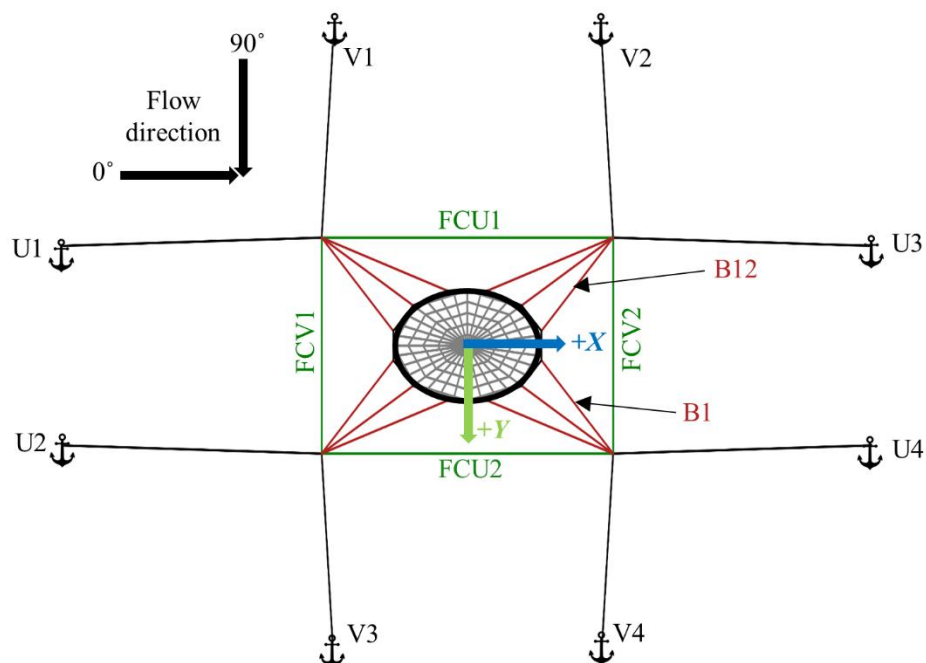


Fig. B-1: Configuration of a single-cage model.

As mentioned in Section 5.2.1, the bridles are numbered in clockwise order starting from the bridles in the first quadrant. The failure modes are considered to fail one of the mooring lines and frame cables. In addition, the pre-tension of the mooring grid is provided in Table B-1, Table B-2, and Table B-3.

Table B-1: Pre-tensions of mooring lines.

Mooring lines [kN]							
U1	U2	U3	U4	V1	V2	V3	V4
58.82	58.82	58.82	58.82	58.82	58.82	58.82	58.82

Table B-2: Pre-tensions of frame cables.

Frame cables [kN]			
FCU1	FCU2	FCV1	FCV2
5.97	5.97	5.97	5.97

Table B-3: Pre-tensions of bridles.

Bridles [kN]											
B1	B2	B3	B4	B5	B6	B7	B8	B9	B10	B11	B12
36.87	2.29	36.87	36.87	2.30	36.87	36.87	2.29	36.87	36.87	2.29	36.87

## B.1 Results from the intact model

Table B-4: Tensions in mooring lines of the intact single-cage model for different flow directions.

Flow direction [°]	Mooring lines [kN]							
	U1	U2	U3	U4	V1	V2	V3	V4
<b>0</b>	80.3	80.3	36.9	36.9	67.6	54.1	67.6	54.1
<b>10</b>	80.8	79.0	38.2	36.6	71.0	57.7	63.7	50.7
<b>20</b>	80.8	77.2	39.9	36.8	74.2	61.4	59.6	47.4
<b>30</b>	80.3	74.8	42.8	37.8	76.7	65.3	55.1	44.2
<b>40</b>	79.5	71.8	46.5	39.5	78.4	68.6	50.7	41.7
<b>50</b>	78.3	68.6	50.7	41.7	79.5	71.8	46.6	39.5
<b>60</b>	76.7	65.3	55.1	44.2	80.3	74.7	42.8	37.8
<b>70</b>	74.2	61.5	59.6	47.3	80.8	77.2	40.0	36.8
<b>80</b>	71.0	57.7	63.7	50.7	80.8	79.0	38.1	36.6
<b>90</b>	67.6	54.1	67.6	54.1	80.3	80.3	36.9	36.9

Table B-5: Tensions in frame cables of the intact single-cage model for different flow directions.

Flow direction [°]	Frame cable [kN]			
	FCU1	FCU2	FCV1	FCV2
<b>0</b>	6.3	6.3	1.8	16.7
<b>10</b>	4.6	8.1	1.8	16.4
<b>20</b>	2.9	9.8	1.7	16.0
<b>30</b>	1.7	11.4	1.6	15.1
<b>40</b>	1.5	12.9	1.5	14.1
<b>50</b>	1.5	14.1	1.5	12.9
<b>60</b>	1.6	15.1	1.7	11.4
<b>70</b>	1.7	16.0	2.9	9.8
<b>80</b>	1.8	16.5	4.6	8.1
<b>90</b>	1.8	16.7	6.3	6.3

Table B-6: Tensions in bridles for different flow directions.

Flow direction [°]	Bridle [kN]											
	B1	B2	B3	B4	B5	B6	B7	B8	B9	B10	B11	B12
<b>0</b>	30.3	0.4	18.3	51.6	8.9	40.1	40.1	8.9	51.6	18.3	0.4	30.3
<b>10</b>	27.5	0.3	17.4	50.6	7.4	37.6	42.6	10.3	52.0	20.0	0.6	33.4
<b>20</b>	24.8	0.2	16.9	49.3	5.8	34.9	45.0	11.4	52.3	22.1	0.8	36.6
<b>30</b>	22.2	0.2	17.2	47.4	4.3	32.3	47.3	12.0	51.8	24.7	1.2	39.9
<b>40</b>	20.1	0.2	18.4	45.2	2.9	29.8	49.1	12.3	50.6	27.2	1.8	42.7
<b>50</b>	18.5	0.2	20.1	42.8	1.8	27.2	50.6	12.3	49.0	29.8	2.9	45.1
<b>60</b>	17.2	0.2	22.2	40.0	1.2	24.7	51.7	12.0	47.3	32.3	4.3	47.4
<b>70</b>	16.8	0.2	24.8	36.6	0.8	22.2	52.2	11.4	45.0	34.9	5.9	49.3
<b>80</b>	17.3	0.3	27.5	33.4	0.6	19.9	52.1	10.3	42.6	37.6	7.4	50.6
<b>90</b>	18.3	0.4	30.3	30.3	0.4	18.3	51.6	8.9	40.1	40.1	8.9	51.6

## B.2 Results from failure mode model

Table B-7: Tensions in mooring lines for different failure modes when the flow direction is 0°.

Failure mode	Mooring line [kN]							
	U1	U2	U3	U4	V1	V2	V3	V4
<b>U1</b>	0.0	106.1	19.0	9.4	45.6	73.4	88.8	27.7
<b>U2</b>	106.0	0.0	9.4	19.0	88.8	27.7	45.7	73.4
<b>U3</b>	65.9	67.8	0.0	43.0	69.6	40.9	53.4	58.2
<b>U4</b>	67.8	65.9	43.0	0.0	53.4	58.2	69.6	41.0
<b>V1</b>	63.0	91.2	48.9	17.2	0.0	66.1	43.6	30.5
<b>V2</b>	87.7	65.7	21.2	44.4	74.0	0.0	49.0	28.5
<b>V3</b>	91.2	63.0	17.2	48.9	43.6	30.5	0.0	66.1
<b>V4</b>	65.7	87.7	44.4	21.2	49.0	28.4	74.0	0.0
<b>FCU1</b>	77.0	80.5	33.5	37.3	68.7	54.8	68.7	54.8
<b>FCU2</b>	80.5	77.0	37.3	33.6	68.7	54.7	68.7	54.8
<b>FCV1</b>	80.3	80.3	37.2	37.2	66.8	54.2	66.8	54.2
<b>FCV2</b>	81.9	81.9	38.8	38.9	69.4	45.4	69.4	45.4



Table B-8: Tensions in frame cables for different failure modes when the flow direction is 0°.

Failure mode	Frame cable [kN]			
	FCU1	FCU2	FCV1	FCV2
<b>U1</b>	0.1	9.3	23.9	25.7
<b>U2</b>	9.3	0.1	24.0	25.7
<b>U3</b>	0.2	12.2	3.7	29.7
<b>U4</b>	12.2	0.2	3.7	29.6
<b>V1</b>	32.7	15.9	0.4	27.7
<b>V2</b>	19.8	15.0	3.5	0.9
<b>V3</b>	15.9	32.7	0.4	27.6
<b>V4</b>	15.0	19.8	3.5	0.9
<b>FCU1</b>	0.0	5.8	1.7	15.7
<b>FCU2</b>	5.8	0.0	1.7	15.7
<b>FCV1</b>	6.1	6.1	0.0	16.4
<b>FCV2</b>	3.8	3.8	1.6	0.0

Table B-9: Tensions in bridles for different failure modes when the flow direction is 0°.

Failure mode	Bridle [kN]											
	B1	B2	B3	B4	B5	B6	B7	B8	B9	B10	B11	B12
<b>U1</b>	0.2	0.1	0.1	72.1	6.1	40.1	21.3	0.3	0.2	0.1	0.2	49.2
<b>U2</b>	49.3	0.2	0.1	0.2	0.3	21.4	40.1	6.1	72.2	0.1	0.1	0.2
<b>U3</b>	18.4	0.3	23.0	39.2	5.2	29.7	48.3	3.0	42.8	0.1	0.2	10.8
<b>U4</b>	10.8	0.2	0.1	42.8	3.0	48.3	29.7	5.2	39.2	23.0	0.3	18.4
<b>V1</b>	1.1	0.2	0.1	74.8	0.5	11.5	0.2	0.2	29.7	0.3	0.3	36.9
<b>V2</b>	15.8	0.3	25.1	33.1	4.8	29.9	49.8	3.9	45.4	1.6	0.2	0.3
<b>V3</b>	36.9	0.3	0.3	29.6	0.2	0.2	11.5	0.5	74.8	0.1	0.2	1.1
<b>V4</b>	0.3	0.2	1.6	45.4	3.8	49.9	29.8	4.8	33.1	25.1	0.3	15.8
<b>FCU1</b>	32.0	0.4	18.4	51.6	9.3	41.3	39.6	10.1	54.1	21.4	0.5	30.5
<b>FCU2</b>	30.5	0.5	21.4	54.1	10.1	39.6	41.2	9.3	51.6	18.4	0.4	32.0
<b>FCV1</b>	30.4	0.4	18.8	51.5	9.3	40.8	40.8	9.3	51.5	18.8	0.4	30.4
<b>FCV2</b>	38.6	0.6	18.9	55.5	10.1	39.7	39.7	10.1	55.5	18.9	0.6	38.6

Table B-10: Tensions in mooring lines for different failure modes when the flow direction is 90°.

Failure mode	Mooring line [kN]							
	U1	U2	U3	U4	V1	V2	V3	V4
<b>U1</b>	0.0	66.1	43.6	30.5	63.0	91.2	48.9	17.2
<b>U2</b>	74.0	0.0	49.0	28.4	87.7	65.7	21.2	44.4
<b>U3</b>	43.6	30.5	0.0	66.1	91.2	63.0	17.2	48.9
<b>U4</b>	49.0	28.5	74.0	0.0	65.7	87.7	44.4	21.2
<b>V1</b>	45.7	73.4	88.8	27.7	0.0	106.0	19.0	9.4
<b>V2</b>	88.8	27.7	45.6	73.4	106.0	0.0	9.4	19.0
<b>V3</b>	69.6	41.0	53.4	58.2	65.8	67.8	0.0	43.0
<b>V4</b>	53.4	58.2	69.6	40.9	67.8	65.9	43.0	0.0
<b>FCU1</b>	66.8	54.2	66.8	54.2	80.2	80.3	37.3	37.2
<b>FCU2</b>	69.4	45.4	69.4	45.4	81.9	81.9	38.8	38.8
<b>FCV1</b>	68.7	54.8	68.7	54.7	77.0	80.6	33.6	37.2
<b>FCV2</b>	68.7	54.8	68.7	54.8	80.5	77.0	37.3	33.6

Table B-11: Tensions in frame cables for different failure modes when the flow direction is 90°.

Failure mode	Frame cable [kN]			
	FCU1	FCU2	FCV1	FCV2
<b>U1</b>	0.4	27.6	32.7	15.9
<b>U2</b>	3.5	0.9	19.8	15.0
<b>U3</b>	0.4	27.6	15.9	32.7
<b>U4</b>	3.5	0.9	15.0	19.8
<b>V1</b>	23.9	25.7	0.1	9.3
<b>V2</b>	24.0	25.7	9.3	0.1
<b>V3</b>	3.7	29.7	0.2	12.2
<b>V4</b>	3.7	29.6	12.2	0.2
<b>FCU1</b>	0.0	16.4	6.1	6.1
<b>FCU2</b>	1.6	0.0	3.8	3.8
<b>FCV1</b>	1.7	15.7	0.0	5.8
<b>FCV2</b>	1.7	15.7	5.8	0.0

Table B-12: Tensions in bridles for different failure modes when the flow direction is 90°.

Failure mode	Bridle [kN]											
	B1	B2	B3	B4	B5	B6	B7	B8	B9	B10	B11	B12
<b>U1</b>	0.1	0.2	1.1	36.9	0.3	0.3	29.6	0.2	0.2	11.5	0.5	74.8
<b>U2</b>	25.1	0.3	15.8	0.3	0.2	1.6	45.4	3.8	49.9	29.8	4.8	33.1
<b>U3</b>	0.3	0.3	36.9	1.1	0.2	0.1	74.8	0.5	11.5	0.2	0.2	29.6
<b>U4</b>	1.6	0.2	0.3	15.8	0.3	25.1	33.1	4.8	29.9	49.9	3.9	45.4
<b>V1</b>	0.1	0.1	0.2	49.3	0.2	0.1	0.2	0.3	21.4	40.1	6.1	72.1
<b>V2</b>	0.1	0.2	49.2	0.2	0.1	0.1	72.1	6.1	40.1	21.4	0.3	0.2
<b>V3</b>	23.0	0.3	18.4	10.8	0.2	0.1	42.8	3.0	48.3	29.7	5.2	39.2
<b>V4</b>	0.1	0.2	10.8	18.4	0.3	23.0	39.2	5.2	29.7	48.3	3.0	42.8
<b>FCU1</b>	18.8	0.4	30.4	30.4	0.4	18.8	51.5	9.3	40.8	40.8	9.3	51.5
<b>FCU2</b>	18.9	0.6	38.6	38.6	0.7	18.9	55.5	10.1	39.7	39.7	10.1	55.5
<b>FCV1</b>	18.4	0.4	32.0	30.5	0.5	21.4	54.1	10.1	39.6	41.2	9.4	51.6
<b>FCV2</b>	21.4	0.5	30.5	32.0	0.4	18.4	51.6	9.3	41.3	39.6	10.1	54.1

## Appendix C

# Results of simulations for 4x1 multi-cage fish farm model

---

This appendix provides the results of the simulations performed for the 4x1 multi-cage fish farm model. The results are categorized based on two models, the intact and failure model. In addition, the results for the failure mode is limited to the flow directions in which the significant change in tension and maximum tension for mooring line, frame cable, and bridle occur. The results presented in this appendix correspond to the discussion in Section 5.3. The notations of cables and the configuration of the 4x1 multi-cage fish farm model are presented on the next page.

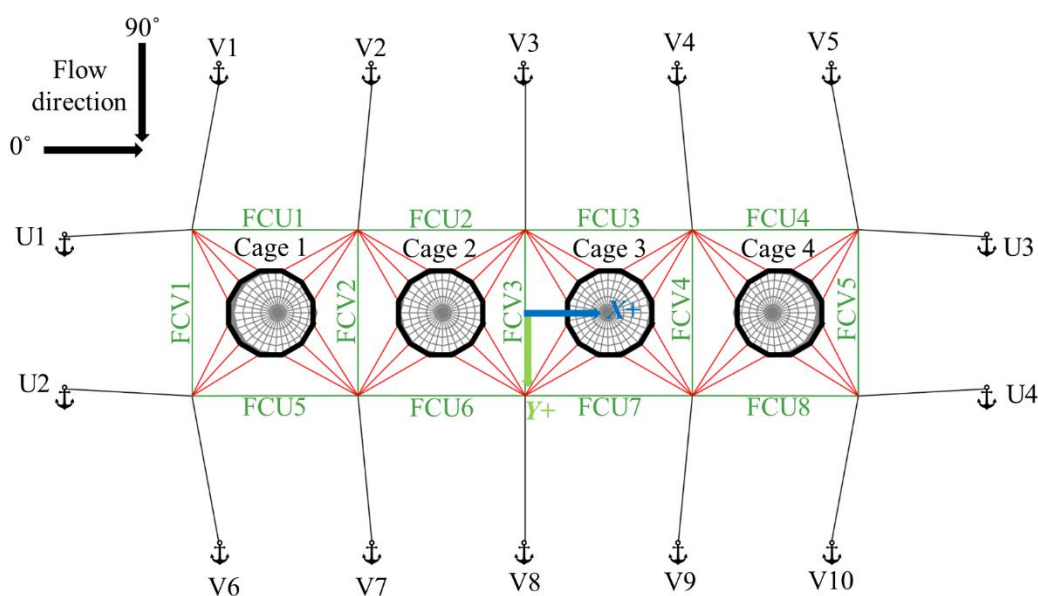


Fig. C-1: Configuration of a 4x1 multi-cage fish farm model.

The numbering of the bridles for each cage is done in the same manner as the single-cage model. Also, the failure modes are considered to fail one of the mooring lines and frame cables. Thus, twenty-seven failure modes are investigated for each flow direction.

## C.1 Results from intact model

Table C-1: Tensions in mooring lines for different flow directions.

Flow direction [°]	Mooring line [kN]													
	U1	U2	U3	U4	V1	V2	V3	V4	V5	V6	V7	V8	V9	V10
0	114.6	114.6	4.4	4.4	70.8	81.3	70.2	59.7	45.7	70.9	81.4	70.0	59.4	45.7
10	128.2	124.6	1.0	0.9	76.7	92.0	83.6	76.6	44.4	69.5	80.1	70.9	59.7	42.7
20	139.1	131.5	1.7	0.9	82.4	103.3	95.9	90.9	45.9	67.2	76.8	66.1	52.8	41.9
30	135.3	124.0	4.4	1.0	84.5	109.3	103.4	99.1	50.3	61.5	68.8	57.7	45.3	39.5
40	123.3	109.1	8.1	1.3	84.1	111.3	106.3	100.6	55.3	54.8	59.8	48.5	38.1	36.8
50	110.1	93.2	12.7	1.7	83.2	112.6	108.5	101.3	60.5	48.1	51.0	40.3	32.1	34.0
60	95.9	76.9	19.5	2.3	81.8	113.4	110.7	102.4	66.0	41.9	43.1	32.8	27.3	31.0
70	81.3	60.5	32.2	5.6	81.2	113.5	112.4	105.3	71.9	37.7	36.7	27.4	25.3	29.5
80	66.8	44.6	43.7	16.4	80.3	112.7	112.7	108.6	75.4	34.8	32.3	24.9	26.8	31.1
90	55.0	29.7	54.6	29.9	78.5	111.6	113.0	110.7	77.8	32.3	28.5	24.0	29.5	33.1

Table C-2: Tensions in frame cables for different flow directions.

Flow direction [°]	Frame cable [kN]												
	FCU1	FCU2	FCU3	FCU4	FCU5	FCU6	FCU7	FCU8	FCV1	FCV2	FCV3	FCV4	FCV5
<b>0</b>	37.1	19.8	0.4	0.2	37.0	19.6	0.4	0.2	1.5	1.7	6.4	17.0	36.3
<b>10</b>	44.6	31.1	7.4	0.1	46.2	30.2	3.8	0.1	1.3	1.4	3.5	10.6	40.9
<b>20</b>	50.1	37.0	12.3	0.1	53.5	37.3	7.9	0.1	1.1	1.1	2.8	9.6	40.3
<b>30</b>	46.3	35.4	12.6	0.2	51.9	37.9	10.1	0.2	1.0	1.0	2.3	8.3	38.1
<b>40</b>	38.0	29.1	8.5	0.3	45.3	34.0	9.1	0.3	1.0	0.9	2.4	8.3	35.7
<b>50</b>	28.8	22.5	4.7	0.5	37.8	29.2	8.0	0.5	1.0	0.8	2.8	8.5	33.2
<b>60</b>	19.5	16.3	2.6	0.7	29.7	24.4	7.6	0.8	1.3	0.8	3.5	8.6	30.4
<b>70</b>	11.0	11.2	2.8	1.0	22.0	20.1	8.1	1.3	4.3	0.9	4.3	7.7	25.3
<b>80</b>	4.2	7.3	3.8	1.3	14.8	16.5	10.0	2.8	8.9	2.2	4.9	6.1	19.3
<b>90</b>	1.9	5.1	5.3	2.0	8.3	13.2	13.0	7.9	14.0	4.2	5.0	4.1	13.9

Table C-3: Tensions in bridles of Cage 1 for different flow directions.

Flow direction [°]	Bridle of Cage 1 [kN]											
	B1	B2	B3	B4	B5	B6	B7	B8	B9	B10	B11	B12
<b>0</b>	20.5	0.4	26.8	51.8	11.8	43.1	43.0	11.8	51.7	26.9	0.4	20.5
<b>10</b>	18.8	0.3	29.6	52.8	11.9	41.8	46.3	15.0	54.7	33.2	0.5	24.5
<b>20</b>	16.2	0.2	31.4	53.2	11.7	40.1	49.4	17.8	57.7	38.1	0.9	27.7
<b>30</b>	13.7	0.2	30.5	49.9	9.3	37.1	51.2	18.0	57.1	39.6	1.2	30.3
<b>40</b>	11.7	0.2	28.2	45.0	6.0	34.0	51.8	16.7	54.4	39.5	1.4	32.2
<b>50</b>	9.8	0.1	25.8	40.1	3.0	30.9	52.3	15.1	51.4	39.2	1.6	34.1
<b>60</b>	8.2	0.1	23.9	34.4	1.3	27.5	52.5	13.3	47.9	39.1	1.9	36.0
<b>70</b>	7.2	0.2	22.2	27.9	0.7	23.0	51.6	10.9	43.8	38.8	2.0	37.9
<b>80</b>	6.5	0.2	21.0	21.5	0.5	18.0	50.0	7.6	38.8	38.0	1.8	39.1
<b>90</b>	4.7	0.3	20.3	15.2	0.3	12.7	48.6	3.5	32.1	35.7	1.1	39.9

Table C-4: Tensions in bridles of Cage 2 for different flow directions.

Flow direction [°]	Bridle of Cage 2 [kN]											
	B1	B2	B3	B4	B5	B6	B7	B8	B9	B10	B11	B12
0	19.0	0.3	10.7	43.8	0.8	29.9	29.8	0.8	43.7	10.9	0.3	19.0
10	15.9	0.2	11.7	45.2	0.8	28.9	31.4	2.6	47.6	16.2	0.4	22.3
20	12.3	0.2	11.1	47.1	0.8	26.9	34.0	5.6	52.0	19.7	0.5	25.6
30	10.3	0.1	9.9	44.0	0.7	22.9	36.8	6.0	51.4	22.3	0.6	28.8
40	7.8	0.1	8.9	38.9	0.5	18.7	38.0	5.5	49.1	23.5	0.7	30.8
50	5.5	0.1	8.5	33.6	0.5	14.8	38.6	4.8	46.4	24.9	0.7	32.8
60	3.8	0.1	8.3	28.3	0.5	11.3	39.1	3.7	43.4	26.5	0.7	34.9
70	2.7	0.1	8.8	23.2	0.4	8.7	39.2	2.6	39.9	29.0	0.7	37.2
80	2.8	0.2	10.2	18.6	0.3	6.2	38.7	1.3	36.3	31.3	0.7	38.9
90	3.9	0.3	12.7	14.2	0.3	4.3	38.2	0.8	33.0	33.6	0.8	40.0

Table C-5: Tensions in bridles of Cage 3 for different flow directions.

Flow direction [°]	Bridle of Cage 3 [kN]											
	B1	B2	B3	B4	B5	B6	B7	B8	B9	B10	B11	B12
0	18.9	0.3	6.9	31.6	0.4	27.6	27.2	0.5	32.3	6.0	0.3	19.4
10	17.1	0.2	9.9	38.1	0.6	31.3	32.1	2.0	42.7	13.1	0.4	23.6
20	13.8	0.2	7.4	40.0	0.7	29.8	36.3	5.1	47.1	15.6	0.5	25.6
30	11.9	0.1	6.0	37.3	0.7	25.5	39.9	5.5	47.3	17.9	0.6	27.9
40	9.9	0.1	6.0	33.0	0.5	20.8	41.2	5.1	45.7	19.6	0.6	30.0
50	7.8	0.1	6.6	28.7	0.5	16.2	41.6	4.4	43.9	21.1	0.7	32.1
60	5.6	0.1	7.1	24.3	0.5	11.3	42.3	3.1	41.2	22.2	0.7	34.3
70	3.6	0.1	8.1	19.9	0.4	8.0	41.7	2.1	38.4	25.4	0.7	36.5
80	3.6	0.2	10.6	16.0	0.3	6.1	40.4	1.1	35.8	29.4	0.7	37.1
90	4.6	0.3	14.4	12.8	0.3	4.2	39.7	0.8	33.5	32.9	0.8	37.8

Table C-6: Tensions in bridles of Cage 4 for different flow directions.

Flow direction [°]	Bridle of Cage 4 [kN]											
	B1	B2	B3	B4	B5	B6	B7	B8	B9	B10	B11	B12
<b>0</b>	8.4	0.2	0.2	10.8	0.3	17.2	18.3	0.3	9.5	0.2	0.2	8.4
<b>10</b>	0.2	0.1	0.1	15.1	0.3	23.2	26.4	0.4	26.6	0.2	0.2	1.7
<b>20</b>	0.1	0.1	0.1	17.3	0.3	20.3	34.6	0.5	34.6	0.2	0.2	3.7
<b>30</b>	0.1	0.1	0.1	19.4	0.4	15.1	41.0	0.5	35.5	0.2	0.3	10.5
<b>40</b>	0.1	0.1	0.1	19.3	0.4	9.3	41.7	0.4	31.7	0.3	0.3	18.3
<b>50</b>	0.1	0.1	0.1	19.2	0.4	4.3	40.9	0.4	28.5	0.4	0.3	26.8
<b>60</b>	0.2	0.1	0.2	18.5	0.4	1.4	40.3	0.3	26.3	3.0	0.5	34.5
<b>70</b>	4.1	0.1	1.0	17.3	0.4	2.5	38.2	0.4	30.0	14.3	0.5	40.3
<b>80</b>	8.6	0.2	8.9	19.4	0.3	3.8	39.3	0.6	32.9	23.9	0.8	45.4
<b>90</b>	13.5	0.3	15.5	20.4	0.3	5.4	39.4	1.1	35.7	32.0	3.4	48.0



## C.2 Results from failure mode model

Table C-7: Tensions in mooring lines for different failure modes (flow direction = 20°).

Failure mode	Mooring line [kN]													
	U1	U2	U3	U4	V1	V2	V3	V4	V5	V6	V7	V8	V9	V10
<b>U1</b>	0.0	211.5	0.5	0.7	63.2	128.5	114.8	105.7	43.9	96.5	68.4	66.0	59.6	43.0
<b>U2</b>	212.5	0.0	0.5	0.7	108.5	90.9	94.2	98.8	44.0	44.8	97.2	84.0	62.6	43.0
<b>U3</b>	138.9	131.2	0.0	1.3	82.3	103.1	95.8	91.7	44.5	67.2	76.8	66.0	51.6	42.3
<b>U4</b>	139.2	131.5	2.1	0.0	82.4	103.3	95.9	90.9	45.7	67.2	76.8	66.2	52.9	41.7
<b>V1</b>	127.8	145.9	0.8	0.8	0.0	120.2	98.9	89.1	44.3	37.9	50.0	65.6	55.7	42.7
<b>V2</b>	147.3	125.6	0.7	0.8	96.1	0.0	117.5	94.5	44.1	38.4	61.0	49.5	51.6	42.8
<b>V3</b>	146.9	130.7	0.9	0.8	85.9	118.5	0.0	114.1	44.4	66.3	58.6	50.5	33.5	42.6
<b>V4</b>	146.1	135.6	11.5	0.5	83.0	109.0	111.2	0.0	76.6	68.9	76.1	51.5	46.2	26.4
<b>V5</b>	139.0	131.4	1.7	0.9	82.4	103.2	95.9	90.8	45.9	67.2	76.8	66.2	52.8	41.9
<b>V6</b>	149.6	119.0	2.1	0.9	58.4	79.3	95.7	93.9	46.7	0.0	89.3	69.0	51.1	41.5
<b>V7</b>	136.0	133.9	2.1	0.9	61.6	93.3	74.5	92.4	46.8	76.5	0.0	79.8	55.6	41.4
<b>V8</b>	139.4	135.1	3.0	0.9	80.4	94.0	87.0	68.1	48.4	70.1	86.6	0.0	66.8	40.6
<b>V9</b>	142.7	137.0	0.6	3.8	84.1	103.8	87.3	76.6	39.4	67.4	80.1	76.8	0.0	51.5
<b>V10</b>	140.7	133.1	4.5	0.1	83.1	104.5	96.5	86.0	14.7	67.1	76.8	67.0	60.2	0.0
<b>FCU1</b>	119.4	142.4	1.2	0.8	92.6	108.3	98.7	95.6	45.2	78.2	89.5	64.3	51.7	42.2
<b>FCU2</b>	132.7	132.5	2.0	0.9	84.2	104.5	99.0	95.7	46.8	62.2	87.0	76.9	50.0	41.4
<b>FCU3</b>	138.2	131.1	2.3	0.9	82.9	103.0	95.8	93.9	47.2	66.5	75.8	70.6	55.7	41.2
<b>FCU4</b>	138.9	131.3	1.6	0.9	82.3	103.1	95.8	90.8	45.9	67.2	76.7	66.1	52.9	41.9
<b>FCU5</b>	150.3	109.6	0.8	0.8	94.2	116.7	93.7	91.2	44.3	78.5	82.2	68.8	55.9	42.7
<b>FCU6</b>	139.9	124.7	0.7	0.8	77.2	113.4	106.8	88.3	44.0	69.1	78.0	69.6	56.8	42.9
<b>FCU7</b>	138.6	130.6	0.9	0.9	81.8	102.4	98.4	92.9	44.6	67.5	76.6	66.1	54.2	42.6
<b>FCU8</b>	139.0	131.4	1.7	0.8	82.4	103.2	95.8	90.8	45.9	67.2	76.8	66.1	52.9	41.9
<b>FCV1</b>	138.8	131.1	1.7	0.9	81.8	103.2	95.7	90.8	45.9	66.7	76.8	66.1	52.9	41.8
<b>FCV2</b>	138.8	131.1	1.7	0.9	82.3	102.8	95.8	90.7	45.9	67.2	76.3	66.2	52.9	41.8
<b>FCV3</b>	138.9	131.2	1.7	0.9	82.3	103.2	94.9	90.8	46.0	67.2	76.8	65.2	52.9	41.8
<b>FCV4</b>	139.0	131.4	1.8	0.9	82.4	103.1	96.2	86.8	46.0	67.2	76.7	66.6	49.0	41.8
<b>FCV5</b>	140.9	133.3	5.2	0.6	83.1	104.4	96.6	87.2	15.9	67.3	77.0	67.1	59.7	2.7

Table C-8: Tensions in frame cables for different failure modes (flow direction = 20°).

Failure mode	Frame cable [kN]												
	FCU1	FCU2	FCU3	FCU4	FCU5	FCU6	FCU7	FCU8	FCV1	FCV2	FCV3	FCV4	FCV5
<b>U1</b>	0.1	11.0	2.5	0.1	91.0	39.1	1.2	0.1	22.7	1.2	6.5	15.7	41.4
<b>U2</b>	85.1	36.9	7.2	0.1	0.2	10.4	0.5	0.1	20.4	1.5	6.3	15.6	41.4
<b>U3</b>	49.9	37.1	12.6	0.1	53.2	36.9	7.0	0.1	1.1	1.1	2.8	9.8	40.7
<b>U4</b>	50.0	37.1	12.3	0.1	53.5	37.3	7.9	0.1	1.1	1.1	2.7	9.7	40.1
<b>V1</b>	76.3	43.4	16.2	0.1	71.7	23.4	2.6	0.1	0.4	1.2	2.6	10.3	41.1
<b>V2</b>	69.4	41.6	12.8	0.1	76.5	50.8	5.8	0.1	1.6	0.3	2.2	10.6	41.2
<b>V3</b>	53.8	44.9	20.0	0.1	52.2	61.1	19.4	0.1	1.1	1.2	0.3	7.6	41.0
<b>V4</b>	55.8	42.0	18.4	0.2	55.5	39.6	35.6	0.1	1.1	1.0	3.4	0.2	25.5
<b>V5</b>	50.0	37.1	12.3	0.1	53.4	37.3	7.9	0.1	1.1	1.1	2.7	9.7	40.3
<b>V6</b>	66.6	24.9	8.5	0.1	76.1	42.1	11.5	0.1	0.4	1.3	2.5	10.0	39.9
<b>V7</b>	65.6	57.0	6.4	0.1	63.1	44.8	6.8	0.1	1.4	0.4	5.9	9.7	39.8
<b>V8</b>	51.4	52.0	31.9	0.1	54.4	33.2	17.2	0.1	1.1	1.1	0.4	17.9	39.0
<b>V9</b>	51.6	37.6	24.6	0.1	58.1	43.1	14.8	0.1	1.1	1.1	2.8	0.2	37.4
<b>V10</b>	50.7	36.7	10.1	0.1	54.9	40.3	13.3	0.5	1.1	1.1	2.6	9.3	0.3
<b>FCU1</b>	0.0	30.1	8.3	0.1	55.0	46.5	7.8	0.1	0.8	1.0	3.6	10.5	40.7
<b>FCU2</b>	44.6	0.0	8.1	0.1	60.6	38.7	14.6	0.1	1.2	0.9	1.7	11.1	39.8
<b>FCU3</b>	48.7	35.3	0.0	0.1	53.6	40.2	7.5	0.1	1.1	1.1	2.1	8.1	39.6
<b>FCU4</b>	49.9	37.0	12.3	0.0	53.3	37.2	8.0	0.1	1.1	1.1	2.7	9.6	40.3
<b>FCU5</b>	51.3	47.0	13.0	0.1	0.0	28.7	2.4	0.1	0.8	0.9	3.7	10.6	41.1
<b>FCU6</b>	57.0	38.3	19.2	0.1	47.6	0.0	3.0	0.1	1.2	1.0	1.7	11.4	41.2
<b>FCU7</b>	50.0	38.8	12.1	0.1	52.4	35.8	0.0	0.1	1.1	1.1	2.4	8.6	40.9
<b>FCU8</b>	50.0	37.0	12.3	0.1	53.4	37.3	7.9	0.0	1.1	1.1	2.7	9.7	40.3
<b>FCV1</b>	49.8	37.1	12.3	0.1	53.2	37.3	8.0	0.1	0.0	1.1	2.7	9.6	40.2
<b>FCV2</b>	49.7	36.9	12.3	0.1	53.1	37.2	8.0	0.1	1.1	0.0	2.7	9.6	40.2
<b>FCV3</b>	49.9	36.6	12.0	0.1	53.3	36.8	7.7	0.1	1.1	1.1	0.0	9.6	40.2
<b>FCV4</b>	49.9	37.2	10.8	0.1	53.3	37.5	6.7	0.1	1.1	1.1	2.7	0.0	40.2
<b>FCV5</b>	50.9	37.1	11.0	0.1	55.0	40.2	13.1	0.1	1.1	1.1	2.6	9.2	0.0

Table C-9: Tensions in frame cables for different failure modes (flow direction = 50°).

Failure mode	Frame cable [kN]													
	FCU1	FCU2	FCU3	FCU4	FCU5	FCU6	FCU7	FCU8	FCV1	FCV2	FCV3	FCV4	FCV5	
<b>U1</b>	0.3	3.9	1.6	0.3	71.9	28.1	1.4	0.3	26.7	0.7	5.6	13.5	36.5	
<b>U2</b>	58.9	22.2	2.8	0.3	0.4	8.5	1.2	0.3	18.5	1.5	5.3	12.6	35.7	
<b>U3</b>	27.4	22.0	6.1	0.3	35.6	25.5	2.4	0.5	1.0	0.8	3.1	9.3	38.0	
<b>U4</b>	28.7	22.4	4.7	0.4	37.7	29.1	7.9	0.3	1.0	0.8	2.8	8.5	32.8	
<b>V1</b>	50.9	34.4	9.7	0.5	44.7	16.0	2.3	0.4	0.2	0.6	2.5	8.7	34.0	
<b>V2</b>	45.3	24.2	10.8	0.5	66.6	31.1	5.5	0.4	4.4	0.2	0.8	9.8	35.0	
<b>V3</b>	31.8	24.7	10.7	0.7	36.3	61.2	11.3	0.4	0.9	0.9	0.1	2.4	35.0	
<b>V4</b>	35.7	26.8	4.8	2.1	41.5	35.4	47.1	0.4	0.9	0.7	3.7	0.1	13.8	
<b>V5</b>	28.8	22.5	4.7	0.4	37.7	29.2	7.9	0.4	1.0	0.8	2.8	8.5	33.2	
<b>V6</b>	41.4	13.2	2.6	0.4	56.6	32.4	10.5	0.4	0.3	1.1	2.6	8.9	33.0	
<b>V7</b>	40.2	36.5	2.1	0.4	45.3	34.8	6.6	0.4	2.0	0.3	5.6	8.7	33.1	
<b>V8</b>	30.0	31.8	19.9	0.4	37.3	24.2	16.5	0.5	1.0	0.8	0.3	14.6	32.5	
<b>V9</b>	26.9	20.9	10.6	0.5	36.5	26.4	2.2	0.5	1.0	0.8	3.3	0.3	39.1	
<b>V10</b>	29.4	22.2	3.3	0.5	38.9	31.5	12.2	0.8	0.9	0.8	2.7	8.6	0.6	
<b>FCU1</b>	0.0	18.4	2.9	0.4	38.8	34.6	7.7	0.4	0.6	0.7	3.5	9.0	33.5	
<b>FCU2</b>	25.5	0.0	2.7	0.4	42.3	30.0	12.0	0.4	1.1	0.7	1.6	9.3	33.0	
<b>FCU3</b>	28.3	21.8	0.0	0.4	37.9	30.3	7.7	0.4	1.0	0.8	2.4	8.0	32.9	
<b>FCU4</b>	28.7	22.3	4.5	0.0	37.6	29.1	8.0	0.4	1.0	0.8	2.8	8.6	33.2	
<b>FCU5</b>	30.2	30.1	5.4	0.4	0.0	22.7	3.5	0.4	0.6	0.7	3.6	9.1	34.1	
<b>FCU6</b>	34.3	23.5	10.3	0.4	32.7	0.0	3.1	0.4	1.1	0.7	1.5	9.7	34.6	
<b>FCU7</b>	28.7	24.0	4.5	0.5	36.6	27.6	0.0	0.4	1.0	0.8	2.3	7.7	34.0	
<b>FCU8</b>	28.7	22.4	4.7	0.5	37.6	29.1	7.8	0.0	1.0	0.8	2.8	8.5	33.1	
<b>FCV1</b>	28.6	22.5	4.7	0.5	37.6	29.2	8.0	0.4	0.0	0.8	2.8	8.5	33.1	
<b>FCV2</b>	28.6	22.4	4.7	0.5	37.6	29.1	8.0	0.4	1.0	0.0	2.8	8.5	33.1	
<b>FCV3</b>	28.8	22.1	4.4	0.5	37.7	28.9	7.7	0.4	1.0	0.8	0.0	8.5	33.1	
<b>FCV4</b>	28.8	22.7	3.7	0.5	37.8	29.3	7.1	0.5	1.0	0.8	2.8	0.0	33.2	
<b>FCV5</b>	30.2	23.5	5.3	0.4	39.6	31.8	12.0	0.4	0.9	0.8	2.5	8.2	0.0	

Table C-10: Tensions in bridles of Cage 1 for different failure modes (flow direction = 50°).

Failure mode	Bridle of Cage 1 [kN]											
	B1	B2	B3	B4	B5	B6	B7	B8	B9	B10	B11	B12
<b>U1</b>	0.1	0.1	0.7	72.9	1.6	25.3	39.6	0.3	0.3	3.6	0.6	85.2
<b>U2</b>	34.4	0.1	15.2	0.3	0.3	9.3	51.0	14.4	79.1	28.9	2.1	6.6
<b>U3</b>	9.4	0.1	24.5	39.7	2.7	31.0	51.8	14.8	50.7	38.9	1.5	34.2
<b>U4</b>	9.8	0.1	25.8	40.0	3.0	30.9	52.3	15.1	51.4	39.2	1.6	34.1
<b>V1</b>	0.1	0.1	0.1	67.4	0.3	0.2	0.4	0.3	45.5	29.6	1.1	58.9
<b>V2</b>	0.2	0.1	40.4	15.3	0.8	3.7	71.9	6.1	43.3	0.2	0.1	0.1
<b>V3</b>	14.2	0.2	26.8	38.4	3.2	29.9	53.3	16.1	55.7	39.0	2.5	32.8
<b>V4</b>	10.2	0.2	27.2	41.1	3.7	32.1	52.2	16.4	53.2	42.2	2.1	34.0
<b>V5</b>	9.8	0.1	25.8	40.1	3.0	30.9	52.3	15.1	51.4	39.2	1.6	34.1
<b>V6</b>	15.7	0.1	12.1	24.3	0.3	0.3	37.0	4.9	62.1	19.6	0.7	20.9
<b>V7</b>	0.1	0.1	0.2	30.3	0.8	40.0	37.0	13.5	45.3	48.3	1.0	30.4
<b>V8</b>	8.8	0.2	24.5	41.4	3.0	32.4	50.9	15.4	50.6	41.0	1.7	35.6
<b>V9</b>	9.5	0.1	25.2	39.7	2.8	30.6	52.2	14.8	50.8	38.4	1.5	34.0
<b>V10</b>	10.1	0.2	26.5	40.2	3.2	30.7	52.7	15.3	51.8	39.2	1.7	33.9
<b>FCU1</b>	18.6	0.2	27.8	41.7	5.1	36.6	50.0	21.6	64.7	52.6	7.3	33.6
<b>FCU2</b>	7.6	0.1	28.8	37.8	2.8	27.9	55.3	14.0	50.0	35.2	1.1	30.1
<b>FCU3</b>	10.0	0.1	26.0	40.0	3.0	30.6	52.6	15.1	51.5	38.8	1.6	34.0
<b>FCU4</b>	9.8	0.1	25.7	40.0	3.0	30.9	52.3	15.1	51.4	39.1	1.6	34.1
<b>FCU5</b>	13.3	0.3	46.7	57.9	10.5	28.8	59.3	19.2	53.7	41.1	4.2	44.1
<b>FCU6</b>	3.9	0.1	19.7	37.9	1.9	34.6	48.4	14.8	48.3	42.9	1.2	31.7
<b>FCU7</b>	9.7	0.1	25.0	40.1	2.9	31.3	51.8	15.1	51.2	39.5	1.6	34.5
<b>FCU8</b>	9.8	0.1	25.7	40.0	3.0	30.9	52.3	15.1	51.4	39.2	1.6	34.1
<b>FCV1</b>	9.8	0.1	26.0	40.0	3.2	31.3	52.7	15.3	51.3	39.4	1.7	34.1
<b>FCV2</b>	10.1	0.2	25.7	40.1	3.0	30.8	52.3	15.1	51.5	39.1	1.7	34.3
<b>FCV3</b>	9.8	0.1	25.7	40.0	3.0	30.9	52.3	15.1	51.4	39.2	1.6	34.0
<b>FCV4</b>	9.8	0.1	25.8	40.1	3.0	30.9	52.3	15.2	51.4	39.2	1.6	34.1
<b>FCV5</b>	10.1	0.2	26.7	40.4	3.3	30.9	52.7	15.5	52.0	39.7	1.7	34.1

Table C-11: Tensions in bridles of Cage 2 for different failure modes (flow direction = 50°).

Failure mode	Bridle of Cage 2 [kN]											
	B1	B2	B3	B4	B5	B6	B7	B8	B9	B10	B11	B12
U1	0.3	0.1	2.6	43.1	0.5	18.9	33.2	3.7	37.0	25.7	0.7	43.8
U2	14.8	0.1	12.0	22.8	0.5	14.1	46.0	6.8	54.0	22.5	0.8	25.3
U3	4.7	0.1	6.5	33.2	0.5	15.7	37.4	4.7	45.4	25.5	0.7	33.0
U4	5.5	0.1	8.5	33.6	0.5	14.8	38.6	4.8	46.3	24.8	0.7	32.8
V1	10.8	0.1	6.5	26.7	0.5	12.7	37.7	5.8	53.4	26.9	0.8	28.1
V2	0.1	0.0	0.1	77.9	0.2	0.2	0.1	0.1	22.3	14.1	0.9	78.0
V3	0.2	0.1	22.1	6.1	0.3	0.4	59.2	1.4	43.5	0.2	0.1	0.1
V4	11.3	0.1	13.5	33.7	0.5	12.6	41.7	5.8	52.1	24.3	0.8	32.1
V5	5.5	0.1	8.5	33.6	0.5	14.8	38.6	4.8	46.3	24.8	0.7	32.8
V6	3.6	0.1	11.9	38.0	0.6	19.5	41.9	6.0	42.6	26.0	0.7	35.8
V7	10.4	0.1	0.2	11.2	0.2	0.2	34.2	1.0	55.4	15.3	0.6	14.5
V8	0.1	0.1	0.1	34.2	0.5	20.4	31.6	5.0	43.1	31.8	0.7	34.0
V9	4.8	0.1	6.9	34.0	0.5	15.6	37.6	4.7	45.2	25.4	0.7	33.8
V10	6.2	0.1	9.9	33.8	0.5	14.0	39.6	4.7	46.9	24.2	0.7	32.6
FCU1	2.0	0.1	5.9	37.5	0.5	12.2	34.7	2.5	42.6	22.4	0.6	36.0
FCU2	12.5	0.1	10.6	36.1	0.6	21.9	37.7	9.8	56.3	37.9	1.5	34.5
FCU3	5.1	0.1	9.0	33.2	0.5	14.2	39.1	4.5	46.0	24.0	0.7	32.1
FCU4	5.6	0.1	8.5	33.6	0.5	14.7	38.7	4.7	46.3	24.8	0.7	32.7
FCU5	9.4	0.1	5.3	26.9	0.4	8.0	36.3	3.3	51.7	21.7	0.7	27.9
FCU6	8.8	0.2	24.6	48.8	0.9	17.4	45.6	7.8	48.5	28.1	1.0	41.4
FCU7	4.1	0.1	6.8	32.8	0.5	15.6	37.6	4.7	45.6	25.7	0.7	32.0
FCU8	5.5	0.1	8.5	33.6	0.5	14.8	38.6	4.7	46.3	24.8	0.7	32.8
FCV1	5.5	0.1	8.5	33.6	0.5	14.7	38.6	4.7	46.3	24.8	0.7	32.8
FCV2	5.5	0.1	8.6	33.5	0.5	15.1	38.9	4.9	46.3	25.0	0.7	32.7
FCV3	6.7	0.1	8.2	34.0	0.5	14.7	38.5	4.8	46.8	24.7	0.7	33.7
FCV4	5.4	0.1	8.4	33.5	0.5	14.8	38.6	4.7	46.3	24.9	0.7	32.6
FCV5	6.2	0.1	9.8	34.2	0.5	14.4	39.2	4.9	47.1	24.9	0.7	32.9

Table C-12: Tensions in bridles of Cage 3 for different failure modes (flow direction = 50°).

Failure mode	Bridle of Cage 3 [kN]											
	B1	B2	B3	B4	B5	B6	B7	B8	B9	B10	B11	B12
<b>U1</b>	7.3	0.1	2.6	27.5	0.5	17.9	40.4	4.1	41.3	20.6	0.6	33.5
<b>U2</b>	10.2	0.1	3.8	24.4	0.5	16.4	41.8	4.3	45.0	20.0	0.7	30.4
<b>U3</b>	7.4	0.1	3.2	27.4	0.5	17.4	39.5	4.4	43.5	22.4	0.7	31.9
<b>U4</b>	7.8	0.1	6.6	28.7	0.5	16.2	41.6	4.3	43.8	21.1	0.7	32.1
<b>V1</b>	12.2	0.1	7.4	22.9	0.5	13.8	43.4	4.7	48.8	19.9	0.7	27.7
<b>V2</b>	9.5	0.1	1.7	25.3	0.4	9.6	35.9	2.7	47.2	19.4	0.7	30.4
<b>V3</b>	0.1	0.0	0.1	75.8	0.2	0.2	0.1	0.1	14.2	8.4	0.8	80.2
<b>V4</b>	0.6	0.1	26.0	6.9	0.4	0.6	61.7	1.9	43.5	0.1	0.1	0.1
<b>V5</b>	7.8	0.1	6.7	28.7	0.5	16.2	41.6	4.3	43.8	21.1	0.7	32.1
<b>V6</b>	5.5	0.1	5.6	31.3	0.5	16.7	40.2	3.9	41.0	20.9	0.6	34.4
<b>V7</b>	7.5	0.1	8.8	29.9	0.5	19.0	44.3	5.2	42.4	21.3	0.7	32.9
<b>V8</b>	7.6	0.1	0.1	7.7	0.2	0.2	36.2	0.6	50.0	11.0	0.5	12.2
<b>V9</b>	0.1	0.1	0.1	28.2	0.5	20.0	36.5	4.0	38.7	25.2	0.6	30.9
<b>V10</b>	7.9	0.1	8.6	29.0	0.5	15.0	43.0	4.1	43.8	19.6	0.7	32.0
<b>FCU1</b>	6.7	0.1	6.2	30.1	0.5	17.4	41.3	4.4	42.1	21.5	0.7	33.6
<b>FCU2</b>	4.7	0.1	4.3	32.0	0.5	14.9	38.4	2.9	40.4	19.7	0.6	35.0
<b>FCU3</b>	9.4	0.1	6.8	29.3	0.5	18.4	41.1	5.7	46.1	24.8	0.7	32.6
<b>FCU4</b>	7.8	0.1	6.7	28.7	0.5	16.1	41.7	4.3	43.8	20.9	0.7	32.1
<b>FCU5</b>	10.0	0.1	7.1	26.2	0.5	16.1	43.0	4.8	45.9	20.9	0.7	30.5
<b>FCU6</b>	11.7	0.1	4.7	22.8	0.4	10.8	40.4	3.3	48.6	18.4	0.7	28.0
<b>FCU7</b>	9.0	0.1	11.9	32.9	0.6	16.6	44.3	5.1	44.6	21.5	0.7	34.5
<b>FCU8</b>	7.7	0.1	6.5	28.7	0.5	16.2	41.6	4.3	43.8	21.1	0.7	32.1
<b>FCV1</b>	7.8	0.1	6.7	28.7	0.5	16.2	41.6	4.3	43.8	21.1	0.7	32.1
<b>FCV2</b>	7.8	0.1	6.6	28.7	0.5	16.2	41.6	4.3	43.9	21.1	0.7	32.1
<b>FCV3</b>	7.7	0.1	7.0	28.3	0.5	17.4	42.5	4.6	43.6	21.6	0.7	32.0
<b>FCV4</b>	12.0	0.1	5.6	29.8	0.5	16.1	41.1	4.5	45.5	20.6	0.7	35.7
<b>FCV5</b>	7.9	0.1	8.2	29.1	0.5	15.8	42.5	4.4	44.3	20.9	0.7	31.9

Table C-13: Tensions in bridles of Cage 4 for different failure modes (flow direction = 50°).

Failure mode	Bridle of Cage 4 [kN]											
	B1	B2	B3	B4	B5	B6	B7	B8	B9	B10	B11	B12
<b>U1</b>	0.1	0.0	0.1	8.7	0.4	4.1	43.5	0.4	31.0	0.2	0.2	15.9
<b>U2</b>	0.1	0.0	0.1	11.1	0.4	4.4	43.0	0.4	30.0	0.2	0.2	18.3
<b>U3</b>	0.1	0.1	0.1	8.7	0.4	2.7	42.3	0.4	31.7	0.2	0.2	14.9
<b>U4</b>	0.1	0.1	0.1	19.2	0.4	4.3	40.8	0.4	28.4	0.4	0.3	26.9
<b>V1</b>	0.1	0.1	0.1	16.4	0.4	3.9	41.3	0.4	29.7	0.4	0.3	23.9
<b>V2</b>	0.1	0.1	0.1	13.1	0.4	3.7	42.2	0.4	30.9	0.4	0.3	20.7
<b>V3</b>	0.1	0.1	0.1	12.7	0.4	0.9	40.4	0.4	32.5	0.9	0.4	20.4
<b>V4</b>	0.0	0.0	0.1	77.0	0.2	0.1	0.1	0.1	2.3	0.9	0.6	87.8
<b>V5</b>	0.1	0.1	0.1	19.2	0.4	4.3	40.9	0.4	28.5	0.4	0.3	26.8
<b>V6</b>	0.1	0.1	0.1	19.7	0.4	4.5	40.9	0.4	27.9	0.4	0.3	27.4
<b>V7</b>	0.1	0.1	0.1	19.6	0.4	4.3	40.7	0.4	27.9	0.3	0.3	27.1
<b>V8</b>	0.1	0.1	0.1	20.5	0.4	7.4	42.8	0.4	26.0	0.3	0.3	28.9
<b>V9</b>	0.1	0.1	0.1	1.2	0.2	0.2	42.4	0.4	36.7	0.3	0.3	7.3
<b>V10</b>	0.1	0.1	0.1	26.2	0.4	5.2	39.8	0.3	24.9	0.5	0.4	35.0
<b>FCU1</b>	0.1	0.1	0.1	18.0	0.4	4.2	41.1	0.4	28.5	0.3	0.3	25.6
<b>FCU2</b>	0.1	0.1	0.1	19.6	0.4	4.7	41.1	0.4	27.6	0.3	0.3	27.4
<b>FCU3</b>	0.1	0.1	0.1	20.1	0.4	4.1	40.4	0.3	28.1	0.4	0.3	27.6
<b>FCU4</b>	0.1	0.1	0.1	19.2	0.4	4.3	40.9	0.4	28.4	0.4	0.3	26.9
<b>FCU5</b>	0.1	0.1	0.1	16.3	0.4	4.0	41.4	0.4	29.2	0.3	0.3	23.7
<b>FCU6</b>	0.1	0.1	0.1	14.5	0.4	4.0	42.0	0.4	30.0	0.3	0.3	22.0
<b>FCU7</b>	0.1	0.1	0.1	16.7	0.4	3.2	40.8	0.4	29.8	0.4	0.3	24.0
<b>FCU8</b>	0.1	0.1	0.1	19.3	0.4	4.3	40.9	0.4	28.4	0.4	0.3	27.0
<b>FCV1</b>	0.1	0.1	0.1	19.2	0.4	4.3	40.8	0.4	28.4	0.4	0.3	26.9
<b>FCV2</b>	0.1	0.1	0.1	19.2	0.4	4.3	40.9	0.4	28.4	0.4	0.3	26.9
<b>FCV3</b>	0.1	0.1	0.1	19.3	0.4	4.2	40.8	0.4	28.5	0.4	0.3	26.9
<b>FCV4</b>	0.1	0.1	0.1	17.6	0.4	7.2	43.6	0.4	27.2	0.4	0.3	26.8
<b>FCV5</b>	6.9	0.1	0.1	26.1	0.4	4.7	40.2	0.4	29.1	0.4	0.4	38.1

Table C-14: Tensions in bridles of Cage 1 for different failure modes (flow direction = 70°).

Failure mode	Bridle of Cage 1 [kN]											
	B1	B2	B3	B4	B5	B6	B7	B8	B9	B10	B11	B12
<b>U1</b>	0.1	0.1	0.2	56.0	0.6	8.3	37.1	0.2	0.2	2.3	0.5	82.7
<b>U2</b>	21.0	0.1	12.7	0.4	0.3	3.1	46.6	7.7	60.4	28.3	1.3	18.8
<b>U3</b>	6.2	0.2	19.6	26.5	0.6	22.1	50.3	9.8	42.3	37.4	1.5	37.9
<b>U4</b>	7.1	0.2	21.9	27.6	0.7	22.7	51.5	10.7	43.6	38.4	1.9	37.9
<b>V1</b>	0.1	0.1	0.1	59.0	0.2	0.2	0.3	0.3	35.0	35.6	3.0	67.8
<b>V2</b>	0.1	0.1	42.3	0.4	0.2	0.2	78.0	4.7	36.9	0.3	0.2	0.1
<b>V3</b>	6.6	0.2	22.1	22.9	0.7	22.9	52.2	11.4	46.5	40.0	1.8	31.7
<b>V4</b>	7.4	0.2	21.1	29.1	0.7	25.8	50.1	12.2	45.0	42.5	2.8	38.6
<b>V5</b>	7.2	0.2	22.2	27.9	0.7	23.0	51.6	10.9	43.8	38.8	2.0	37.9
<b>V6</b>	11.7	0.1	11.3	12.5	0.3	0.2	41.0	3.6	51.7	24.6	0.8	26.5
<b>V7</b>	0.1	0.1	0.9	18.9	0.5	27.3	38.9	9.2	39.5	44.7	1.1	35.7
<b>V8</b>	7.0	0.2	21.3	28.6	0.7	23.5	50.8	10.9	43.3	39.3	2.1	39.0
<b>V9</b>	6.9	0.2	21.6	27.3	0.7	22.3	51.4	10.4	43.2	37.8	1.8	37.8
<b>V10</b>	7.4	0.2	22.7	28.0	0.7	22.9	51.9	10.9	44.1	38.7	2.0	37.8
<b>FCU1</b>	10.6	0.2	23.1	28.8	0.8	26.3	51.1	13.4	48.6	43.9	4.2	37.6
<b>FCU2</b>	6.0	0.2	23.4	26.7	0.7	21.2	52.8	10.1	42.9	36.7	1.4	36.2
<b>FCU3</b>	7.3	0.2	22.2	27.8	0.7	22.7	51.7	10.8	43.8	38.5	2.0	37.9
<b>FCU4</b>	7.2	0.2	22.2	27.9	0.7	22.9	51.6	10.8	43.8	38.7	2.0	37.9
<b>FCU5</b>	9.4	0.2	33.8	39.2	1.6	24.4	56.4	13.3	45.1	40.0	3.9	43.4
<b>FCU6</b>	3.2	0.2	17.6	25.8	0.6	24.5	48.5	10.4	41.6	40.9	1.4	36.3
<b>FCU7</b>	7.0	0.2	21.3	27.9	0.7	23.2	51.0	10.8	43.5	39.0	2.0	38.3
<b>FCU8</b>	7.2	0.2	22.1	27.9	0.7	22.9	51.5	10.8	43.8	38.7	2.0	37.9
<b>FCV1</b>	7.3	0.2	23.2	27.9	0.8	25.2	53.2	11.7	43.6	39.8	2.2	37.9
<b>FCV2</b>	7.6	0.2	22.1	28.0	0.7	22.9	51.5	10.9	44.0	38.7	2.1	38.2
<b>FCV3</b>	7.2	0.2	22.1	27.9	0.7	23.0	51.5	10.9	43.8	38.8	2.0	37.9
<b>FCV4</b>	7.3	0.2	22.3	28.0	0.7	23.1	51.6	10.9	43.9	38.9	2.1	38.0
<b>FCV5</b>	7.5	0.2	23.1	28.5	0.7	23.4	51.9	11.3	44.4	39.4	2.2	37.9



Table C-15: Tensions in bridles of Cage 2 for different failure modes (flow direction = 70°).

Failure mode	Bridle of Cage 2 [kN]											
	B1	B2	B3	B4	B5	B6	B7	B8	B9	B10	B11	B12
<b>U1</b>	0.2	0.1	1.3	27.9	0.4	7.9	34.8	0.9	32.1	24.8	0.7	46.2
<b>U2</b>	7.7	0.1	10.1	16.2	0.4	7.6	43.4	3.2	43.8	26.4	0.8	32.4
<b>U3</b>	1.9	0.1	6.1	22.3	0.4	9.3	38.0	2.3	38.4	28.8	0.7	37.4
<b>U4</b>	2.7	0.1	8.6	23.0	0.4	8.6	39.2	2.5	39.7	28.7	0.7	37.1
<b>V1</b>	8.8	0.1	5.6	15.0	0.4	3.8	36.2	2.8	48.6	30.1	0.9	31.4
<b>V2</b>	0.1	0.1	0.1	71.0	0.2	0.2	0.1	0.1	12.2	21.7	2.2	88.4
<b>V3</b>	0.1	0.1	38.3	0.3	0.2	0.2	75.1	2.9	36.6	0.2	0.1	0.1
<b>V4</b>	4.0	0.1	9.3	19.7	0.4	8.1	39.9	3.1	43.6	29.9	0.8	32.7
<b>V5</b>	2.7	0.1	8.8	23.2	0.4	8.7	39.2	2.6	39.9	29.0	0.7	37.2
<b>V6</b>	1.1	0.1	11.2	26.8	0.5	12.0	41.7	3.4	36.9	29.4	0.7	39.8
<b>V7</b>	7.3	0.1	0.5	5.2	0.3	0.2	35.5	0.8	46.2	23.3	0.6	24.1
<b>V8</b>	0.1	0.1	0.2	22.0	0.4	11.7	33.8	2.6	38.2	32.8	0.7	38.7
<b>V9</b>	2.3	0.1	7.8	23.5	0.4	9.1	38.6	2.4	38.9	28.9	0.7	37.9
<b>V10</b>	3.3	0.1	9.8	23.3	0.4	8.0	40.0	2.6	40.4	28.4	0.7	37.1
<b>FCU1</b>	1.4	0.1	7.6	24.5	0.4	7.6	37.7	1.8	38.4	28.0	0.7	38.3
<b>FCU2</b>	6.3	0.1	9.6	24.4	0.4	12.3	38.7	5.0	44.8	35.2	1.1	38.1
<b>FCU3</b>	2.5	0.1	9.0	23.0	0.4	8.3	39.5	2.4	39.7	28.4	0.7	36.8
<b>FCU4</b>	2.7	0.1	8.8	23.2	0.4	8.6	39.2	2.6	39.9	28.9	0.7	37.1
<b>FCU5</b>	4.8	0.1	6.7	18.9	0.4	4.6	37.7	1.6	42.7	26.8	0.7	34.1
<b>FCU6</b>	4.9	0.2	19.5	33.3	0.5	10.4	44.3	4.5	41.2	30.7	1.0	43.0
<b>FCU7</b>	1.4	0.1	6.9	22.4	0.4	9.5	38.0	2.5	39.2	29.8	0.7	36.4
<b>FCU8</b>	2.6	0.1	8.6	23.2	0.4	8.7	39.1	2.6	39.9	29.0	0.7	37.2
<b>FCV1</b>	2.7	0.1	8.6	23.2	0.4	8.4	39.0	2.5	40.0	28.9	0.7	37.1
<b>FCV2</b>	2.7	0.1	8.9	23.1	0.4	9.1	39.5	2.7	39.8	29.2	0.7	37.1
<b>FCV3</b>	4.7	0.1	8.2	23.8	0.4	8.7	38.9	2.7	40.8	28.9	0.8	38.8
<b>FCV4</b>	2.6	0.1	8.7	23.3	0.4	8.8	39.1	2.6	40.0	29.2	0.7	37.1
<b>FCV5</b>	3.1	0.1	9.5	23.8	0.4	8.6	39.4	2.8	40.6	29.4	0.7	37.3

Table C-16: Tensions in bridles of Cage 3 for different failure modes (flow direction = 70°).

Failure mode	Bridle of Cage 3 [kN]											
	B1	B2	B3	B4	B5	B6	B7	B8	B9	B10	B11	B12
U1	2.4	0.1	4.5	15.8	0.4	4.9	41.1	0.7	34.5	19.3	0.6	35.0
U2	3.3	0.1	6.3	16.4	0.4	4.5	42.2	0.8	35.8	19.2	0.6	34.9
U3	2.7	0.1	3.5	16.2	0.4	7.0	39.7	1.2	36.9	23.2	0.6	34.7
U4	3.2	0.1	7.9	19.8	0.4	7.5	41.7	1.8	37.7	24.4	0.7	36.6
V1	9.0	0.1	9.4	13.5	0.4	6.4	43.6	2.9	44.9	25.6	0.8	31.2
V2	5.9	0.1	1.9	15.6	0.4	1.5	34.2	0.9	42.8	25.1	0.7	34.0
V3	0.1	0.1	0.1	70.5	0.2	0.1	0.1	0.1	5.4	17.4	1.6	90.9
V4	0.1	0.1	38.8	0.3	0.2	0.2	75.0	2.8	36.0	0.2	0.1	0.1
V5	3.6	0.1	8.1	19.9	0.4	8.0	41.7	2.1	38.4	25.4	0.7	36.5
V6	1.4	0.1	7.2	21.7	0.4	7.6	40.8	1.4	35.5	24.1	0.6	38.1
V7	3.2	0.1	9.7	20.1	0.4	8.7	44.2	2.1	36.9	23.7	0.6	36.6
V8	7.1	0.1	0.4	4.2	0.3	0.2	37.3	0.7	44.0	20.6	0.6	24.7
V9	0.1	0.1	0.2	18.1	0.4	11.2	36.2	1.9	36.0	29.1	0.6	36.1
V10	3.3	0.1	9.6	20.2	0.4	6.5	42.9	1.6	37.7	23.2	0.6	36.3
FCU1	3.0	0.1	7.8	20.3	0.4	8.0	41.7	1.9	37.3	24.8	0.7	37.0
FCU2	1.8	0.1	6.9	21.3	0.4	6.8	40.4	1.2	36.0	23.6	0.6	37.8
FCU3	4.5	0.1	8.2	20.2	0.4	9.1	41.5	2.7	39.6	27.1	0.7	36.7
FCU4	3.5	0.1	8.2	19.9	0.4	7.8	41.8	2.0	38.3	25.1	0.7	36.4
FCU5	4.8	0.1	8.4	18.3	0.4	7.4	42.7	2.0	39.2	24.3	0.7	35.5
FCU6	6.6	0.1	6.8	15.7	0.4	4.7	40.9	1.5	41.9	23.8	0.7	33.6
FCU7	4.7	0.1	13.0	24.0	0.5	8.4	44.4	2.7	39.0	25.5	0.8	38.8
FCU8	3.4	0.1	7.8	19.8	0.4	8.2	41.5	2.1	38.3	25.6	0.7	36.4
FCV1	3.6	0.1	8.1	20.0	0.4	8.1	41.7	2.1	38.5	25.5	0.7	36.5
FCV2	3.6	0.1	8.1	19.9	0.4	8.0	41.7	2.1	38.5	25.4	0.7	36.5
FCV3	3.5	0.1	8.5	19.2	0.4	10.0	43.1	2.5	38.0	26.2	0.7	36.1
FCV4	7.4	0.1	6.9	20.9	0.4	7.9	41.1	2.2	40.0	25.1	0.8	39.5
FCV5	4.0	0.1	8.8	20.3	0.4	8.6	41.9	2.5	39.4	26.7	0.7	36.3

Table C-17: Tensions in bridles of Cage 4 for different failure modes (flow direction = 70°).

Failure mode	Bridle of Cage 4[kN]											
	B1	B2	B3	B4	B5	B6	B7	B8	B9	B10	B11	B12
<b>U1</b>	0.1	0.1	0.2	7.9	0.3	0.4	42.9	0.3	21.8	4.2	0.4	34.1
<b>U2</b>	0.2	0.1	0.2	10.7	0.3	0.5	41.6	0.3	22.3	5.6	0.4	36.0
<b>U3</b>	0.1	0.1	7.2	1.0	0.3	0.3	51.9	0.3	20.3	0.2	0.2	25.5
<b>U4</b>	0.1	0.1	0.1	16.4	0.4	3.8	37.3	0.4	28.2	16.0	0.5	37.8
<b>V1</b>	6.3	0.1	1.6	15.8	0.4	2.3	39.0	0.5	32.9	14.8	0.6	39.0
<b>V2</b>	7.1	0.1	0.5	11.4	0.4	2.6	39.1	0.5	34.9	15.8	0.6	35.5
<b>V3</b>	4.9	0.1	0.2	13.3	0.3	1.0	34.0	0.6	37.9	21.5	0.6	34.4
<b>V4</b>	0.1	0.1	0.1	71.8	0.2	0.1	0.1	0.1	0.7	14.7	1.8	94.4
<b>V5</b>	4.1	0.1	1.0	17.3	0.4	2.5	38.3	0.4	30.0	14.3	0.5	40.3
<b>V6</b>	3.1	0.1	0.7	17.4	0.4	2.5	38.2	0.4	28.7	13.8	0.5	40.3
<b>V7</b>	2.6	0.1	0.6	16.9	0.4	1.8	38.2	0.4	27.8	12.5	0.5	39.8
<b>V8</b>	2.1	0.1	2.0	18.1	0.4	2.8	40.1	0.4	26.4	11.7	0.5	40.9
<b>V9</b>	5.5	0.1	0.2	2.4	0.3	0.2	40.8	0.4	34.2	11.8	0.5	27.1
<b>V10</b>	0.1	0.1	0.3	21.0	0.4	5.3	36.5	0.4	26.6	17.6	0.5	42.8
<b>FCU1</b>	3.4	0.1	0.7	16.7	0.4	2.2	38.2	0.4	29.2	13.6	0.5	39.8
<b>FCU2</b>	2.9	0.1	0.7	17.2	0.4	2.4	38.2	0.4	28.4	13.4	0.5	40.2
<b>FCU3</b>	3.4	0.1	0.9	17.8	0.4	2.2	38.0	0.4	29.0	13.7	0.5	40.6
<b>FCU4</b>	4.4	0.1	1.1	17.4	0.4	2.8	38.3	0.4	30.5	14.8	0.5	40.4
<b>FCU5</b>	2.8	0.1	0.5	15.5	0.4	1.5	38.4	0.4	28.4	12.3	0.5	38.7
<b>FCU6</b>	3.1	0.1	0.5	14.3	0.4	1.4	38.7	0.4	28.8	12.1	0.5	37.6
<b>FCU7</b>	4.4	0.1	0.5	14.6	0.4	1.3	38.0	0.4	31.0	13.7	0.5	37.8
<b>FCU8</b>	4.2	0.1	1.6	18.0	0.4	2.6	38.6	0.4	30.1	14.3	0.5	40.7
<b>FCV1</b>	4.1	0.1	1.1	17.5	0.4	2.6	38.3	0.4	30.1	14.4	0.5	40.4
<b>FCV2</b>	4.1	0.1	1.1	17.4	0.4	2.5	38.3	0.4	30.0	14.3	0.5	40.4
<b>FCV3</b>	4.2	0.1	1.1	17.4	0.4	2.6	38.2	0.4	30.2	14.5	0.5	40.3
<b>FCV4</b>	4.0	0.1	1.5	15.8	0.4	5.9	41.0	0.5	29.6	15.6	0.5	39.7
<b>FCV5</b>	15.7	0.1	0.4	22.6	0.4	1.6	38.1	0.5	33.6	12.3	0.8	51.8